Passive and Thermo-Optic Characterization of Long-Range Surface Plasmon-Polariton Structures in CYTOP

By:

Hui Fan

A thesis submitted to the School of Graduate Study and Research
in partial fulfillment of the requirements for the degree of

Master of Applied Science

Ottawa-Carleton Institute for Electrical and Computer Engineering
Department of Electrical Engineering
University of Ottawa
Feb 28, 2011

Abstract

Long-range surface plasmon-polariton waveguides fabricated of gold, cladded with CYTOP, designed to be 5µm wide and 35nm thick, were modelled and fabricated by other researchers and tested by the author. In passive measurements, cutback curves were drawn and S-bends, Y-junctions, Mach-Zehnder interferometers, and couplers were tested. Results show that the fabricated waveguide thicknesses are inconsistent and thinner than designed, and improvement of their fabrication quality is necessary. In thermo-optic measurements, electric currents were injected heating the waveguides and changing the refractive index of the claddings. Electromigration were characterized and the conclusion was that the waveguides can work under the current density 70GA/m^2. Mode extinction experiments were made and as one waveguide was repeatedly tested its mode extinction threshold gradually decreased due to heat accumulation and CYTOP glass-transition. 2.5mA was safe to prevent mode extinction in the first 12 experiments. The optical response time was also measured and discussed.

Acknowledgements

I would like to acknowledge the support and guidance of my supervisor Prof. Pierre Berini throughout the course of my graduate studies.

I would like to acknowledge the help and assistance of Ali Akbari, Anthony Olivieri, Asad Khan, Charles Chiu, Ewa Lisicka-Skrzek, Israel de Léon Arizpe, Michal Tencer, Oleksiy Krupin, Raza Hanif, and Robin Buckley.

I would also like to acknowledge the encouragement of my family.

Table of Contents

1. Introduction

1.1 Motivation

The motivation for this work is to introduce a new kind of long-range surface plasmon-polariton (LRSPP) waveguide for the interest of LRSPP biosensing. Thus it is necessary to verify the mode behaviour of varieties of passive structures, as well as to study the thermo-optic properties of straight waveguides.

1.2 Organization

The current chapter will introduce the concepts of surface plasmon-polaritons (SPPs), LRSPPs in metal slabs and stripes, and subsequently, thermo-optic effects related in this work.

Chapter 2 gives parameters of the tested sample chips in cross-sectional view and top view, as well as components of the experiment setup. It also describes the procedures and points for attention of the experiments.

The experimental results for passive structures and thermo-optic modulation are presented and analyzed in Chapter 3 and 4, respectively, the conclusions of which are drawn or summarized in brief in Chapter 5. Chapter 5 also introduces the contributions of this work, and gives suggestions for future work.

1.3 Surface plasmon-polaritons (SPPs)

SPPs are transverse magnetic (TM) polarised optical surface waves that propagate typically along a metal-dielectric interface, therefore termed the “single-interface” SPPs [1~3]. This structure supports a non-radiative SPP mode, whose field peaks at the interface and decays exponentially in both media, as shown in Figure 1.1.

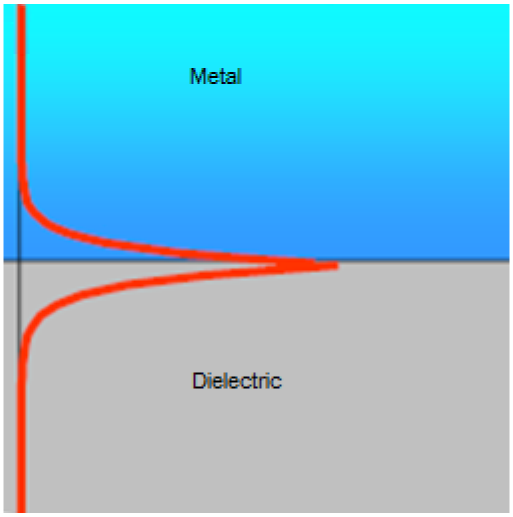

Figure 1.1: SPPs travelling along a metal-dielectric interface [4]

The single-interface SPPs have useful properties such as good confinement and very high surface and bulk sensitivities, but they also have an obvious disadvantage that limits its scope for applications -- the attenuation is too high for the wave to travel a long distance away.

Researchers found a method of reducing the SPP attenuation. That is to use a thin metal film or stripe bounded on the sides by the same dielectric material, operating the structure in a mode called "long-range" SPP mode. With a comparatively lower attenuation, the wave is allowed to propagate over a much longer distance. However, this comes at the expense of reduced confinement, though the extended range may outweigh the reduction of confinement and be made use of better applications [5].

1.4 Long-range surface plasmon-polaritons (LRSPPs)

1.4.1 Metal slab LRSPP

When the widths of the layers are optically infinite, the waveguide is called "metal slab".

Figure 1.2(a) shows the single-interface SPP. The red curves represent the distribution of the main transverse electric field component (E_y) of the SPP. The propagation direction is along the z axis which is out of the page.

Figure 1.2(b) shows the metal slab. The red curves represent the distribution of the main transverse electric field component (E_y) of the modes supported. The metal slab consists of a thin metal film of thickness t and relative permittivity $\varepsilon_{r,2}$ with both sides bounded by optically semi-infinite dielectric claddings of relative permittivity $\varepsilon_{r,1}$ and $\varepsilon_{r,3}$.

In most applications involving the LRSPP, the metal slab structure is supposed to be symmetric, with the relative permittivity $\varepsilon_{r,1}= \varepsilon_{r,3}$. As the thickness t is reduced, the bound single-interface SPPs supported by the individual top and bottom metal-dielectric interfaces will couple, forming two TM-polarised (E_x=H_y=H_z=0) bound super modes [1], also called coupled modes. For the reason that the main transverse electric field component of them is either asymmetric or symmetric, these two super modes are referred to as a_b or s_b for asymmetric bound and symmetric bound, respectively. The subscript *b* signifies “purely bound”, meaning non-radiative, in contrast with two other modes labelled a_L and s_L standing for “leaky” formed in the asymmetric structure case.

In symmetric structures, suppose the claddings are lossless, the attenuation of the s_b mode diminishes as the thickness t is reduced [7]. This occurs because its mode field is increasingly expelled from the metal film and penetrates more deeply into the claddings as t approaches zero [5]. The term “LRSPP” refers to the s_b mode of a thin symmetric metal slab for which the t is regarded as infinitesimal. In opposition, the a_b mode shows more confinement in the metal as t reduces and its attenuation rises up, making the mode short-ranged.

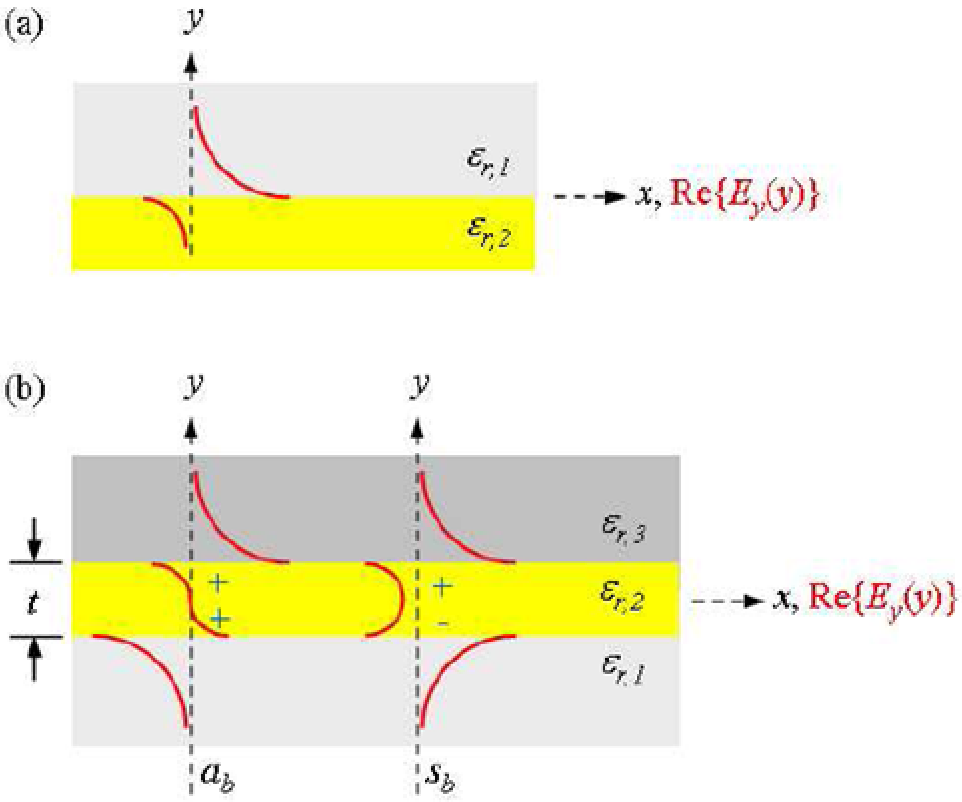

Figure 1.2: Single-interface SPP, metal slab LRSPP, and their curves of mode [6]

1.4.2 Metal stripe LRSPP

In the metal slab LRSPP case, the width of the metal layer is large enough to be regarded infinite, but what is used in the experiments are actually metal stripes whose width is limited to a finite value, as exhibited in Figure 1.3. As the layer turns into a stripe, the modes supported will change as well. The metal stripe ($\varepsilon_{r,2}$) of thickness t and width w is bounded by semi-infinite dielectric claddings ($\varepsilon_{r,1}$, $\varepsilon_{r,3}$). The direction of mode propagation is along the z axis, which is directed out of the page.

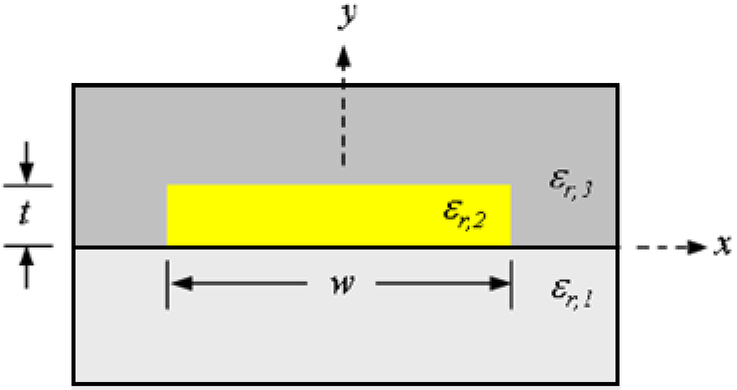

Figure 1.3: Metal stripe LRSPP [8]

In metal stripes the solutions to Maxwell's equations cannot be obtained analytically and straightforwardly as in metal slabs. The evolution of modes with dimensions t and w, materials properties $\varepsilon_{r,1}$, $\varepsilon_{r,2}$ and $\varepsilon_{r,3}$, and wavelength of operation λ_0 is complicated, especially for asymmetric structures ($\varepsilon_{r,1} \neq \varepsilon_{r,3}$), thus they have to be derived numerically [5]. This difficulty is due to the fact that all modes are created from the coupling of elemental corner or edge modes, which changes with structure parameters and wavelength of operation, making the coupled modes unpredictable. Despite the increasing analysis effort, the metal stripe can be handled by well-established numerical techniques, such as the method of lines (MoL) and the finite element method (FEM). Besides, the difficulty can, to some extent, be reduced since most of the applications mainly employ symmetric structures ($\varepsilon_{r,1} = \varepsilon_{r,3}$), which is the case of interested here and focused on in the following paragraphs.

When the structure is symmetric there are four fundamental modes supported by the metal stripe, namely aa_b^0, as_b^0, sa_b^0, and ss_b^0. In these labels the a and s refer to asymmetric and symmetric respectively; the first position is associated with the horizontal dimension x while the second with the vertical dimension y. The b here, again, implies non-radiative, or "purely bound".

Higher order modes having extrema along x in their field distribution can also be supported. The E_y field component dominates for all modes [5] when t is small enough compared to w, hence the modes are essentially TM in character.

As t approaches zero, all modes can eventually be categorized into two kinds: lower attenuation modes (ss_b^m and as_b^m) acting like the s_b mode in metal slab case, and higher attenuation modes (sa_b^m and aa_b^m) like the a_b mode, depending on the symmetry of distribution of E_y along y [9]. Here m refers to the m~th order mode. One fundamental mode ss_b^0 evolves a field distribution well-matched to Gaussian-like fields such as the output beam of a single mode fiber [9], accompanied by a decrease of confinement and attenuation. The ss_b^0 mode in a thin symmetric metal stripe is the fundamental long-range mode, and is used as the so-called "LRSPP mode" for all the experiments related to this work.

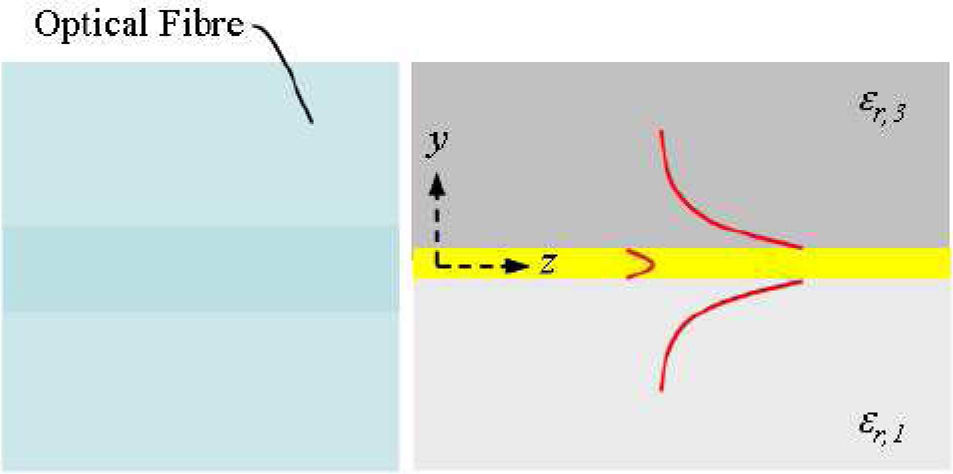

Figure 1.4: An optical fiber butt-coupled to the metal stripe to excite the LRSPP [10]

Since the ss_b^0 mode for the thin symmetric structures has a Gaussian-like field distribution, efficient excitation of this LRSPP mode can be achieved by the polarization-aligned and size-matched fundamental mode of a single mode fiber (SMF), butt-coupled directly into the structure.

Longitudinal cross-sectional view is in Figure 1.4 with the excited LRSPP sketched in red. This is the method adopted for all the coupling in experiments carried out for this work.

Another fundamental mode as_b^0 evolves in a similar manner into the first higher-order long-range mode as t approaches zero. Higher-order long-range mode may also exist originating from ss_b^m (m>0, odd) and as_b^m (m>0, even), with a cut-off dimension that increases with m [9]. These higher order modes have attenuation low enough to be considered as long-range only near cut-off. Modes with sa_b^m and aa_b^m symmetries have increasing attenuation as t approaches zero and hence are not long-range.

When the structure is asymmetric, the ss_b^0 mode exhibits a cutoff thickness that was not presented in the symmetric structures [9]. Henceforth, the ss_b^0 does not exist in a very thin asymmetric metal stripe for it is eventually cutoff as t approaches zero. This makes the ss_b^0 sensitive to asymmetry of refractive index in top and bottom claddings.

1.5 Thermo-optic modulation

1.5.1 Thermo-optic effect

The thermo-optic effect is a phenomenon by which heat can influence the refractive index of a material [11]. For constant pressure and wavelength, there is a linear model for the relationship between temperature and refractive index, given in the equation below.

$$n(T) = n(T_0) + (T - T_0)\frac{dn}{dT} \qquad (1.1)$$

n is the refractive index while T is the temperature. The variation of refractive index as a function of temperature $\frac{dn}{dT}$ is called the thermo-optic coefficient (TOC), which can be regarded as a constant if the temperature range is relatively small. However, in practice, the TOC usually varies for a temperature range of 100˚C [12] and therefore should be decomposed as a sum of smaller ranges of constant TOC. In this case, (1.1) changes into the following equation.

$$n(T_N) = n(T_1) + \sum_{i=1}^{N-1}[(T_{i+1} - T_i)(\frac{dn}{dT})_{T_i}] \tag{1.2}$$

i and N are the i~th sub-range and the total number of sub-ranges respectively. Thus, given the temperature range of the thermo-optical device, the refractive index can be determined applying the equations (1.1) and (1.2). The linear relationship between refractive index and temperature in thermo-optic effect is generated by differentiating the Clausius-Mossotti relation [12].

1.5.2 Mechanism of modulation

Thermo-optic modulation has an important role in optical sensing for the simple design and cheap construction cost of its devices. The methods for modulation are many. The experiments for this work applied one approach. A straight waveguide serves as both path for light and source of heat, in which electric current is injected and generates heat. The heat causing the temperature of the metal strip to increase, forming a temperature gradient in the nearby CYTOP cladding region as the heat dissipates outwards, and changing the refractive index correspondingly according to the thermo-optic effect. The CYTOP is known to have a negative TOC. Thus claddings closer to the center region where the temperature is high will have lower refractive index, and vice versa, forming an anti-guide which will exert a negative effect on the propagation of the LRSPP mode through the waveguide, causing the confinement of the waveguide to be reduced. As the current density of the injected current goes up, this negative effect will grow stronger, and in the end cut the LRSPP mode off, making most of the optical power radiate and couple to cladding modes. Reference [13] serves an example to this method.

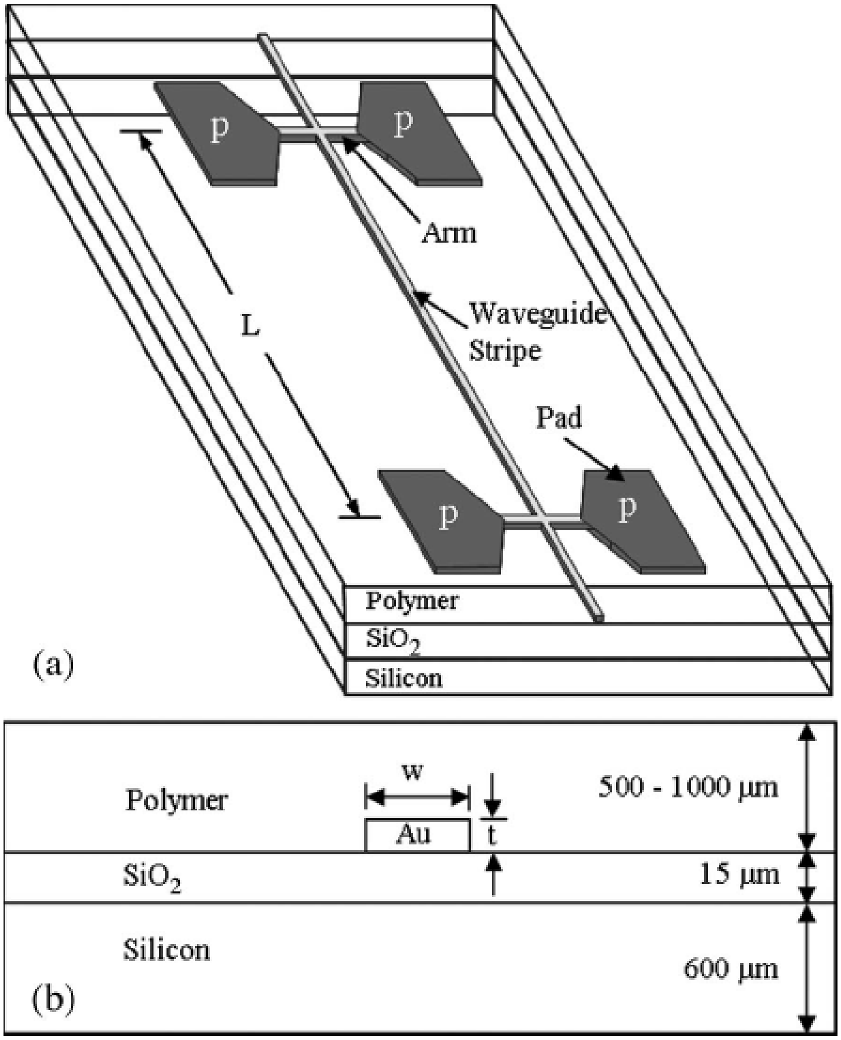

Figure 1.5: Refractive index mismatch created by selecting two index matched materials with different TOCs to be the top and bottom claddings and then heating them to break the index match [11]

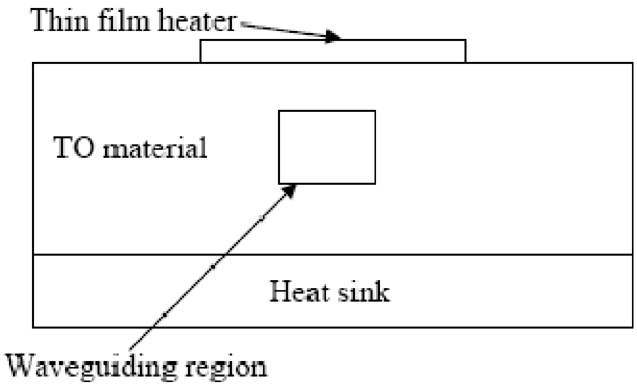

Figure 1.6: Refractive index mismatch created by generating a temperature gradient using the heater on the top and heat sink at the bottom [15]

There are other methods for modulation, which is not used in this work but adopted by some other researchers. Another mechanism is to create an asymmetry of refractive index for the top and bottom cladding, motivated by the fact that LRSPP mode is sensitive to asymmetry as introduced in Section 1.4. This can be realized by selecting two index matched materials with different TOCs to be the top and bottom claddings and then heating them to create an index mismatch, making the structure asymmetric, as illustrated in Figure 1.5. Reference [11] and [14] choose this method. This asymmetry can also be created by generating a temperature gradient in the waveguide region from top to bottom, as is done in reference [15] and shown in Figure 1.6; the gradient in this case is caused by the heater on the top and the heat sink at the bottom.

A third mechanism is to use a Mach-Zehnder interferometer (MZI) as the modulator and inject electric current to heat one of its arms. The change in refractive index with temperature in the heated arm will lead to a difference in optical path length between the two arms. As the current varies the difference of optical path length will change between constructive and destructive interference conditions and the optical power output will oscillate between normal MZI output and zero. This method is applied in reference [16], represented in Figure 1.7.

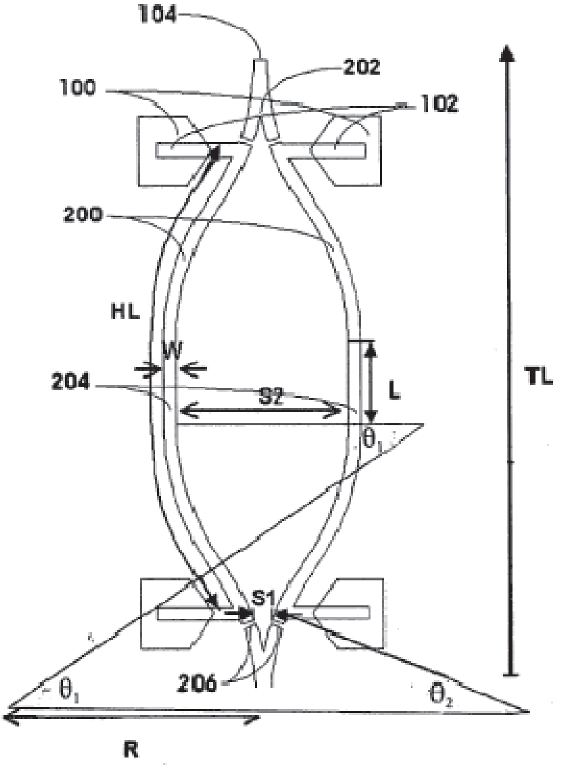

Figure 1.7: Thermo-optic modulation using MZIs [16]

1.5.3 Electromigration

The metal waveguides suffer a degradation known as electromigration when the heavy positive ions constituting the metal are displaced due to the strong electron-wind colliding on them when a high current density is applied [7]. In a polycrystalline metal such as our gold waveguide, the electromigration mechanism occurs predominantly through the migration of ions along the grain boundaries [17].

Electromigration should be monitored as we increase the electric current during the thermo-optic modulation, for when the current reaches a very high level electromigration may take place burning the waveguide in a short period of time, reflected by dramatic changes in the resistance of the waveguide. Before starting the thermo-optic modulation, it is necessary to determine a threshold voltage or current under which the waveguide can work for a long time without burning out. This value is known as the electromigration threshold.

However, we should know that given enough time, even small voltage or current can burn the waveguide, and the reducing of lifetime is accumulative because the electromigration process is irreversible. This is introduced in details in Appendix A.

2. Experimental techniques

2.1 Devices

2.1.1 Cross-sectional view of chips

Figure 2.1 illustrates the front cross-sectional view of the chips used in the experiments. The whole device was supported by a 450 μm thick silicon substrate and fabricated as follows [18, 19]. Firstly, a 10 μm bottom cladding layer made of CYTOP was coated upon the silicon substrate. A gold layer of 35 nm was then deposited on the bottom claddings and patterned in a lift-off lithography process by removing the gold in some predetermined areas according to the mask. After properly depositing and patterning the waveguides, another 10 μm CYTOP layer was coated as the top claddings, fully embedding the LRSPP devices into CYTOP.

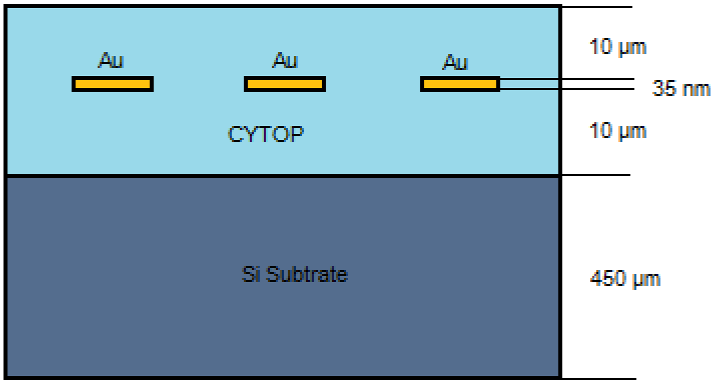

Figure 2.1: Cross-sectional view of chips

2.1.2 Passive structures

Figure 2.2 shows all kinds of passive structures measured in the experiments, including straight waveguides of different widths, S-bends, Y-junctions, Mach-Zehnder interferometers (MZI), and couplers. These waveguides had a thickness of 35 nm, and were fabricated on the chips DIE39, DIE38-1, DIE38-2, DIE6, DIE3, DIE21-6, DIE21-3, and DIE32.

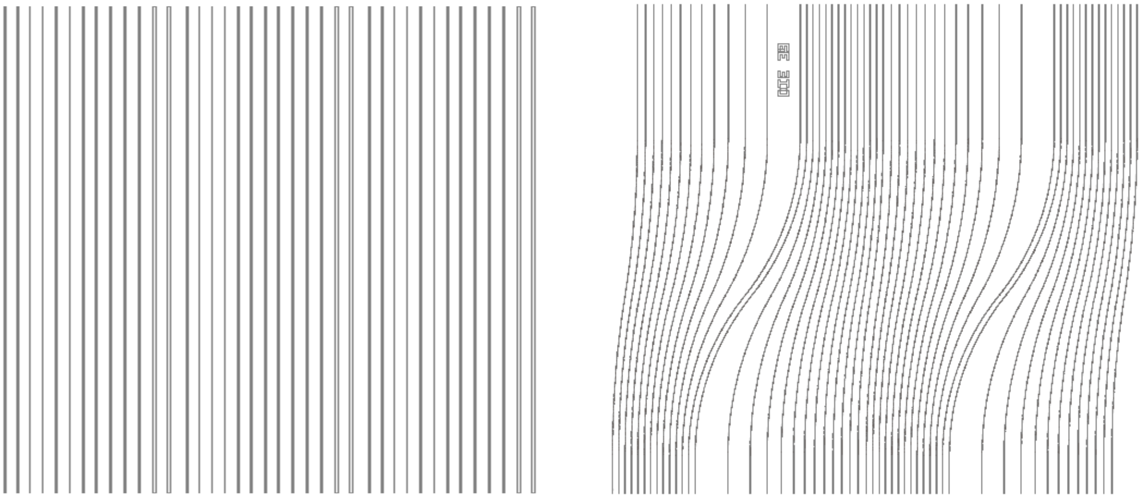

(a) Straight waveguide of different widths (b) S-bends

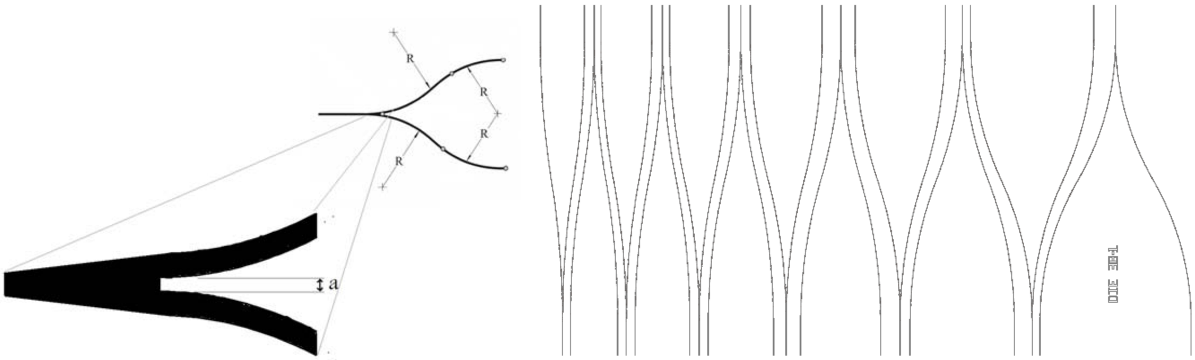

(c) The "Y-junction" structure (d) Y-junctions

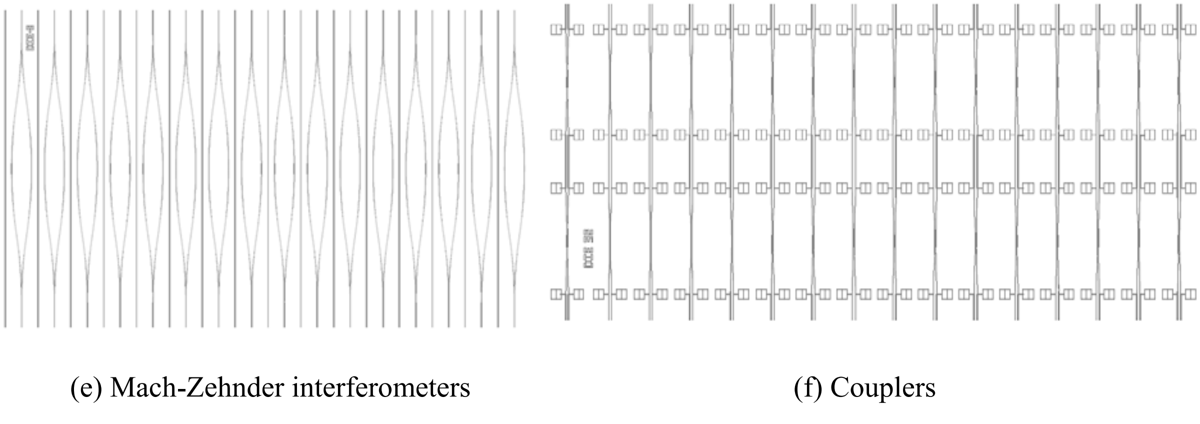

(e) Mach-Zehnder interferometers (f) Couplers

Figure 2.2: All kinds of passive structures [20]

The straight waveguides of different widths are shown in Figure 2.2(a). These waveguides were made on DIE39 taking half of the chip, and were arranged in 3 repeats. Each repeat started at a 1-µm-wide waveguide and ended at a 12-µm-wide one as an arithmetic series with a step of 1 µm, and then with an extra 5-µm-wide waveguide attached to the very beginning of the series. This extra 5-µm-wide waveguide was added because 5 µm is the optimized width for the design of the chips tested in the experiments (S-bends, Y-junctions, etc). All of these straight waveguides were 3.8 mm long.

The S-bends took the other half of DIE39 and is represented in Figure 2.2(b). Each S-bend began with a straight section, then followed with two curved sessions bending in opposite directions, and then with another straight section. The S-bends were also arranged in repeats. There were 4 repeats of S-bends on DIE39. In the first repeat they had radii of curvature of 2 mm to 8 mm with a 0.5 mm step. The second repeat was the same arithmetic series but with a decreasing trend instead of an increasing one. The third repeat was an increasing series again, and the last one decreasing again. All these waveguides had the same width of 5 µm, same length of 3.8 mm in the direction of the width of the chip, and same total length of 1.3 mm for the two straight sections, whereas different path lengths because the radii of curvature of their S-bends differed from each other. Table 2.1 gives the path lengths for S-bends of different radii of curvature.

Radius(mm)	8	7.5	7	6.5	6	5.5	5
Path length (mm)	3.81	3.81	3.81	3.82	3.82	3.82	3.83

Radius(mm)	4.5	4	3.5	3	2.5	2
Path length (mm)	3.83	3.84	3.86	3.88	3.92	4.00

Table 2.1: The path lengths for S-bends of different radii of curvature

The Y-junctions were fabricated on DIE38-1 and DIE38-2, both were 3 mm wide. In reference to Figure 2.2(c) we can observe that a Y-shaped waveguide consisted of 2 S-bends bending to opposite sides and the “Y-junction” structure was formed in the intersection of them. Waveguides on the same chip would have the same Y-junction width a=1 µm or a=2 µm respectively on DIE38-1 or DIE38-2. As Figure 2.2(d) shows, on both chips the Y-junctions were arranged based on the radii of curvature, similarly to the S-bends case. Their radii of curvature ranged from 2 mm to 7.5 mm with a step of 0.5 mm. The Y-junctions next to each other opened in opposite directions. All the Y- shaped waveguides had the same width of 5 µm.

Figure 2.2(e) illustrates DIE3, one of the chips on which the MZIs were fabricated. We can regard a MZI as two Y-junctions joined together with their openings facing each other. MZIs were fabricated on DIE6, DIE21-6, and DIE21-3 as well, amongst which DIE6 and DIE21-6 were 3 mm long and had a center waveguide separation of 140 µm for the MZIs, while for DIE3 and DIE 21-3 these parameters were 3.8 mm and 240 µm. MZIs with 1 µm and 2 µm Y-junctions were made alternately on these chips, and there was also one straight waveguide between each pair of neighbouring MZIs. All waveguides on these four chips were 5 µm in width, and all curved sections had the same radii of curvature of 5.5 mm, the optimized radii of curvature for the design. One thing the readers should bear in mind is that for some selected MZIs and straight waveguides, micro-fluidic channels were created in the top CYTOP claddings so that the gold waveguides could be immersed and functionalized in buffer liquid solutions (not tested herein). This, however, induced a problem to the experiments -- there were no fully cladded MZIs with 1 µm Y-junctions available because of the design of these chips. Hence, all the MZIs tested in the experiments were with 2 µm Y-junctions and none with those of 1 µm.

Figure 2.2(f) represents the couplers fabricated on DIE32, a chip 1.5 mm in width. The couplers had the same waveguide width 5 µm, same coupling length 100.25 µm, same radii of curvature 5.5 mm, whereas different coupling separations of 1, 1.5, 2, 2.5, 3, 3.5, 4, 5, 6, 7, 8, 3, 3.5, 4, 5, 6 μm respectively, arranged in sequence. Hereby I need to indicate that DIE32 was originally a 3 mm long chip. Each waveguide structure on this chip was constituted by two identical 1.5 mm long couplers placed in series. Therefore in the experiments, the whole chip was diced into two pieces for the purpose of convenience, each contained one coupler. The dicing might have damaged the end-facet, as indicated in the inspections and the experiment results.

2.1.3 Thermo-optic structures

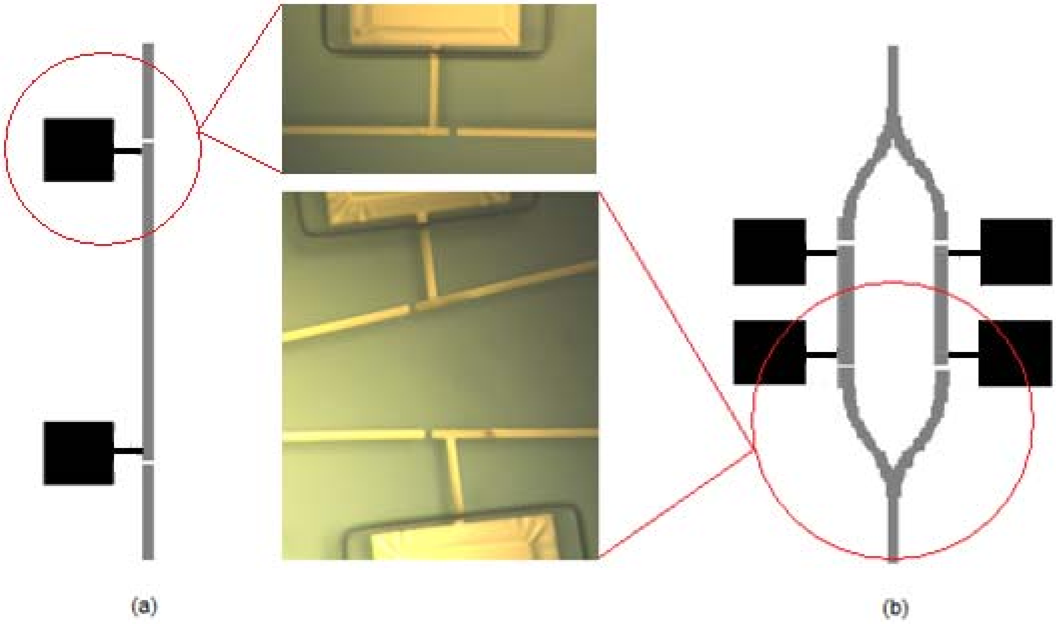

Figure 2.3: Thermo-optic structures [21]

Figure 2.3(a) and (b) represent respectively a straight waveguide tested in thermo-optic experiments for this work, as well as a MZI which was designed to be the basic structure for thermo-optic biosensing and will be tested in future works. These pictures show that waveguides used for thermo-optic measurements had some extra structures than those for the passive measurements. In order that electric current could be injected into the waveguides so that heat could be generated causing thermo-optic effects, metal pads were added for electrical probes connected to a power supply. The pads were kept far from the waveguides to prevent optical coupling, and linked to them by connecting arms of the same thickness and width with the waveguides. Most of the power in the LRSPP mode is contained within a radius of about 3 µm [22] and the pads were placed a least 20 µm away to avoid any possible interference. The junctions formed between the contacting arms and the waveguide were optically non-invasive, either, because the mode at one side of the junction travelled only 5µm to reach the other side so the mode field did not change too much. A 5 µm gap was also designed and fabricated right beside the intersections between the active region of the waveguide and the connecting arm, on the end-facet side. Such µm-sized gaps did not introduce noticeable optical loss, and are sufficiently wide to isolate electric current from the rest of the stripe [21].

2.2 Setup description

2.2.1 Setup for passive measurements

Figure 2.4 illustrates the block diagram for the setup used in passive measurements. Light at the wavelength 1310 nm was generated from a laser and was guided to the system by a Polarization Maintaining Fiber (PMF), which was held by a 5-axis positioner adjustable in x, y, z, yaw, and tilt axis, as is shown in Figure 2.5. The sample chip was mounted on a 3-axis positioner in the middle, adjustable in x, y and roll axis. A binocular microscope with illumination was put above the middle positioner enabling us to observe and adjust the location of the chip. This observation microscope could be replaced by a trinocular one on order that low magnification pictures of the chip could be taken. The beam would enter and pass through the chip, and after exit the chip, be refracted by a Microscope Objective (MO). The image of the out-coming laser spot would reach a CCD camera and be observed on a monitor, which helped us find the LRSPP mode. An optical density filter was placed in front of the camera preventing the mode image shown on the monitor from being saturated. The MO was held by a translation stage fixed on another 5-axis positioner. The translation stage also held a Single Mode Fiber (SMF) and allowed us to shift between the MO and the fiber. After finding the mode we would shift to the SMF, then the output light would be accepted by the SMF and led into a power meter, where the output power was displayed in dBm.

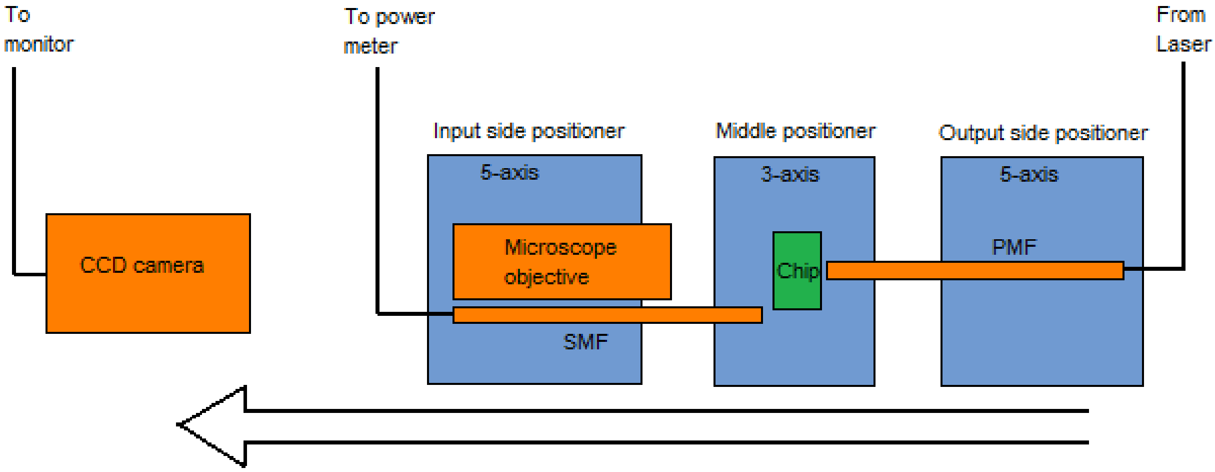

Figure 2.4: Block diagram of the setup for passive measurements (top view)

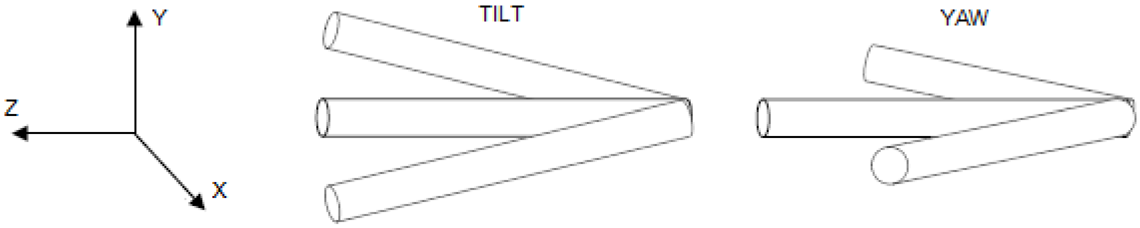

Figure 2.5: Degrees of freedom -- x, y, z, yaw (x-z plane), and tilt (y-z plane) axis [18]

Table 2.2 shows the elements used in the passive measurements with their respective model numbers or part numbers, as well as their manufacturers.

Instrument or Part	Manufacturer	Model No. or Part No.
Tunable Semiconductor Laser	Agilent	81600B
Diode Laser	NTT electronics	NLK 1B5GAAA
Mount	ILX Lightwave	LDM-4980
Current Source	ILX Lightwave	LDX-3220
Temperature Controller for the Laser	ILX Lightwave	LDT-5910
Input side PMF 1310 nm	OZ Optics	PMJ-3A3A-1300-7/125-1-5-1
Input side 5-axis Positioner	Newport	562
Fiber Cleaver	FITEL	S324
Polarizer	OZ Optics	ROT-1-1
Middle 3-axis Positioner	Newport	561D
Observation Microscope	Nikon	1033125
Microscope Objective 25X	Melles Griot	04OAS010
Microscope Objective 10X	Melles Griot	04OAS014
Output side SMF 1310 nm	OZ Optics	SMJ-3A3A-1300/1550-9/125-1-5
Output side 5-axis Positioner	Newport	562
CCD Camera	Electrophysics	7290A
Video Monitor	Panasonic	WV-BM 990
Optical Density Filter	New Focus	5215
Infrared Sensor Card	Newport	F-IRC2
Infrared Sensor Card	ThorLabs	VRC2
Power Meter	EXFO	PM-1600
Power Meter	Agilent	81635A

Table 2.2: Instruments and parts for the passive measurements

2.2.2 Setup for thermo-optic measurements

In the thermo-optic modulation experiments, an electric circuit was added to the pre-existing optical system. The introduction of two extra 3-axis positioners supported by the optical table and adjustable in x, y, and z axis enabled us to hold two electrical probes, adjust their locations precisely, and press them hard onto the metal pads. The probes were connected to a power supply and a multi meter by wires forming a closed electric circuit. The power supply, the multi meter and the power meter were all connected to the computer using GPIB cables allowing us to control them with LabView programming. Such LabView programs would command the power meter to apply a certain voltage between the two probes so as to pass electric current through the pads and the active waveguide region. They would also order the multi meter to measure the current or resistance and ask the power meter to get the value of optical power and, in the end, record these data into a spreadsheet or show them in a live chart.

Table 2.3 gives the additional elements for the thermo-optic measurements with their manufacturers and model numbers or part numbers.

Instrument or Part	Manufacturer	Model No. or Part No.
Refractive Index Matching Oil	Cargille	L-RIAA-766
Extra 3-axis Positioner	Quater Research & Development	XYZ 500 TLM
Extra 3-axis Positioner	Quater Research & Development	XYZ 500 Low Profile
Needle and Test Arm	Quater Research & Development	A-20235
Temperature Controller for the TEC	ILX Lightwave	LDT-5525
Power Supply	Agilent	E3643A
Multi Meter	Keithley	2000
GPIB Card	Agilent	82350B

Table 2.3: Additional instruments and parts for the thermo-optic measurements

2.3 Experimental methods for passive measurements

2.3.1 Sample chip cleaning

Once measuring a new chip, we would always need to follow the procedures described below before we could get convincing data. First of all, the chips should be immersed in Acetone for at least 15 min to remove photo resist introduced during the fabrication process, then be agitated inside a bottle filled with Acetone for about 50 times. Secondly, repeat the first step yet this time use Isopropanol Alcohol (IPA) instead. The third turn of cleaning would be an ultrasonic bath, shaking off dusts that might possibly stick on the end-facet of the chips. Sometimes the ultrasonic bath was omitted by reason that it was often observed to damage the chip, especially the in region close to the end-facets. The next step was to wash the chips with IPA again, and then dry them by putting the chips on a piece of filter paper. Nitrogen blower, if available, could be used to speed up the evaporation of IPA.

2.3.2 Inspection and its limitation

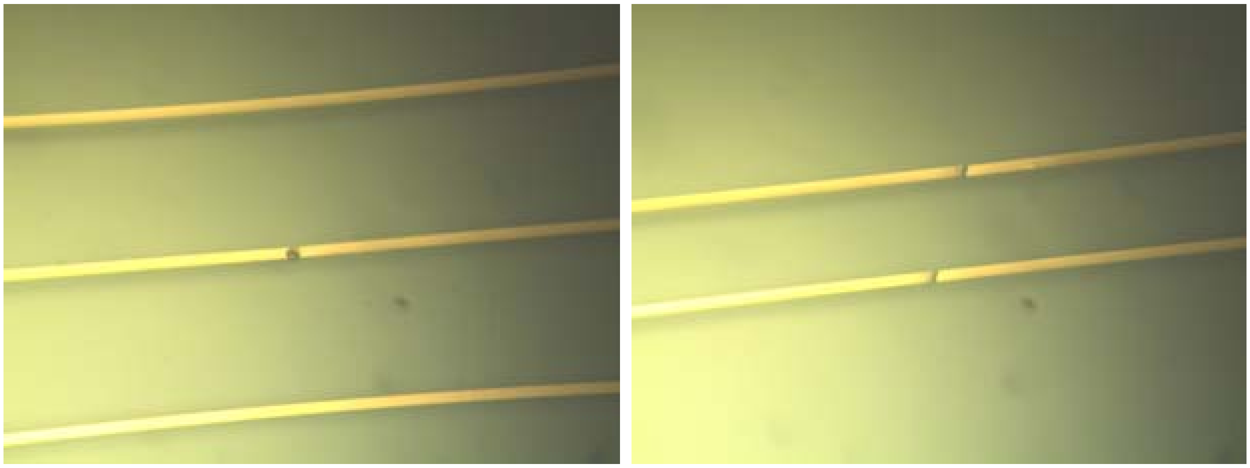

(a) Notches on the waveguide edge

(b) Gaps at an angle to the waveguide

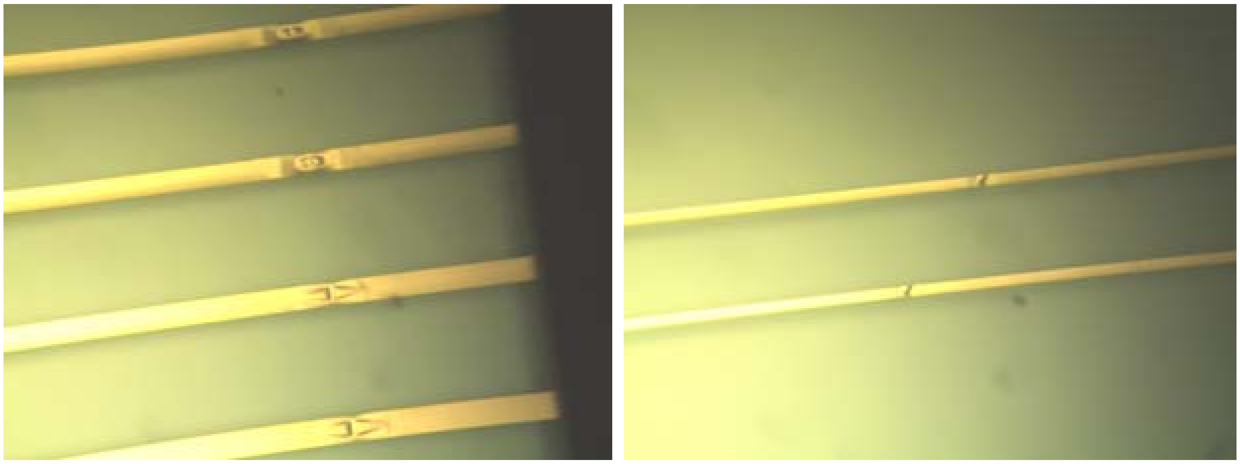

(c) Twisted sections

(d) Scratches on the waveguide top surface

Figure 2.6: Typical kinds of defects on the waveguides

After the cleaning, we need to inspect the quality of the waveguides on the chips under a higher magnification microscope at 50X or 100X so as to get a qualitative prediction of how lossy each waveguide could be as well as a rough estimation on how would the results obtained from each waveguide meet the theoretical expectations. For instance, waveguides with a lot of defects would be lossier and quite unlikely to act as designed to be; a waveguide with too many defects would not be measured at all. Several typical kinds of defects are represented in Figure 2.6, including notches on the waveguide edge, gaps at an angle to the waveguide, twisted sections, and scratches on the waveguide top surface. Hereby, one thing researchers need to notice is: before the inspections, always clean the stage of the higher magnification microscope with Q-tips dipped with IPA. This was to prevent the recontamination of the chip by dusts accumulated on the stage.

The inspections of the chips could be helpful to make the results more convincing and save time and efforts during the experiments. However, since that not all of the defects could be discovered under the microscope, good-looking in the inspection did not necessarily mean that good result could be generated from a waveguide. For instance, damages on the end-facets of the chips would always result in much heavier losses than expected theoretically, but could seldom be observed during the inspection unless they occur on the top edge of the facets.

A second example for the deviation from expectations was that the wafer numbered CWS19, from which all chips used in the experiments were picked up, was found to have generally thicker waveguides on chips located in the center region of the wafer, whereas thinner ones on those picked from the edge of the wafer [19]. This variance in waveguide thickness led to different attenuation, different radiation loss through curved sections, different butt-coupling loss and transition loss, and so on. As a result, the total insertion loss through the same kind of waveguide would be to some extent dependent on the original location of the chip and so it could be beneficial to know the distribution of the tested chips on the wafer, as referred to in Figure 2.7.

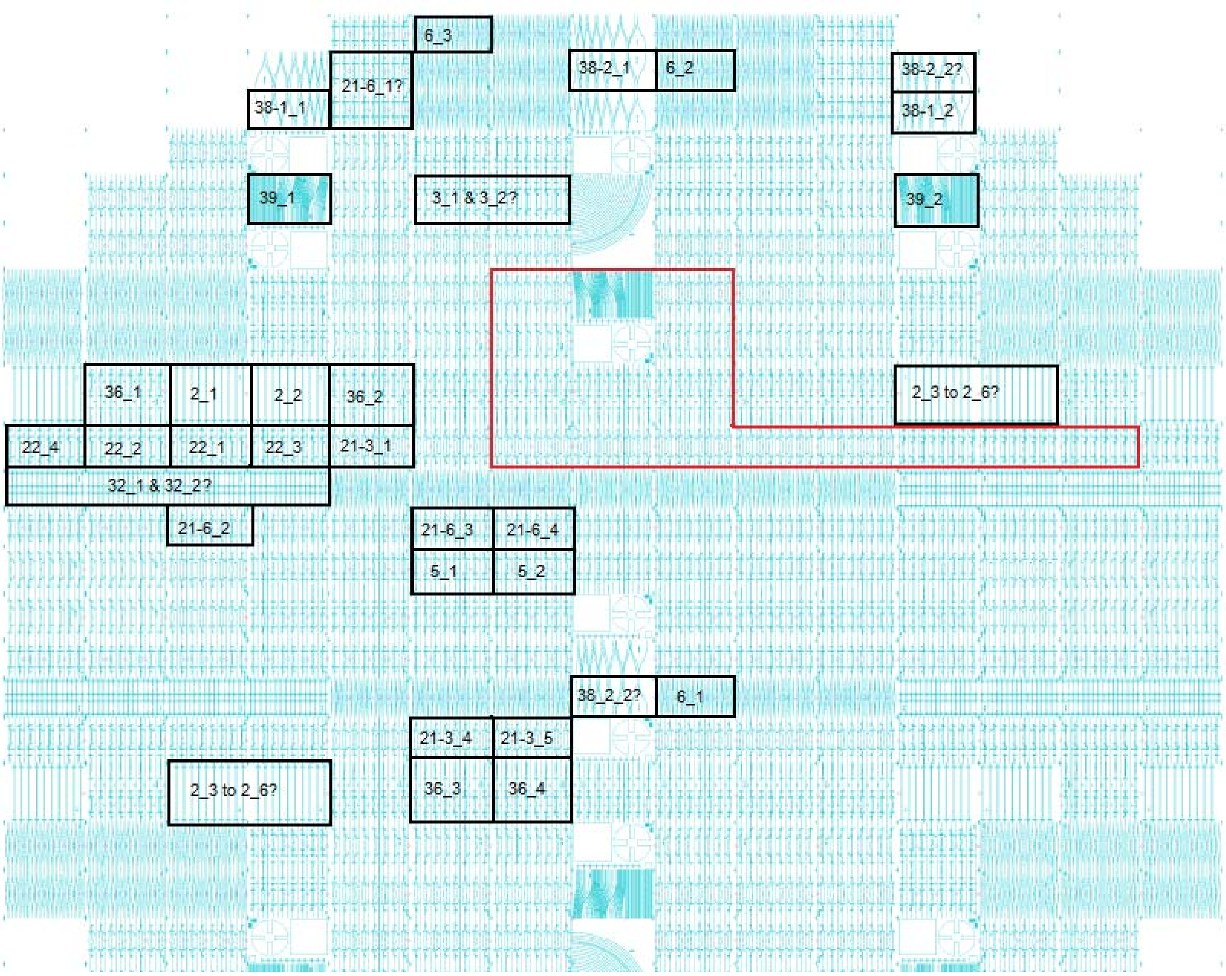

Figure 2.7: Distribution of the chips on wafer CWS19. All the words "DIE" in front of the chip number are omitted. The number behind the "_" mark indicates the sequence for chips of the same kind. The "?" mark means one of the possible locations of a chip. The red region is where chips shared with another student might be taken.

Moreover, it had been reported in other student's work that the Atomic Force Microscopy (AFM) result obtained from the chips produced for these experiments had shown deformation of the waveguides [18], changing the shape of their cross-sections and their equivalent width and thickness, causing them to generate different results from the expected values. What made things worse, the deformation was irregularly distributed on the wafer hence we could predict neither which waveguides were deformed nor how serious their deformations were.

2.3.3 Preparation of chip and laser before experiments

After cleaning and inspections, the chip should be mounted on the 3-axis positioner and fixed using double-side tape so that it would not slide too much when touched by fiber tips.

Laser power output stability was another important thing to check. We connected the Laser output port directly to the power meter input port and expect the readings to be stable enough -- the variations of optical power must be less than 0.1dBm. Usually, the fluctuation would not exceed 0.05dBm, as is represented in Fig 2.8. It should be emphasized that every time we connect and disconnect the Laser and the power meter, the fiber connectors should be cleaned using Q-tips dipped with IPA.

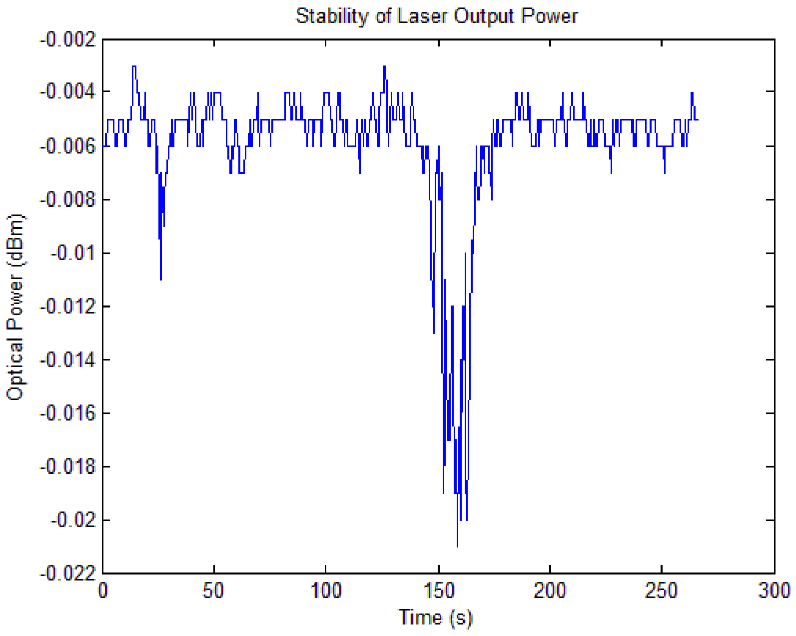

Figure 2.8: Stability of the Laser output power

2.3.4 Preparation of fibers before experiments

The fiber tips also need inspections, though just the low magnification microscope above the chip was good enough for this work. If there were defects along the fiber or if the cross-session of the fiber tip was apparently not perpendicular to the fiber axis, the fiber would need recleaving. To strip the jacket out of the fiber before the carrying out the cleaving, the fiber was immersed in Chloroform with which the plastic jacket would dissolve in 15 min, and then be removed with a stripper. The cleaving could be done by a fiber cleaver, whose manufacturer and model number was FITEL, S324. After cleaving, the fiber should be fixed onto a holder or a translation stage and wiped using Q-tips dipped with IPA.

The PMF used to excite a device under test needs to be polarization-aligned using a polarizer such that the electric field exciting the device would be vertical (TM-polarized).

2.3.5 Alignment

The alignment steps were as follows:

1) Get the image of the output side end-facet of the chip on the camera. This was done by adjusting the input side positioner so as to move the tip of PMF to the same x-y plane as the output side end-facet of the chip, and adjusting the output side positioner with the help of the infrared sensor card so that the MO cast the image of the PMF tip cross-section on the camera. At this time, the image of the output side end-facet of the chip should be on the same plane. Move the PMF tip back to the input side end-facet, then lift the chip up by adjusting the middle positioner. A bright band would soon be observed on the monitor screen. That was the image of output side facet of the chip.

2) Adjusting the roll axis of the middle positioner to make the upper surface of the chip horizontal. This was done by adjusting the middle positioner in x-direction so the chip moved in the same way, meanwhile observing the bright band on the monitor screen. If this band gradually went up or down, keep adjusting the roll axis properly until the band stayed at the same height on the screen of monitor as middle positioner moved in the x-direction. In this method, the chip and the PMF got aligned in the roll axis.

3) Adjusting the yaw and tilt axis of the input side positioner. For the yaw axis, move the PMF above the chip and observe from the microscope. Select one of the straight waveguides or one straight session of a waveguide as a reference. Keep adjusting the yaw and x axis of the input side positioner until the PMF and the selected straight waveguide became collinear in the microscope. For the tilt axis, move the PMF very close to the upper surface of the chip, which was regarded as a "mirror", observe the PMF and its image reflected by the "mirror" and adjust the tilt axis of the input side positioner till the PMF paralleled its image. In such a method, the chip and the PMF were aligned in the yaw and tilt axis as well.

4) On the output side, shift from MO to SMF. Adjusting the yaw and tilt axis of the output side positioner in a similar method. Now the yaw, tilt and roll axis were all properly aligned and did not need further adjustments.

5) Things would get much easier as we only need to align x, y, and z at this moment. Shift back to MO from SMF on the output side. Adjust the x, y, and z directions of both the input side and the output side positioners to get the LRSPP mode pattern on the monitor. The appearance of the mode pattern meant that the chip and the PMF were aligned in x, y, and z directions as well.

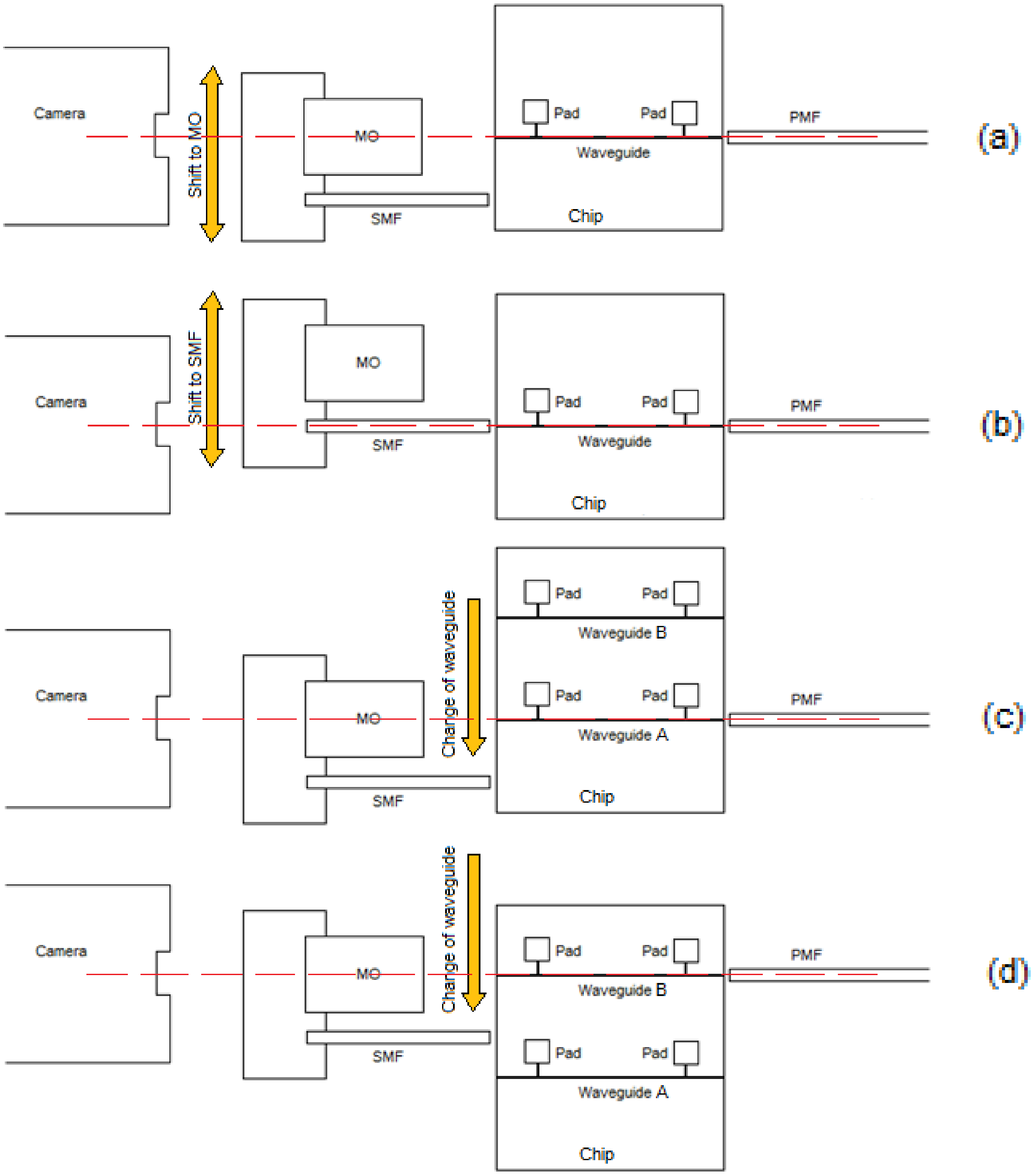

Figure 2.9: Fully aligned chip, PMF, SMF/MO, and camera. (a): Shift the translation stage to MO. (b): Shift the translation stage to SMF. (c): Alignment with waveguide A. (d): Change the alignment from waveguide A to waveguide B.

6) Finally, the task left here was to align the chip, the SMF, and the camera in the x, y, and z direction. Shift to SMF again on the output side. Adjust the x, y, and z axis of the output side 5-axis positioner to reach the highest value for the power meter readings. Then shift back to MO and adjust the location of the camera so that it caught the mode image again. By this time, the chip, the PMF, the SMF/MO, and the camera had been aligned in all 6 axes. We could shift between the MO and the SMF freely as well as change from one waveguide to another on the same chip by just moving the middle positioner in the x-axis without having to adjust any else axes. Figure 2.9 summarizes some of these alignments.

Thus the alignment process was complete. As we could see from the above, the initial alignment was very complicated but once it was done, the following work would become much more convenient.

2.3.6 Measurements and calibrations

Before measuring the loss of a waveguide, its LRSPP mode pattern should be found by moving the chip in the x and y directions. Once the mode was obtained, shift from MO to SMF to measure the output power value. Then shift back to the MO, change to another waveguide by adjusting the x-axis of the middle positioner again and find the mode for the new waveguide. The whole sample would be tested through repeat these steps. The main effort was spent in the initial alignment hence there were not many problems left in the measurement steps.

The values got from the power meter were only optical output powers. After testing the whole chip we need to bring the SMF and PMF close tip to tip and read a calibration power value. Subtracting the output power from the calibration power it would give the total loss through the waveguide.

There was a problem about recording the readings of the instrument manually. The power meter was so sensitive that the reading changed even when the experiment system was kept static and untouched. Variations usually exceed 0.1dBm. In the passive measurements, this problem was overcome by playing the output side positioner around when the SMF got close enough to the mode region. The better the alignment was, the higher the reading of the power meter would become. The acquirement of the highest power value meant that the best alignment had been reached. Therefore, the highest value reached during the "playing around" process was recorded as the measurement result.

The "playing around" method was just expediency, without solving the problem with the system stability. Judgements of the experimenter were needed in this method and so it could not be carried out automatically. For instance, when the fiber tips or the end-facet of the chip was contaminated by dusts, light passing through might be refracted and scattered, causing some abnormal readings on the power meter. The researcher could pick these abnormal readings out yet the computer could not. The problem of stability will be rediscussed and solved in Section 2.4 because thermo-optic modulations required automatic control using LabView programming. Nevertheless, the stability was not improved for the passive measurements because it would have been time-consuming.

2.4 Experimental methods for thermo-optic measurements

2.4.1 Attachment of chips

Methods for thermo-optic modulation experiments were generally the same as the passive measurements. However, since new elements were added into the system such as electrical probes and LabView, several new problems were introduced and corresponding improvements were made.

The first problem was the attachment of chips. In the passive measurements we used double-side tape to fix the sample chip onto the positioner, as mentioned in Section 2.3. But in the thermo-optic modulation experiments, the double-side tape was found unable to hold the chip firmly enough.

Referring to Section 2.1, in the thermo-optic modulations, electrical probes were attached upon metal pads so that electric current could pass through the active region of the waveguide. One issue of concern was the pressure of the probes exerted on the pads. Too light pressure usually led to bad connections between the probes and the pads, represented by severe changes in the readings for resistance of the waveguide. But as we increased the pressure, the chip would usually move before the connections improved, and the chip would become misaligned. Since the double-side tape was not strong enough to withstand the pressure of the probes, we replaced it with nail-polish. In this new method, nail-polish was put underneath or at the corners of the chip and the researcher had around 10 min to adjust the location. After 10 min the nail-polish congealed, keeping the chip at its place.

The nail-polish was stronger than the double-side tape, though less convenient to remove -- acetone had to be used in order to dissolve the nail-polish every time we changed to a new chip.

2.4.2 Method of alignment

The introduction of the probes also changed the method of alignment. As mentioned in Section 2.3, for the passive measurements, once the initial alignment was done, the chip, the PMF, the SMF/MO, and the camera were all aligned. For changing to another waveguide or making fine tuning for the alignment, only the middle positioner needed adjustments while the PMF and SMF/MO remained aligned and were just left untouched. Whereas in the thermo-optic case, as the probes pressing onto the chip, the initial alignment between the chip and the PMF would, anyway, be slightly changed thereby fine tuning would be necessary. But at this time, since the probes had been dropped onto the chip, the middle positioner could no longer be adjusted. Instead, it was the PMF that had to be adjusted for the fine tuning, as shown in Figure 2.10. This adjustment broke the initial alignment amongst the PMF, the SMF/MO, and the camera. At this moment, for recovering the alignment, we need to adjust either the SMF/MO or the camera, or both. However, due to the limitation of the setup system, it was difficult to adjust the location of the camera both frequently and precisely, whereupon we would have to adjust only the SMF/MO, leaving the camera untouched.

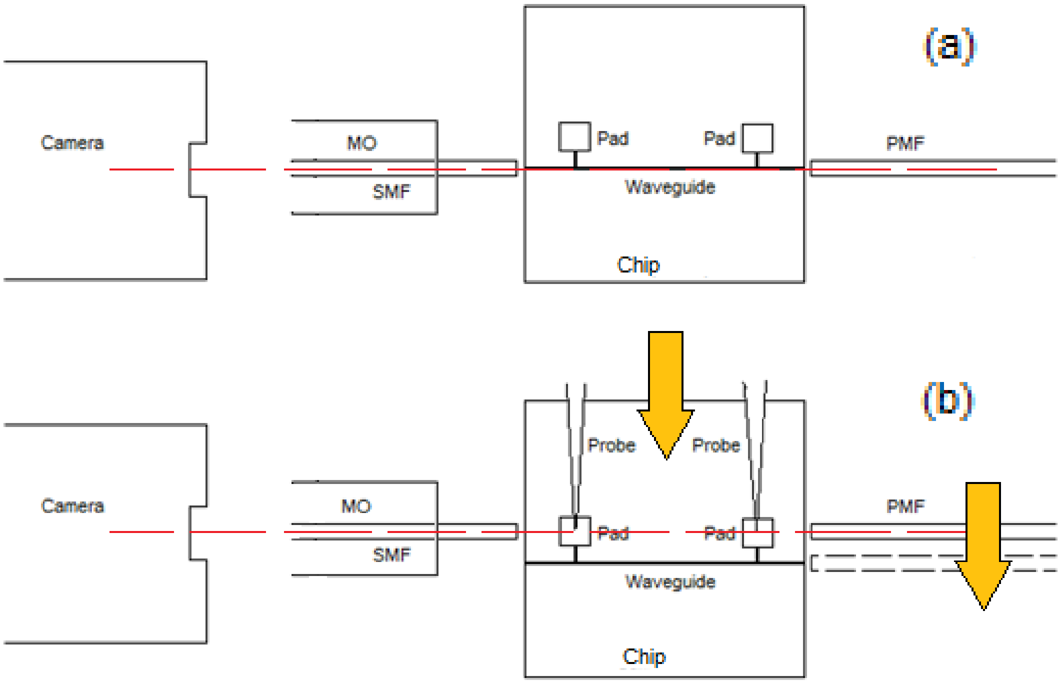

Figure 2.10: Slight misalignment caused by the probes and the realignment of PMF to the chip. (a): The original alignment. (b): The attaching of probes, moving of the chip, and realigning of PMF.

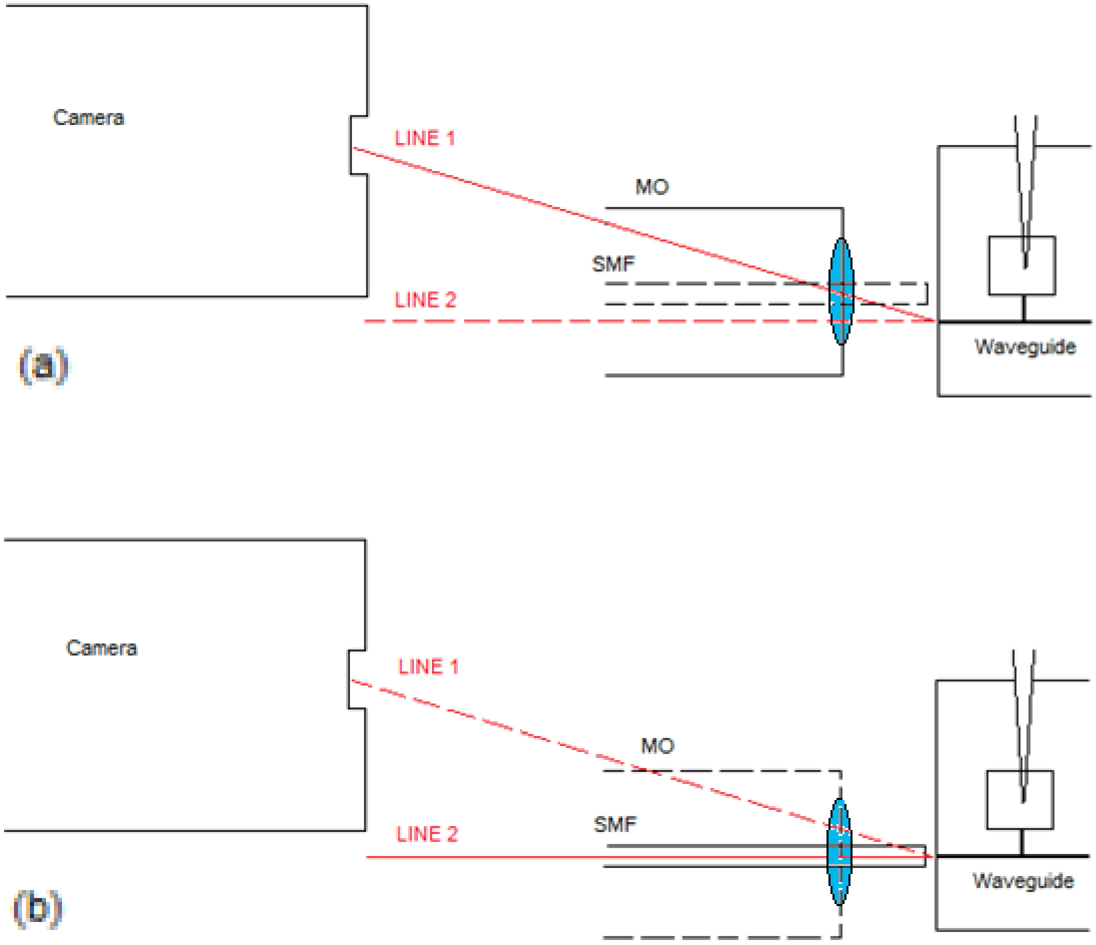

Figure 2.11: Different locations of alignment for the MO and for the SMF

(a): the MO case. (b): the SMF case.

With the changing of alignment method, a problem was brought about and illustrated in Figure 2.11. The location for proper alignment of the MO and that of the SMF were different, as could be observed by comparing Figure 2.11 (a) and (b). On one hand, for the alignment of the MO, the center of its front surface was supposed to be on LINE 1 in Figure 2.11(a) so that the output beam could be focused into the camera. Instead, for the alignment of the SMF, it was LINE 2 -- the extension of the straight waveguide that the SMF should to be collinear with, shown clearly in Figure 2.11(b). These two alignments were apparently not at the same place. As a result, when changing between the SMF and MO, we could no longer just shift forward and back as we did in the passive measurements, but had to more or less make some adjustments each time we shifted. Admittedly, even in the passive measurements some fine tuning would be necessary after the shifting. Nevertheless, the above-mentioned adjustments was at a higher order compared to the fine tuning, and after several turns of accumulation it might grow even larger, for the slight misalignment caused by the pressure of the probes were not random but directional.

This problem brought inconveniences to the experiments by increasing the time for completing the alignment and for finding the mode on the monitor. I once applied a self-designed setup structure to deal with this problem. The basic idea was to support the two extra probe-holding positioners with the middle positioner rather than using the optical table, in other words, to gain a linkage between the chip and the two extra positioners in order that they were able to move together. In this method, even after the probes had been pressed, we could still readjust the middle positioner without having the chip scratched by the probes since they were moving together, effectively avoiding the problem mentioned above. And now that the middle positioner could, again, be readjusted, correcting the misalignment would be as easy as it was in the passive measurement case. I named this designed setup structure “Scorpion” -- imagine the two extra positioners as two clips and the troublesome middle positioner as the poisonous tail, the whole structure standing under the observation microscope would look like a scorpion climbing up a tree! However, the Scorpion had unluckily a fatal disadvantage. The two extra positioners added such a heavy weight onto the middle positioner that its loading limitation was exceeded, which seriously affected the stability of the Scorpion structure (as discussed again quantitatively and graphically in the following paragraphs). In respect that a new positioner sufficiently sustaining this heavy weight could be too expensive to purchase, the Scorpion structure was given up, and thus in the thermo-optic experiments the above-mentioned inconveniences had to be accepted as they were. The Scorpion has proven to be an unsuccessful design, but still it is discussed here for its basic idea and the lessons learned.

Another possible solution to the problem might be improving the mechanism for moving the camera so that it could move precisely, since the problem originated from the difficulty of adjusting the location of the camera. To fix the camera on a positioner might be a sound idea -- though the camera was also heavy, it did not receive data but just helped find the mode, so the instability that might follow did not actually matter. There was, however, a problem that positioners were in short supply and always precious in the lab.

2.4.3 Power output readings

In the thermo-optic experiments it was necessary to draw curves that consisted of hundreds or thousands of data points for one single waveguide, making it impossible to do the task manually. LabView was introduced to automatically change the voltage provided by the power supply every few seconds or even half a second and record the readings acquired respectively from the multi meter and the power meter at that moment. This brought us a new problem. As discussed in Section 2.3, the readings on the instruments would fluctuate by about 0.1 dBm even when the system was left static. When recording the readings by hand, usually only the highest value appearing during a period of time was recorded as the result. Moreover, abnormal data were excluded based on the judgement of the experimenter. Such a task was unlikely, or rather difficult for a computer to carry out. Methods such as averaging the data had been tried but proved not quite effective. Accordingly, it was the improvements of the system stability that was needed in this case. The next section discusses this in detail.

2.4.4 Improvement of stability

The search for sources of instability and methods of dealing with them was a difficult and time-costing process, which will be discussed in sequence.

At the beginning, the SMF and PMF were aligned tip-to-tip for a calibration measurement. After proper alignment the setup was left untouched while the LabView program read the optical power output every half a second, drawing a curve of power versus time representing the stability of the calibration. In the first step, no improvements were made and the obtained power curve had a noise of about 0.8 dBm from the highest power to the lowest as can be observed in Figure 2.12(a). Besides, it showed that the noise was constituted by a higher frequency noise as there were sharp peaks added onto the profile of the noise curve.

Then a plastic tent was built to cover the setup and to protect it from environmental air flows led by ventilations, passing people, etc. The power curve is given in Figure 2.12(b), from which little improvements could be found -- the noise was about 0.7 dBm within 3 min. In order to compare the stability more quantitatively, a new parameter was added in -- the variance for all the data points contained in the curve was calculated. The smaller the variance was, the better the stability would be. In this case, the variance was about 0.028. But still, there was one thing noticeable -- it seemed that the frequency for the higher frequency noise had been lowered.

On the optical table there laid the Laser diode current source and the temperature controller for the Laser, whose fans might have worsened the system stability. I removed these instruments from the table so as to exclude the effects of the fans. Figure 2.12(c) shows the result -- the noise decreased to about 0.6 dBm and the variance was 0.021, a little better than the previous time.

Next, the fiber tips exposed out of their chucks were too long to remain stable. On one hand, they should be cleaved short, but not too short because it might become difficult to aligned to the waveguides. As mentioned in Section 2.3, in the alignment process, the tip of the fiber was moved on top of the chip, overlapped with one straight waveguide looking from the observation microscope hanging above, and adjusted to parallel its image in the “mirror”. If this section of fiber was too short, it would be difficult for the experimenter to judge the overlap and the degree of parallelism. For this reason, I left about 0.5 mm out of the chuck for each fiber. Data in this case are shown in Figure 2.12(d). The variance dropped to 0.011 and the optical power varied for about 0.4 dBm this time, better but still quite larger than 0.1 dBm as was required.

The most important breakthrough was made by adding refractive index matching oil between the fiber tips and the end-facets of the chip. The oil that had the closest refractive index to the core region of the fibers n=1.4474 [23] was selected. The chosen oil was produced by Cargille Laboratories with a refractive index of 1.456. Clearly from Figure 2.12(e), the optical power varied for about 0.06 dBm, fulfilling the requirement of less than 0.1 dBm, and the variance went down much further to 0.0002. A prominent change that could be noticed here was that the higher frequency noise had decreased to a lower level in magnitude compared to the lower frequency noise, unlike what was shown in the earlier results that the two noises were of more or less the same order. This is probably because that the higher frequency noise was generated from the Fabri-Perot cavity, which was formed between the fiber and the device end-facet and was removed by filling in the refractive index matching oil.

After this breakthrough I wanted to examine whether the plastic tent isolating the setup did play a role in minimizing the noise. If not, it should be removed to facilitate experiment operations. In this turn the tent was opened and results showed that the variation of the power increased to about 0.2 dBm with the variance rose to 0.003 as is shown in Figure 2.12(f), meaning that the tent was really indispensable.

Hereby the readers should keep two things in mind. Firstly, the Scorpion structure introduced above was still in use when the above tests were made. Secondly, all the experiments above were calibration measurements. In the next step, we turned to insertion loss measurements, which were done by adding the chip to the setup and connecting probes to the chip without passing current through them. The insertion loss measurements might have lower stability than the calibration measurements for the probes could conduct the vibrations of the two overweighed extra positioners onto the chip, and the vibrations would give rise to instantaneous misalignments. Accordingly, similar curves were drawn for the insertion loss measurements and results are represented in Figure 2.12(g). This curve looked like Figure 2.12(e) added by a few sharp drops with the depth of about 1 dBm, indicating that the system stability had been severely worsened. As was discussed before, this degradation was understandable since the middle positioner had sustained heavier weight than its loading capacity. After disassembling the Scorpion and fixing the two extra postioners to a support seated on the optical table, another stability test for the insertion loss measurements was made and the results were illustrated in Figure 2.12(h), showing a disturbing decreasing trend with a variation of 0.25 dBm and a variance of 0.005 probably caused by the drifting of refractive index matching oil and the mechanical drift of the positioners. Admittedly, this result was not perfect, but already the best stability that could be reached on the setup we had, so I stopped the stability improvement research. Finally, for validation, the chip was removed and the two fibers were aligned to make an additional stability test for calibration shown in Figure 2.12(i). We see that without the Scorpion, the power variation was 0.05 dBm and the variance was 0.0001 -- both suggested perfect stability for this calibration measurement.

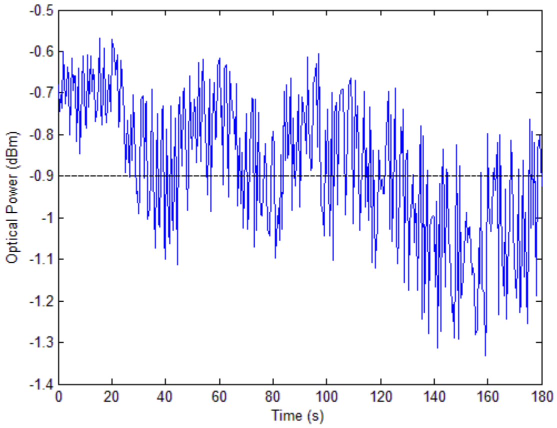

(a) Before improvements were made

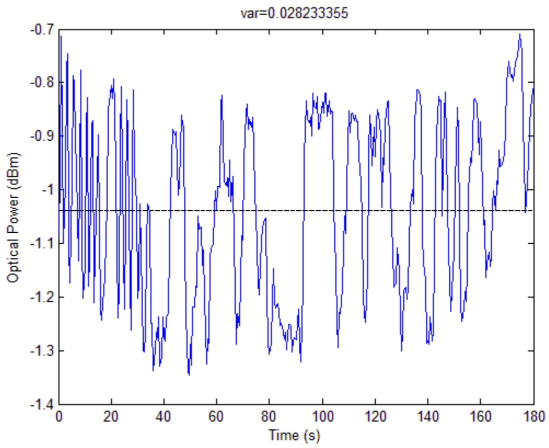

(b) After building a plastic tent

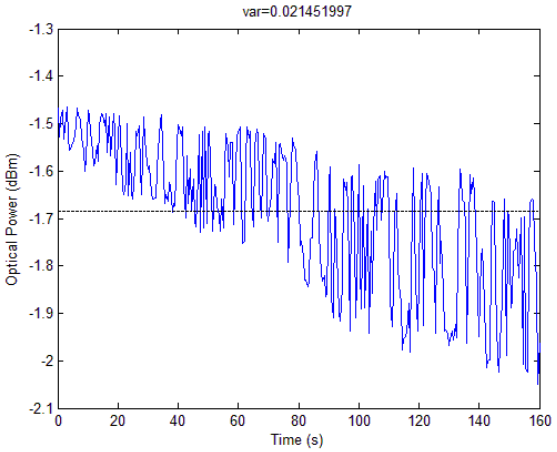

(c) After removing the fans

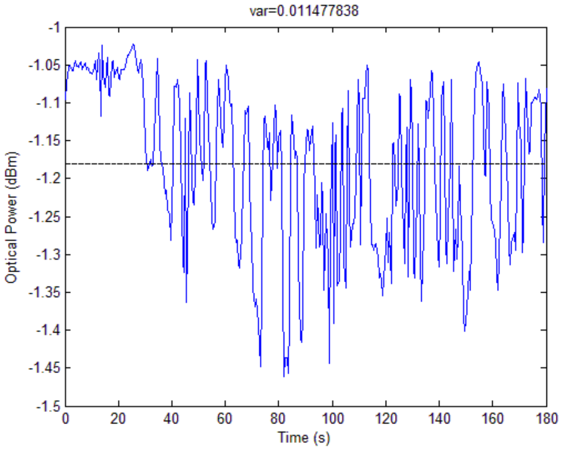

(d) After cleaving the fibers

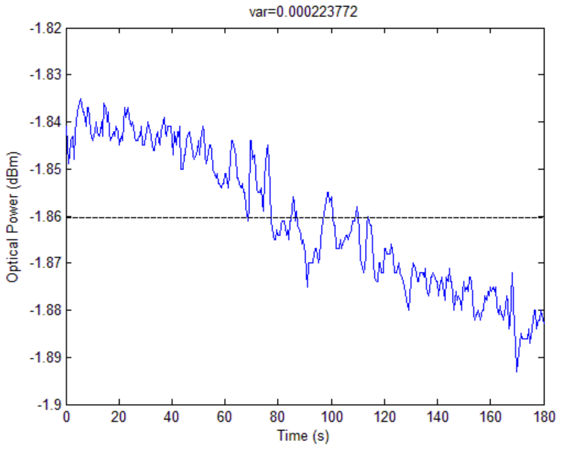

(e) After adding refractive index matching oil

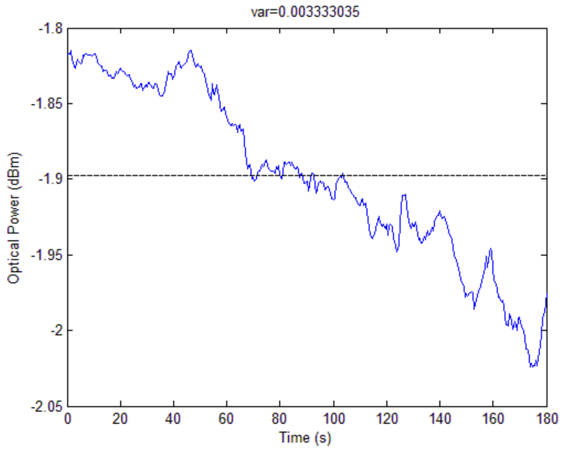

(f) After opening the tent

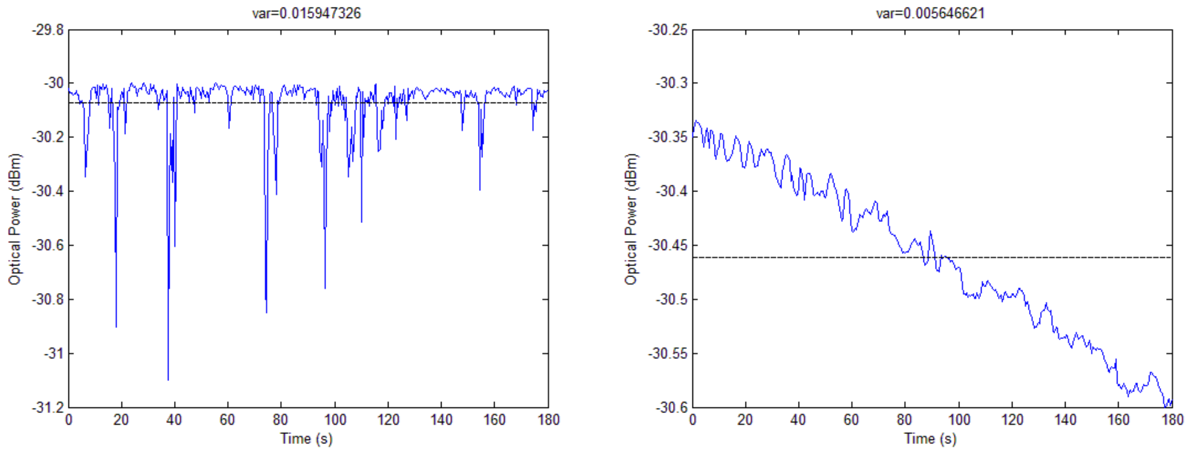

(g) Insertion loss measurement

(h)After removing the weight from the positioner

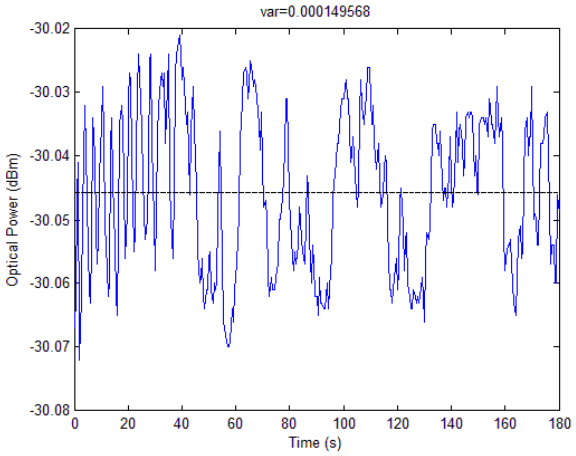

(i) Calibration measurement for validation

Figure 2.12: Improvement of stability

2.4.5 Improvement of thermal conductivity

During the thermo-optic experiments, another problem was found. The thermal conductivity between the sample chip and the middle positioner was not high enough resulting in an accumulation of heat inside the chip that affected the experiment results.

To deal with this problem, a Thermo-Electric Cooler (TEC) and a jig were added between the chip and the middle positioner. The jig was designed to be porous so it had relatively larger cooling surface area favouring the dissipation of heat, and was fixed to the middle positioner using Instant Krazy Glue. The TEC was stuck to the porous jig by Epoxy which served both as the glue and as a thermal conductor. Wires connected the TEC to a temperature controller so that the controller could pass current through the TEC to cool or heat it, keeping its temperature at the preset level. At one corner of the TEC we used Instant Krazy Glue to fix a thermistor there, which was connected to the temperature controller as well, enabling it to sense the temperature of the TEC. After these were settled, the chip was put onto the TEC with a layer of Silicone heat transfer compound (Catalogue Number: 860-150g) in the middle of them. This compound was well heat-conductive and could improve the thermal connection between components and heat sinks so that heat accumulated in the substrate of the chip could be quickly dissipated into the TEC. But it was not sticky enough to hold the chip firm on the TEC so we would still need to add nail-polish at the corners of the chip.

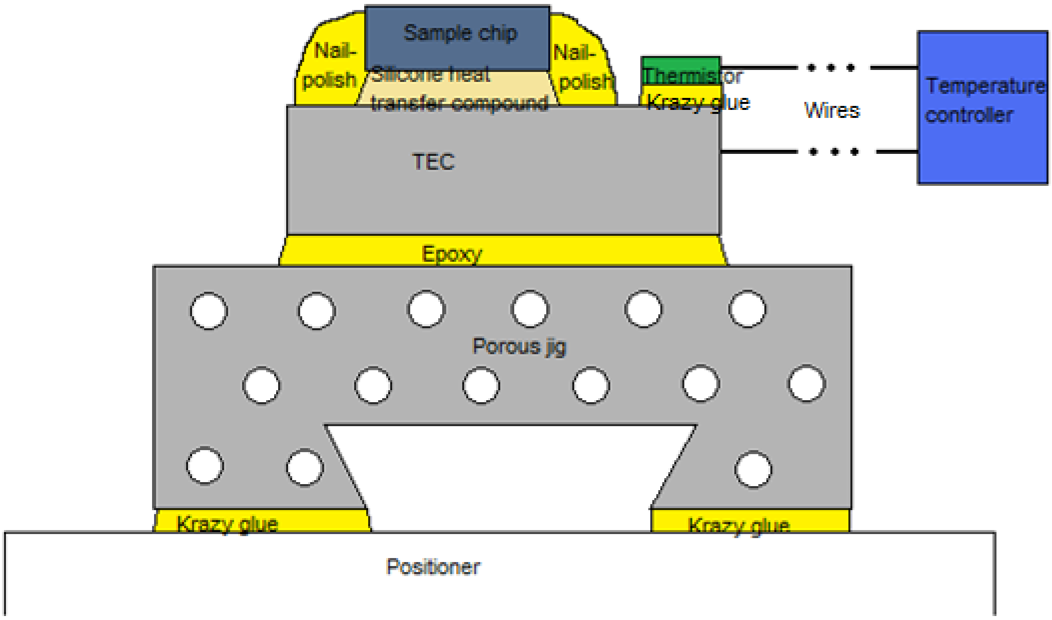

Figure 2.13: Improvement of thermal conductivity

After these improvements, heat generated in the active region of the chip could quickly pass through the Si substrate, the Silicone heat transfer compound below the chip, the TEC, the Epoxy, and get dissipated at the porous jig and the positioner, as is illustrated in Figure 2.13. But these improvements could not help when heat produced in the gold waveguides was passing through the CYTOP claddings, which has a rather smaller thermal conductivity of 0.12 W/(m·K) compared to 30 W/(m·K) for gold and 145 W/(m·K) for Si [11]. Nevertheless, the bottom CYTOP cladding layer was only 10 μm thick, to some extent compensating for its low thermal conductivity.

3. Passive measurements

The work in Chapter 3 is mainly to compare the measurements of passive elements with theoretical expectations generated by other researchers to see whether the design and the fabrication of the tested devices are of good quality.

3.1 Cutback measurements

The first step is to determine two basic waveguide parameters -- butt-coupling loss per facet and attenuation per mm, which can be obtained from cutback measurements.

The cutback measurements were carried out by measuring the insertion loss (in dB) of straight waveguides of different length (in mm) and fitting the length-loss data points to a straight line. The Y-intercept would be the total butt-coupling loss of two facets and the slope would be the attenuation per mm. In the cutback measurements 52 waveguides of 3 different lengths were tested; some of the results are shown in Figure 3.1.

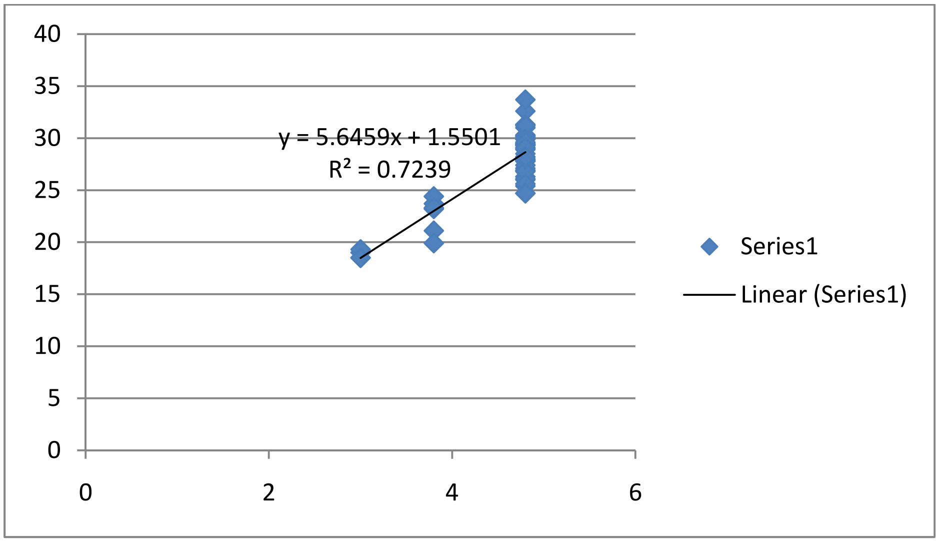

Figure 3.1: Cutback measurements

X-axis: waveguides length (mm), Y-axis: total insertion loss (dB)

From this cutback measurement it could be calculated that the butt-coupling loss was about 0.78 dB/facet and the attenuation was 5.6459 dB/mm, both of which were far from the theoretical expectations, which were 0.8936 dB/facet and 7.1776 dB/mm [22], respectively. However, we could also see that the data points of this cutback measurement were so scattered that its reliability was low -- the R^2 was 0.7237, much smaller than an acceptable value 0.9.

There could be three possible causes for this: the dependability of my measurement skill, the validity of the design of these devices, and the quality of their fabrication. The first one will be discussed in Section 3.7, proving that the dependability of my measurement skill was acceptable. For the rest two possible causes, the problem was more likely to lie in the quality of the fabrication, as we have discussed in Section 2.3. Firstly, even the best waveguides had visible defects based on the record of inspection comments. Secondly, some of them might have damages on the end-facets, the quality of which could not be observed during inspection. Thirdly, the thickness of waveguides located on different regions of the wafer was not consistent, for the gold layer tended to be thicker in the center of the wafer while thinner near the edge. Besides, the prevalence of deformation amongst the waveguides reported by AFM tests [18] were irregular, making waveguides even on the same chip or in the nearby region deformed differently in type and extent, and therefore become less comparable with each other.

In summary, due to the low quality of the sample chip, the above cutback measurement could not generate reliable enough results of butt-coupling loss per facet and the attenuation per mm.

3.2 Relation between attenuation and width

DIE39_1 was tested to draw some curves of loss versus width. Based on theoretical expectation, the wider the waveguide was, the higher its attenuation would be.

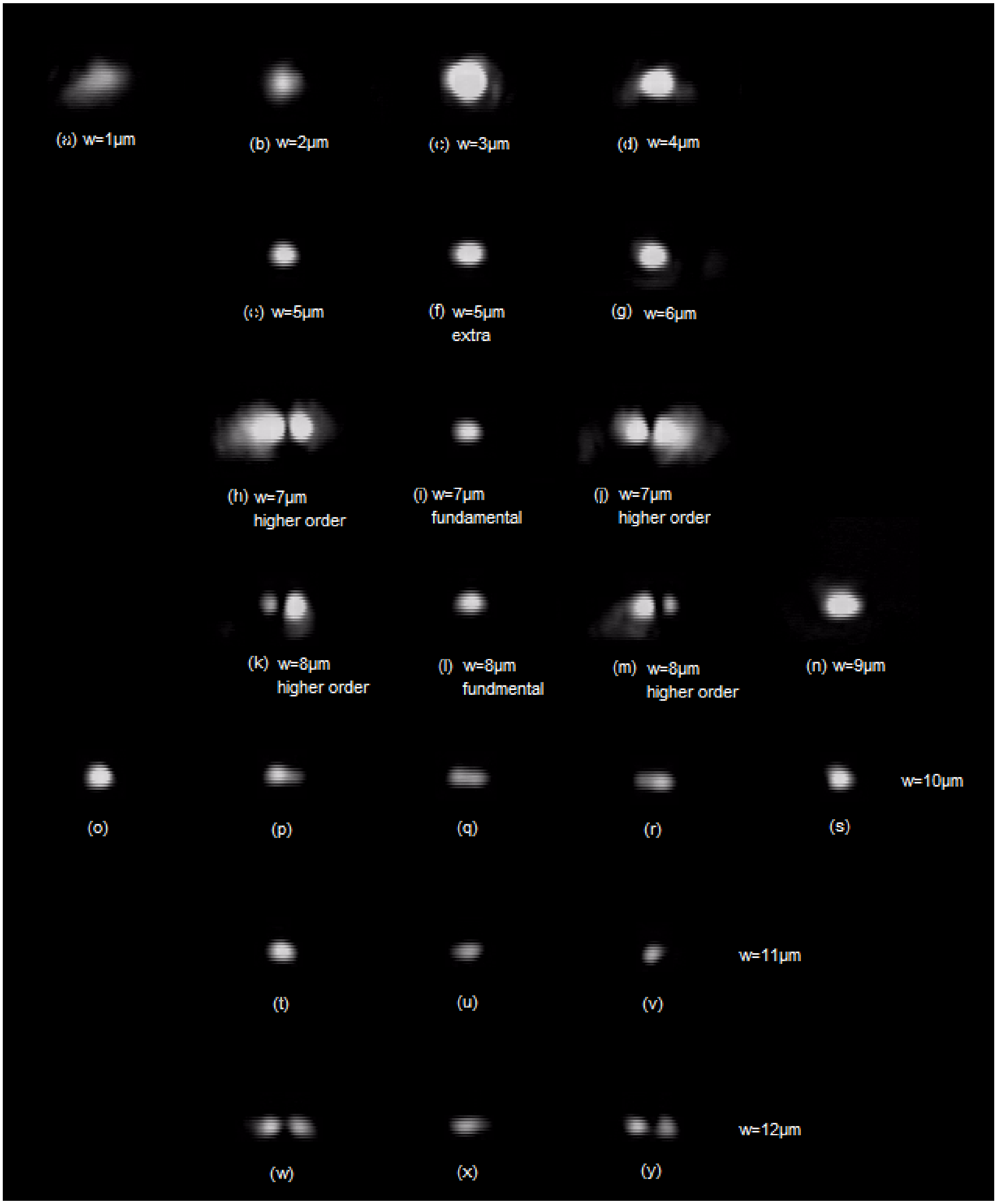

Figure 3.2: Mosaic of mode outputs of straight waveguides of different widths

Figure 3.2 represents the mode appearances of straight waveguides of different widths. Figure 3.2(a) and (b) are modes for width=1μm and 2μm. These two modes were so bright that they were taken under much higher optical density filter (making the modes dimmer) than other modes so as not to damage the CCD camera. Figure 3.2(c) and (d) are modes for width=3μm and 4μm. (e) and (f) are both for 5μm because there was an extra 5μm wide waveguide in one group, while (g) is for 6μm waveguide. From (a) to (g) the mode was gradually getting dimmer as the waveguide width increased.

Figure 3.2(h) to (j) are modes taken for width=7μm. From this width forward, the waveguide had gone wide enough for higher order modes, as mentioned in Section 1.4. Figure 3.2(i) should be the fundamental mode for width=7μm, and (h) and (j) were a higher order mode excited by slightly misaligning the input fiber leftward and rightward. The higher order mode seemed to have two lobes.

Figure 3.2(k) to (m) are modes for an 8μm wide waveguide, taken similarly as the 7μm wide waveguide. (n) is for 9μm wide waveguide, for which width no higher order mode was found. (o) to (s) are for 10μm, (t) to (v) are for 11μm, and (w) to (y) are for 12μm. Because that the higher order modes had appeared, the 7μm wide waveguide and those wider were not measured in the experiments.

The curves of total insertion loss versus width are illustrated in Figure 3.3. The general trend of these curves was that the total insertion loss rose up as the waveguide width increased. A theoretical expectation curve for thickness=35nm was drawn and had the same trend with the measured results, but stood much higher to them. Since the attenuation contributed most of this insertion loss, we could say that the attenuation of these waveguides was much lower than expected theoretically. This suggests that the tested waveguides were thinner than 35nm, the thickness they were designed to be.

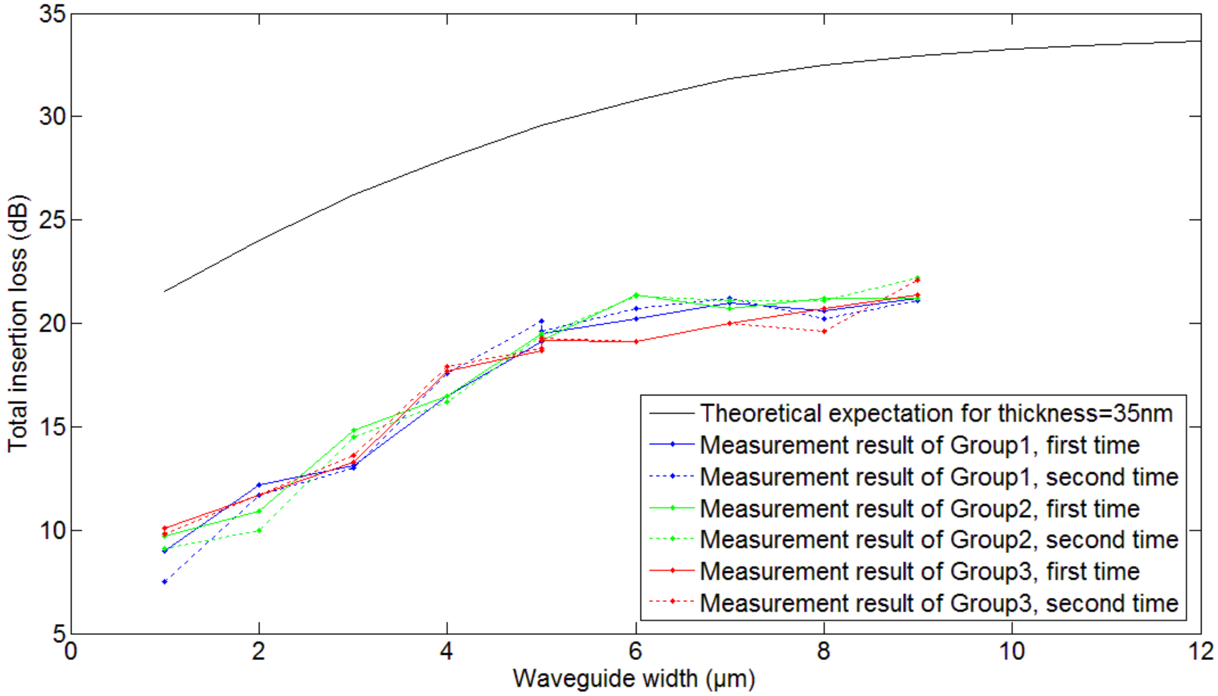

Figure 3.3: Curves of total insertion loss versus width

3.3 S-bends

The other half of DIE39 was packed with S-bends of different radii of curvature which would cause different radiation loss. These S-bends needed to be tested and the data could be drawn into a loss versus radius curve. Theoretical results indicated that larger radii of curvature would have smaller radiation loss.

Figure 3.4: Mosaic of mode outputs of S-bends of different radii of curvature

Figure 3.4 shows the mode mosaic for waveguides of different radii of curvature. The radii for each mode had been marked below the picture. Figure 3.4(a) was taken without the optical density filter because otherwise this mode was too dim to be caught by the CCD camera. These pictures generally corresponded with the theoretical prediction that as the radius increases the mode will become brighter. One exception is Figure 3.4(j), which was unexpectedly dim. This was due to serious defects recorded in the inspection comments.

Figure 3.5(a) and (b) are two groups of data measured on DIE39_1 and DIE39_2 respectively, showing the relation of total insertion loss versus radius of curvature of S-bends. The theoretical curves were computed by linearly combining the existing curves of radiation per 90˚ for 30nm (attenuation 4.4448 dB/mm) and 35nm (attenuation 7.1776 dB/mm) thick waveguide [22] given the estimateed attenuation, transforming into curves of total radiation loss, and adding the estimateed butt-coupling loss, the estimateed attenuation multiplied by pathlength, and the transition losses (transition losses for 35nm thick waveguide were used here but this will not cause too big an error). The estimateed butt-coupling loss per facet and attenuation for the theoretical expectation curves were carefully chosen so that the measured data points distributed on both sides of the curve. In Figure 3.5(a), the measured data fitted the theoretical curve with butt-coupling loss 0.35dB/facet and attenuation of 5dB/mm, while in Figure 3.5(b) these two parameters changed to 0.3dB/facet and 6dB/mm. The difference between these two pairs of parameters shows again the inconsistency of waveguide thickness on the wafer. We could see that the two attenuation values 5dB/mm and 6dB/mm were both smaller than the attenuation for the designed waveguide thickness 35nm, and consistent with the cutback measurements of Figure 3.1. Theoretically, thinner waveguide had lower attenuation. This meant that the waveguides on both chips were thinner than the designed thickness, strengthening the conclusion drawn at the end of Section 3.2.

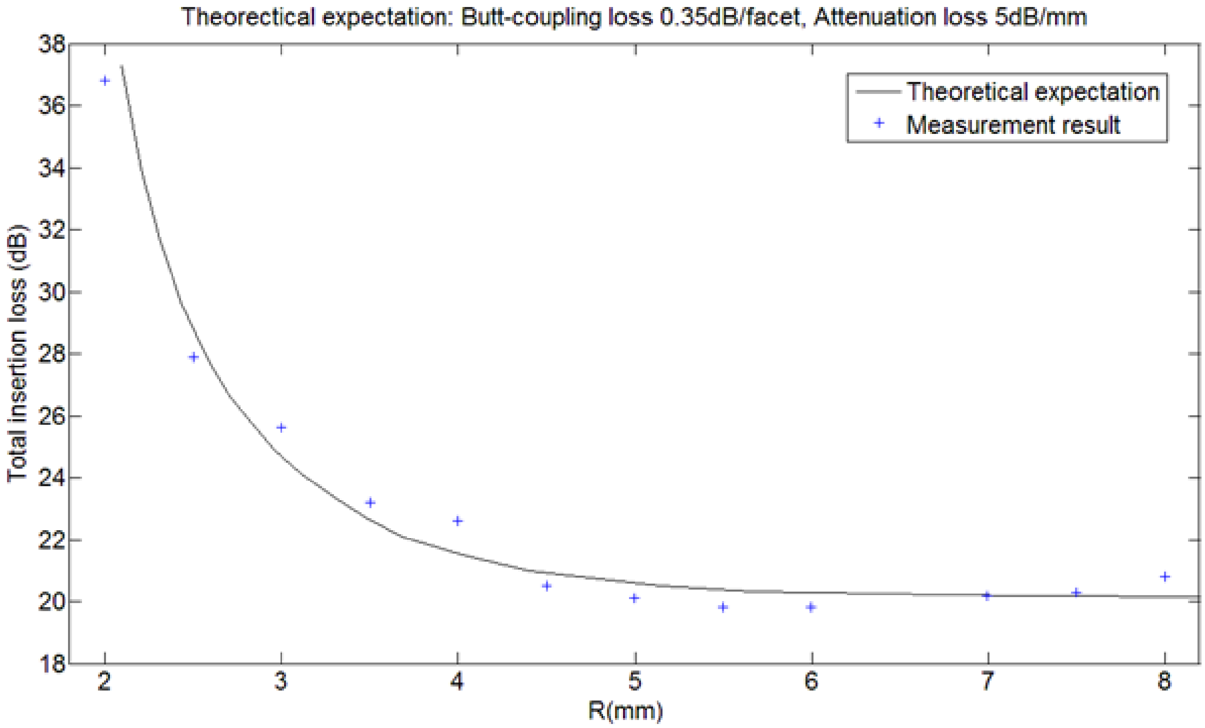

(a) DIE39_1

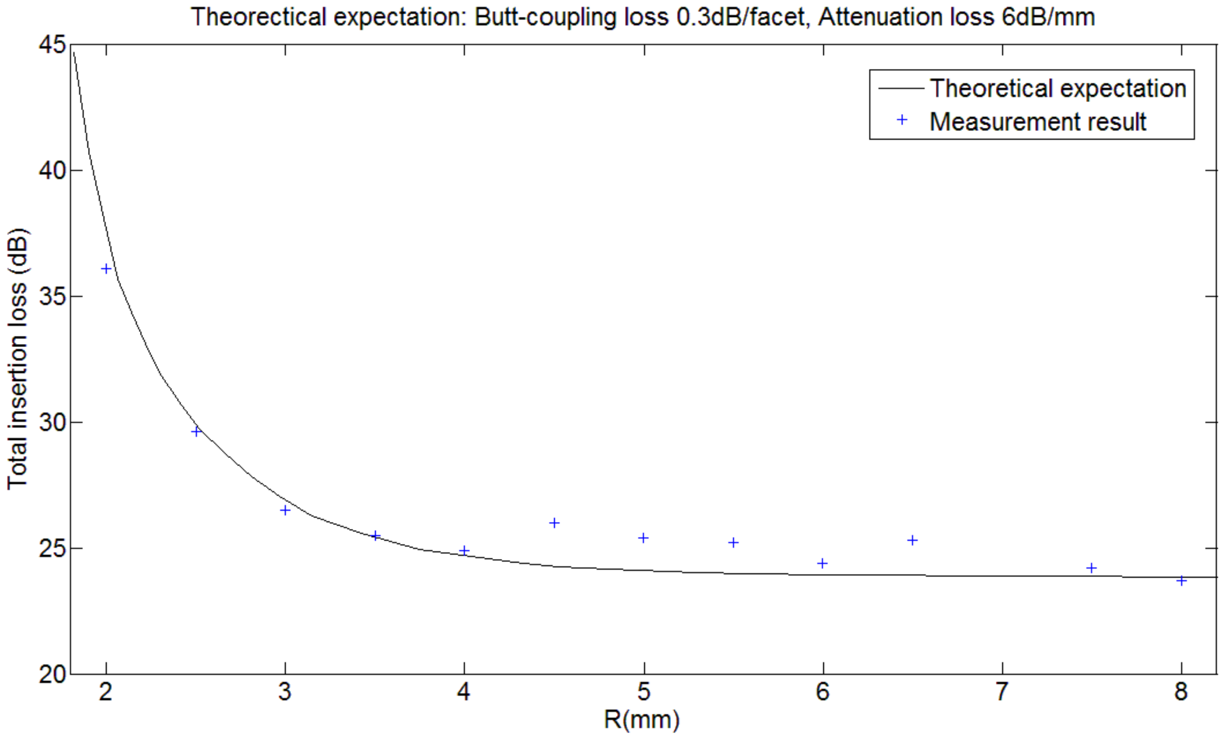

(b) DIE39_2

Figure 3.5: Curves of total insertion loss versus radius of curvature for S-bends

3.4 Y-junctions

Y-junctions divide the input into two equal outputs. They were designed from an overlapping mirrored-pair of S-bends. Therefore their loss-versus-radius relation should be similar to that of S-bends. The difference was that Y-junctions had an extra transition loss at the junction structure.

Figures 3.6(a) and (b) represents the mode mosaic of Y-junctions of various radii of curvature for Y-junctions having a 1μm (DIE38-1_1) and 2μm (DIE38-2_1) wide gap respectively. Similarly to the S-bend case, the mode became brighter as the radius increased. Figure 3.6(a) also contains pictures of the scattered light in between the two outputs showing on the right side of the picture. It is observed that the larger the radius, the less the scattered light, in accordance with theorectical expectations.

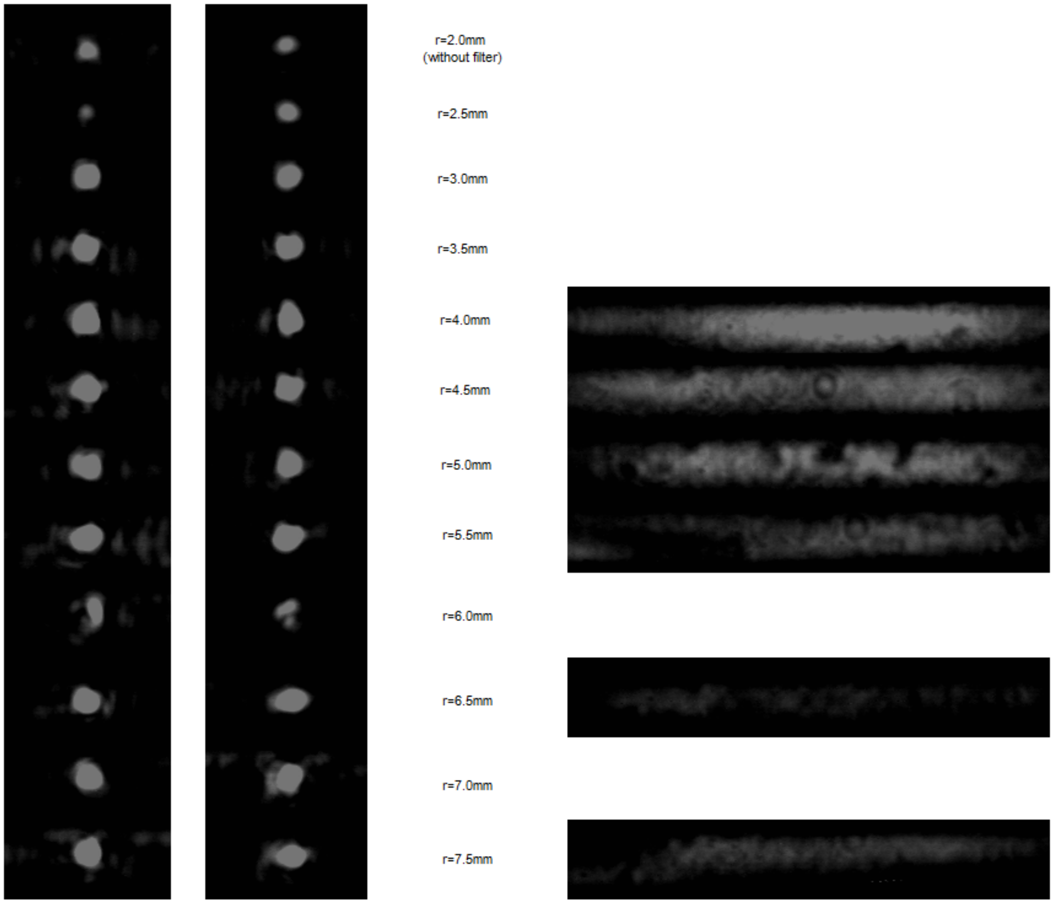

(a) DIE38-1_1, junction wide=1 µm

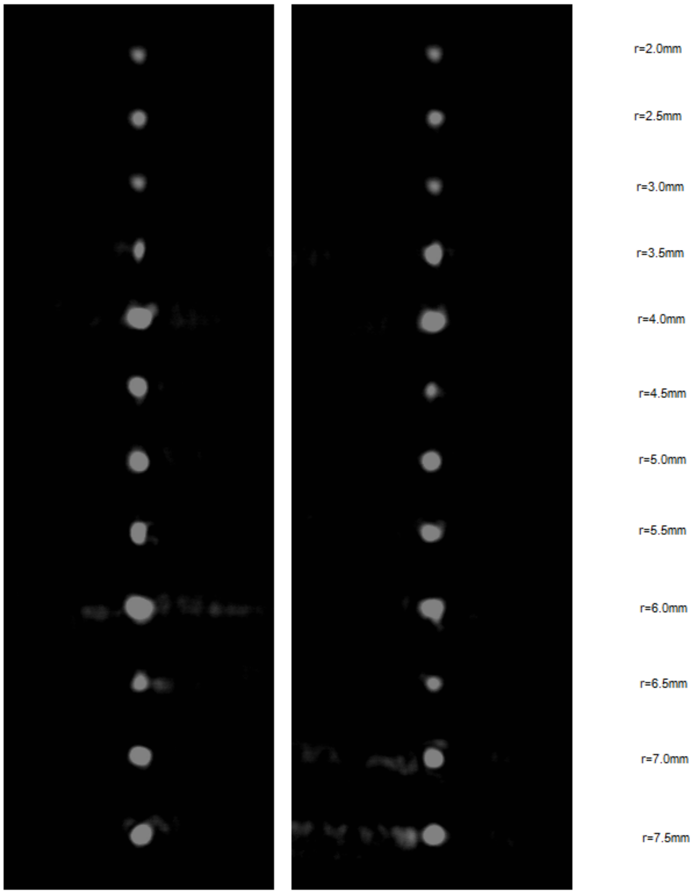

(b) DIE38-2_1, junction wide=2 µm

Figure 3.6: Mosaic of mode outputs of Y-junctions of different radii of curvature

Figures 3.7 (a) and (b) give plots of total insertion loss versus radius of curvature for Y-junctions 1µm (DIE38-1_1) and 2µm (DIE38-2_1 and DIE38-2_2) wide respectively. The butt-coupling loss per facet and the attenuation for the theoretical expectation curves were chosen in the same way as in the S-bends case. The two parameters for both of the above two cases were 0.3dB/facet and 4.8dB/mm. The value of the attenuation indicated that the waveguides on these three chips were also thinner than designed. It can also be observed from the pictures that the Y-junctions tested in the experiments were well-balanced, for both output powers are similar to each other.

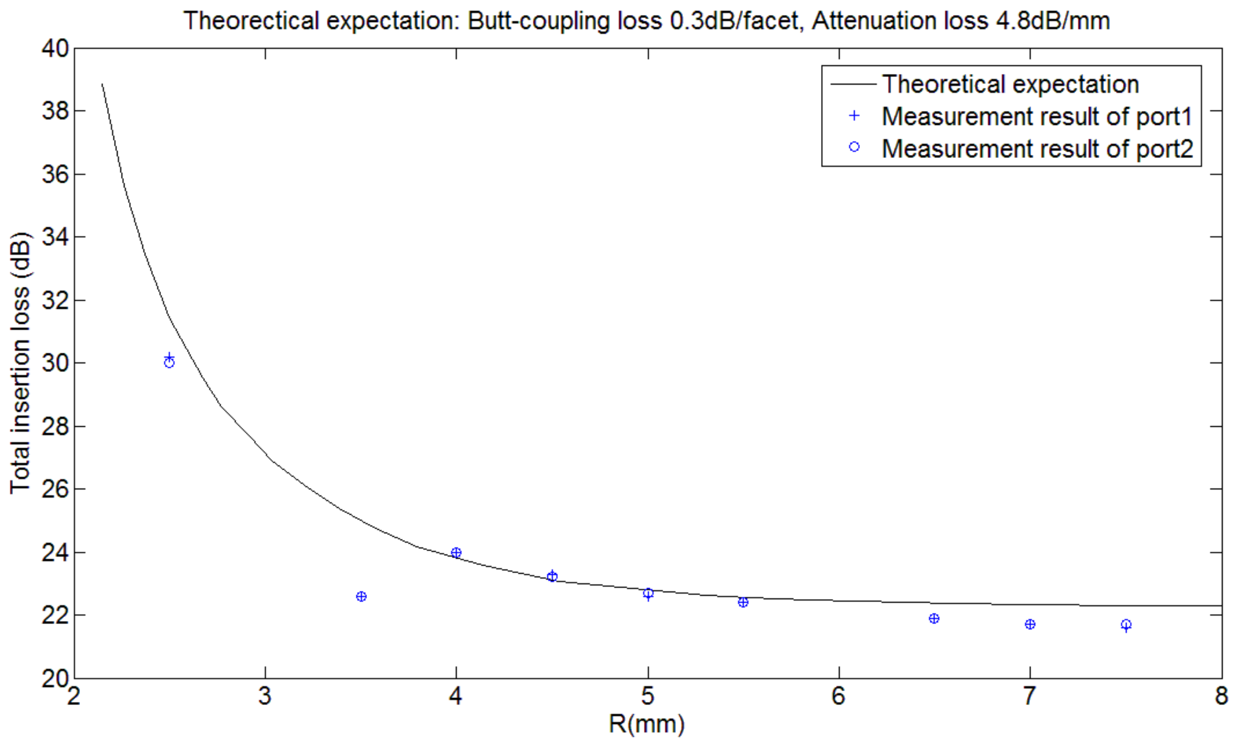

(a) DIE38-1_1, junction wide=1 µm

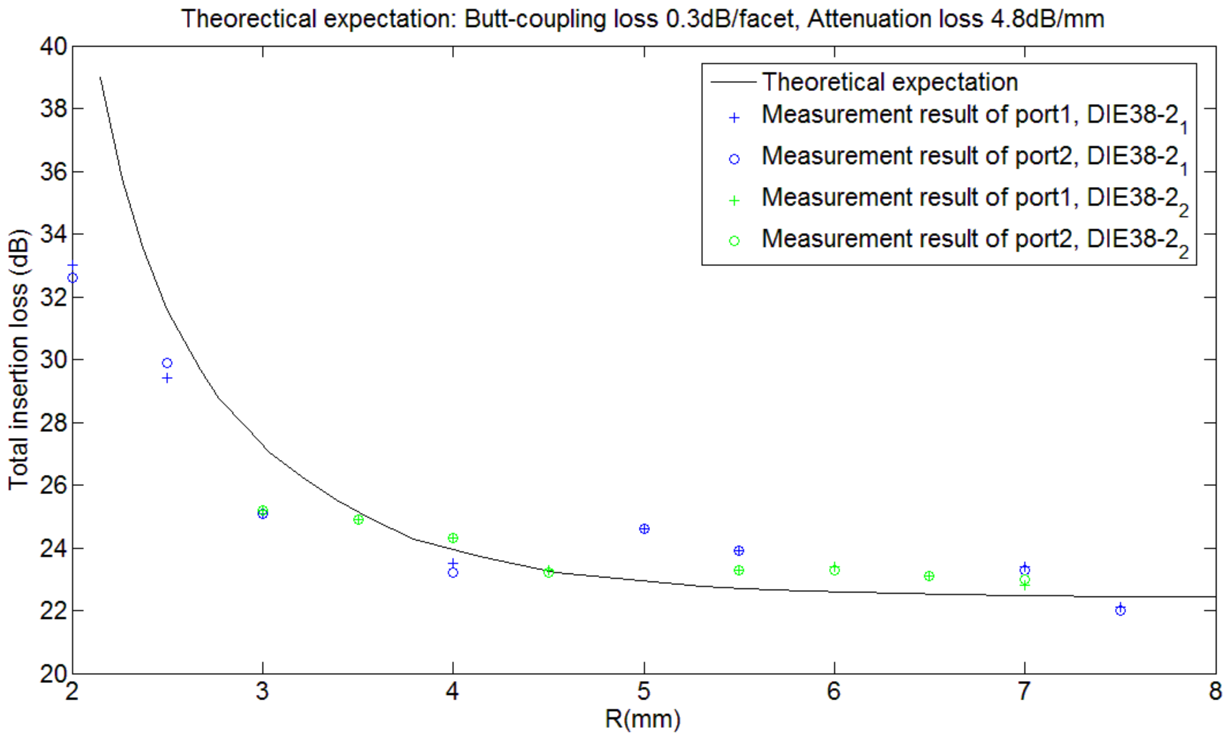

(b) DIE38-2_1 and DIE38-2_2, , junction wide=2 µm

Figure 3.7: Curves of total insertion loss versus radius of curvature for Y-junctions

Figure 3.8 makes a comparison between the measured results for S-bends and Y-junctions to see how their relationship meets the theory. Based on theory the insertion loss curve for Y-junctions should be more than 3dB higher than S-bends because the output power of one port of Y-junctions was only half of the output power of S-bends, plus an extra transition loss at the junction part, just as was discussed at the beginning of Section 3.4. Moreover, the curve for 2μm Y-junctions should be a little higher than that of the 1μm Y-junctions, because 2μm junctions would cause more transition loss. Observing Figure 3.8 we would discover that for higher radii of curvature the measurement fit the theoretical prediction, although not quite well, while as the radius went down, the curves got entangled with each other instead of dividing into groups. The reason why the errors happened mainly in the lower radius region is yet to be further explored.

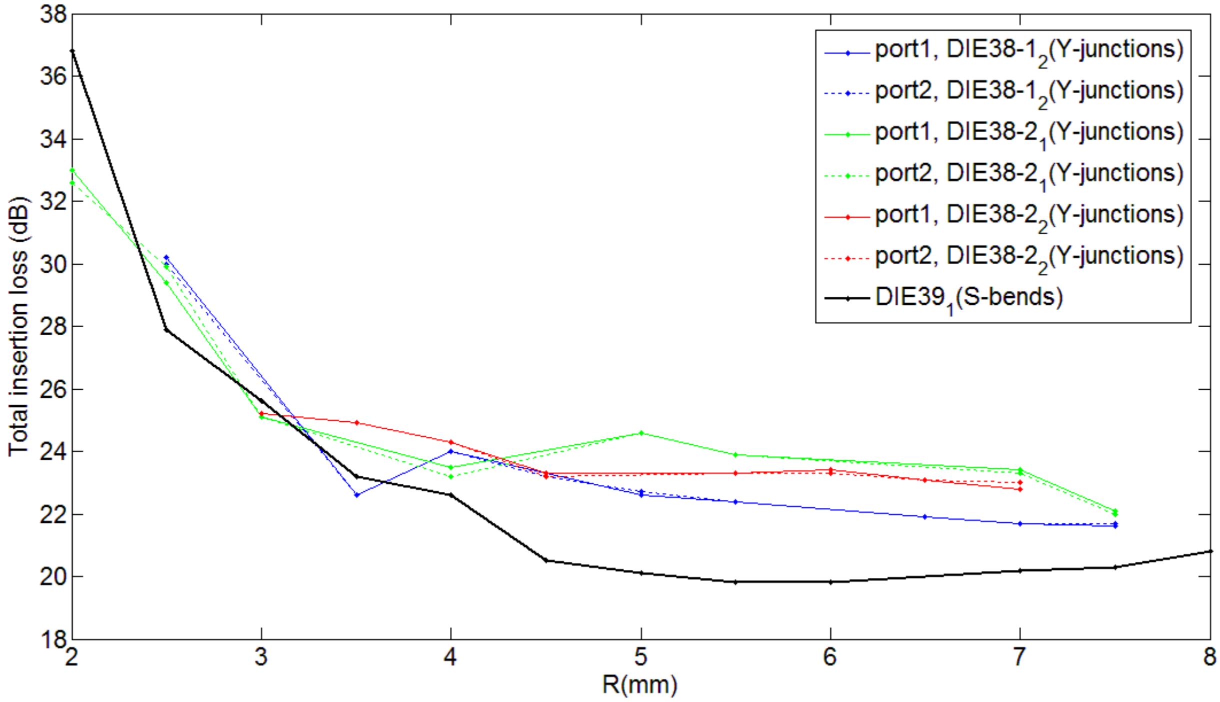

Figure 3.8: Comparison between measured data of S-bends and Y-junctions

3.5 Mach-Zehnder interferometers (MZIs)

The MZIs were designed as a combination of straight waveguides, S-bends, and Y-junctions. Thus we can make predictions on the total insertion loss of the MZI using the theoretical expectation values for butt-coupling loss per facet, attenuation, and radiation loss [22]. However, in the discussions of the above passive structures it was discovered that different chips would have different performance because of the prevailing deformations and defects on this wafer, for instance, the attenuation ranged from 4.8dB/mm to 6dB/mm.

L=3.0mm, center waveguide separation=140um		
1	20.9 dB	1 twisted part on the left
2	22.7 dB	very bad rotting parts near the 2 pads on the left
3	22.2 dB	perfect
4	19.7 dB	perfect
5	29 dB	1 twisted part each on both Y-junctions, long twisted part on curved sections, 1 twisted part on the right
6	27.6 dB	1 twisted parts each on both Y-junctions, long twisted part on curved sections
7	27.7 dB	1 twisted parts each on both Y-junctions, long twisted part on curved sections
8	28.8 dB	1 twisted parts each on both Y-junctions, long twisted part on curved sections, and small crackles like wrinkles near the left facet
9	33 dB	1 twisted part on higher arm, extra material beyond the right facet
10	20.1 dB	perfect
11	19.7 dB	perfect
12	20.3 dB	perfect
13	20.2 dB	perfect
14	19.8 dB	2 twisted parts, each on higher and lower arm, 1 black dot on the left
15	19.5 dB	2 twisted parts, each on higher and lower arm, 1slit on the left, 1 twisted part on the right
16	20.1 dB	1 small black dot on the left Y junction, 1 twisted part on higher arm, 2 twisted parts and 1 small black dot on lower arm, 1 gap 1um on the right

Table 3.1 Measurements and inspection records of MZIs on DIE6 and DIE21-6

L=3.8mm, center waveguide separation=240um		
1	25.7 dB	perfect
2	24.2 dB	2 twisted parts, each on higher and lower arm
3	21.7 dB	2 gaps 3um wide, each on higher and lower arm
4	25.2 dB	1 small bite and 1 long scratch on the higher arm
5	28.1 dB	perfect
6	21.3 dB	perfect
7	31.2 dB	1 bite on the edge on higher arm, 1 slit on lower arm
8	19.2 dB	1 small scratch on the right Y junction, 1 deep scratch near the right end

Table 3.2 Measurements and inspection records of MZIs on DIE3

Although the measured loss of the MZI could not be compared with a theoretical one, they are still listed in tables together with their inspection records as Tables 3.1 and 3.2. In both tables the first row gives the length and arm separation of the MZI, while the rest are divided into three columns. The left column gives the number of the MZI, the middle one gives its total insertion loss, and the right one the inspection results. Rows for MZIs that looked perfect in the inspection are highlighted to facilitate reading.

From these two tables we discover that the insertion loss and the inspection comments are not necessarily related. Comparing MZI No.3 and 4 in Table 3.1, or No.1, 5, and 6 in Table 3.2, we find that the MZIs had quite different insertion losses, though their inspection comments all said "perfect". Another example was the contrast of MZI No.5 and 8 in Table 3.2. No.5 was commented "perfect" while No.8 had some defects, yet the insertion loss of No.5 was unexpectedly higher than that of No.8. These two tables serve a good evidence for the existance of defects on the end-facets or deformations of the waveguides, which affect the output power but can not be detected during inspection.

(a) MZI **(b) Straight waveguide**

Figure 3.9: Mode output of MZI compared to straight waveguide

Figure 3.9 gives a typical mode output for an MZI that was tested. The pattern was usually a mode output added to a band of scattered background light, as shown in Figure 3.9(a). A clear mode of a straight waveguide with no background light is shown in Figure 3.9(b) for comparison. One cause for the heavy background light near the mode of the MZI was that the optical paths of the two arms of the MZI was not the same, therefore generating some interference which scatters out into the background. This was detected using thermo-optic method and is given in details in Appendix B.

3.6 Couplers

Couplers were excited on the input side and measured on the through and coupled ports on the output side. The two output power values obtained in dBm were transformed into mW and added together to get the total output power. The ratio of the output power of one port over the total output power was calculated thus defining the transfer coefficient for each output port and transformed into dB. From the results of one set of couplers varying in waveguide separation, two curves for the through port and the coupled port were generated, constituting the coupling plot for this set of couplers. Figure 3.10 shows the coupling plots of couplers on two chips DIE32_1 and DIE32_2.

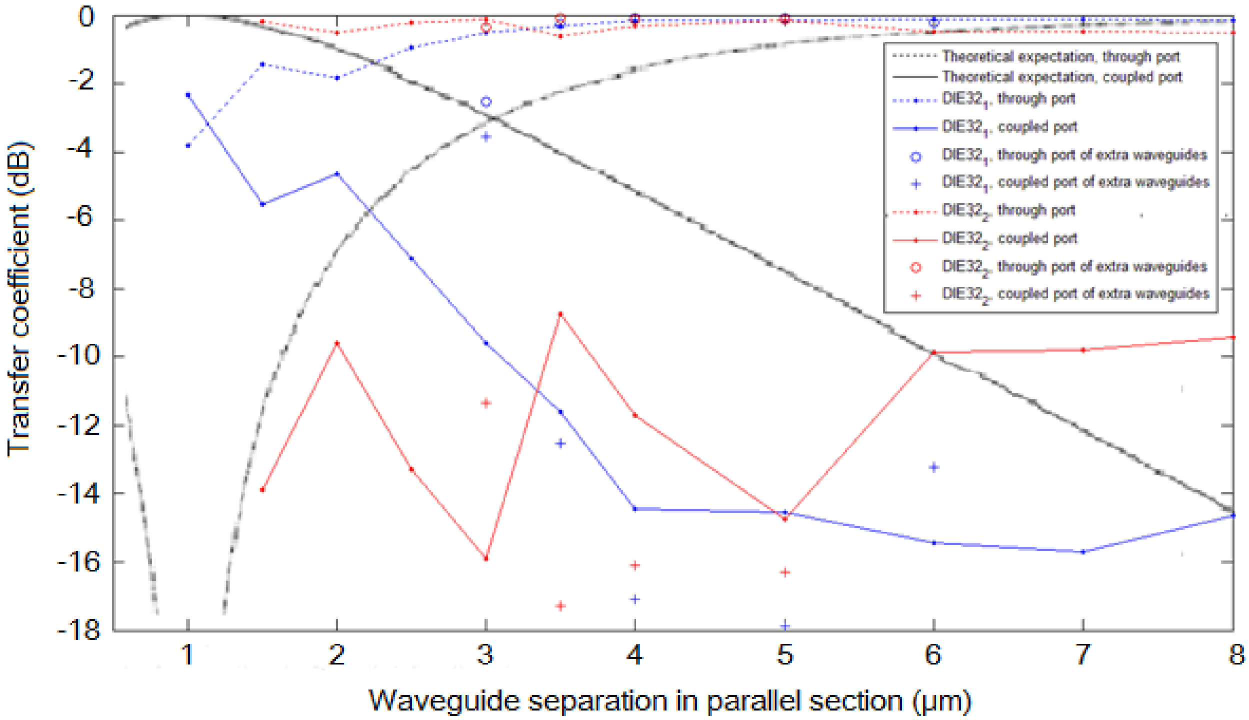

Figure 3.10 Curves of transfer coefficient versus waveguide separation

It is observed that the couplers on DIE32_1 reached 3-dB coupling (when the output power of the through port and the coupled port are equal) at a lower waveguide separation than the theoretical value of 3μm [22], which could mean that the waveguides are thicker than designed, which is not consistent with the conclusions reached for the straight waveguide, S-bend and Y-junction cases. There is another possibility, however, that the waveguide separation fabricated is wider than it is designed to be. Whether this is the case was verified by measuring the separation under a microscope. One example is shown in Figure 3.11(a). It is for the case of separation width=3μm, so the separation width should be proportionally 3/5 of the waveguide width 5μm. But measured from the picture, it is about 4/5 as wide as the waveguide, meaning that the separation is indeed wider than designed. Results for most of the other separation widths gave the same conclusion.

Noticeably, the data for 3μm separation of the extra waveguides located near 3-dB coupling is close to theoretical prediction. Nevertheless, Figure 3.11(b) shows that the separation width of this coupler to the waveguide with is also 3:4 instead of 3:5, indicating that it also has a wider separation than designed; and since the inspection record for this coupler was not good, maybe it was just a coincidence that this one agreed with the design.

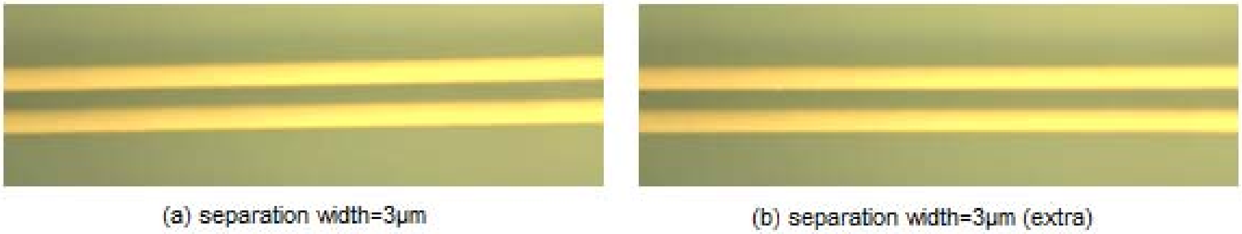
(a) separation width=3μm

(b) separation width=3μm (extra)

Figure 3.11: Microscope images of couplers with separation width of 3μm

The couplers on DIE32_2 did not couple quite well. This problem might be due to bad facets created when dicing the original DIE32 into two pieces, as was discussed in Section 2.1. Mode outputs from DIE32_1 and DIE32_2 are given in Figure 3.12(a) and (b), respectively. The corresponding waveguide separation in the parallel section for each mode was marked beside the pictures.

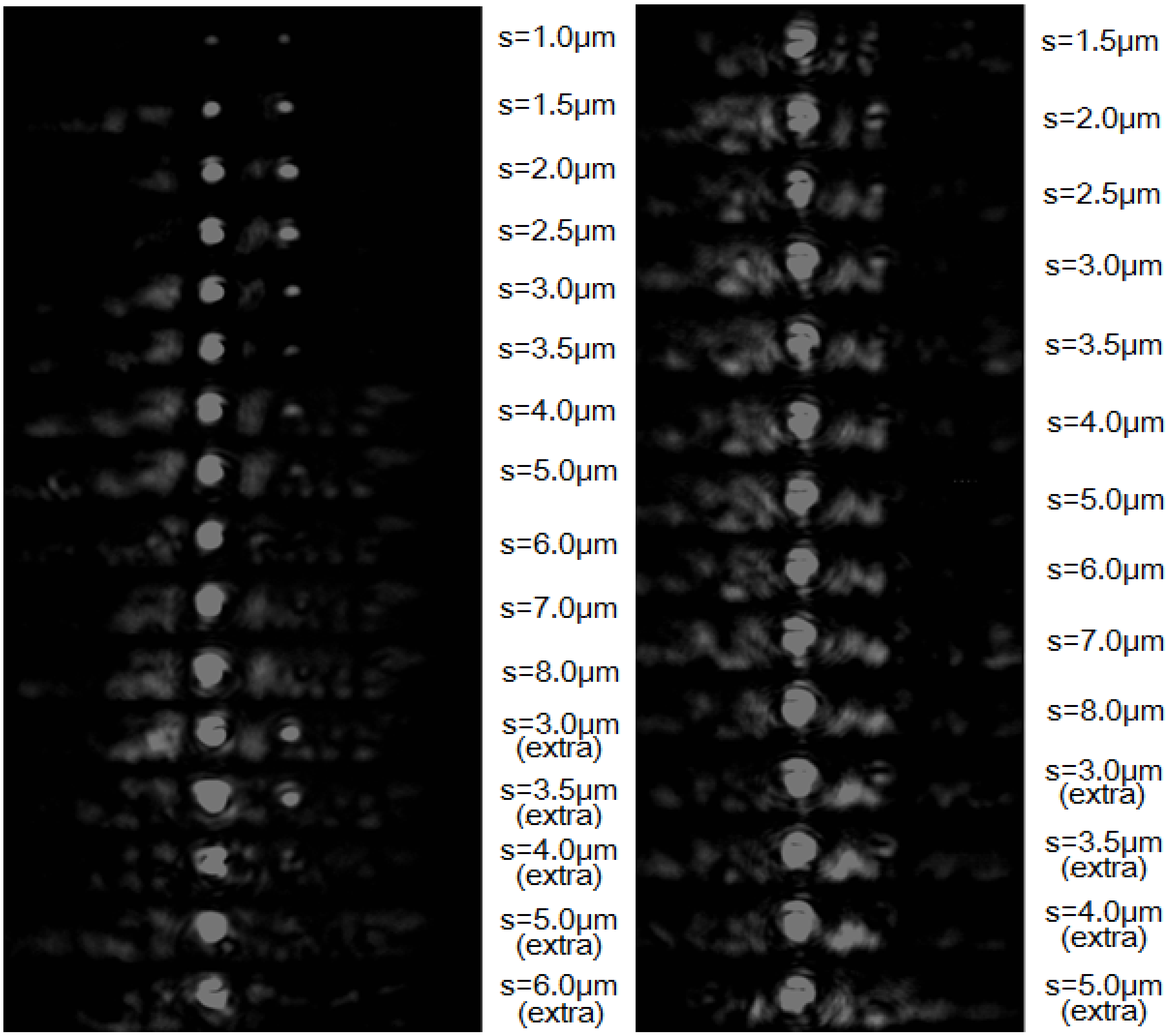

(a) DIE32_1 **(b) DIE32_2**

Figure 3.12: Mosaic of mode outputs of the couplers

3.7 Reliability of the measurements

It had been discussed in Section 3.1 that there were three possible causes for the mismatch of measured data with theoretical expectation: the design of the devices, the fabrication quality, and the measurement skill of the researcher who tests the devices. Before concluding that the problem lay in the design or the fabrication process, we must make sure that the measurement skill of the researcher did not make the problem even worse. The method used for the validation of my measurement skill was to check the repeatability of my measurements.

Group 1		
1st time (dB)	2nd time (dB)	Error (%)
19.5	19.6	0.511509
9	7.5	18.18182
12.2	11.7	4.1841
13.1	13	0.766284
16.5	17.6	6.451613
19.1	20.1	5.102041
20.2	20.7	2.444988
21	21.2	0.947867
20.6	20.2	1.960784
21.2	21.1	0.472813

Group 2		
1st time (dB)	2nd time (dB)	Error (%)
19.2	19.4	1.036269
9.7	9.1	6.382979
10.9	10	8.61244
14.8	14.5	2.047782
16.5	16.2	1.834862
19.5	19.4	0.514139
21.4	21.3	0.468384
20.7	21.1	1.913876
21.2	21.1	0.472813
21.2	22.2	4.608295

Group 3		
1st time (dB)	2nd time (dB)	Error (%)
19.1	19.1	0
10.1	9.8	3.015075
Bad	Bad	N.A.
13.3	13.6	2.230483
17.7	17.9	1.123596
18.7	18.8	0.533333
19.2	19.3	0.519481
20	20	0
20.7	19.6	5.459057
21.4	22.1	3.218391

Average error(%)
2.931554

Table 3.3 Repeatability of measurements

Table 3.3 gives the repeatability of 3 groups of insertion losses. Each loss was measured twice -- in the second time the system was absolutely realigned -- and the error was calculated and listed in the table. We see that except for a few large ones most of the errors were within 5%, and the average of all these errors was 2.93%, which could be considered as acceptable.

4. Thermo-optic modulation

As introduced in Sections 1.5 and 2.1, the structure of the device tested in thermo-optic measurements is a straight waveguide connected with two contact pads, as shown in Figure 2.3. Metal probes are dropped to the pads and an electric current is injected through, heats the waveguide and induces a temperature gradient in the nearby CYTOP claddings. A negative gradient of refractive index is formed in the cladding region near the stripe due to the negative TOC of CYTOP, which, if is large enough, induces cut off of the LRSPP, causing leakage of optical power into the cladding mode. Thus finding the threshold for thermo-optic cutoff is important.

Another concern is electromigration -- too large an injected current density will burn the waveguide. In order to prevent electromigration we need to obtain the threshold current density through a few burn-out experiments; they are conducted first.

4.1 Electromigration threshold

4.1.1 Short term experiments

Figure 4.1(a) shows the resistance-versus-time curve of two waveguides on a DIE32. The tested waveguides are couplers 1.5 mm long in the direction of the width of the chip, fabricated with 2 designed gaps about 5μm wide and 2 pads fabricated on them. In these experiments we applied a controlled voltage to those waveguides by metal probes, measured the current passing through, and calculated the corresponding resistance value for each pair of voltage and current values. The applied voltage was increased step by step -- each step was 0.1V, lasted 10s -- from 8V until the waveguide was burnt out. Here 10s was set to be the duration of one step so that the trend of changes in resistance could be seen clearly while the experiments would not last too long. Since the voltage steps were very low and much shorter than the total time of the experiments, they could be regarded as data points of resistance versus voltage as well (each voltage value corresponds with 10 resistance values), forming two voltage-resistance curves ranging from 8V to about 22.5V or 22.1V respectively, as shown in Figure 4.1(b). In both (a) and (b) the two curves generally had the same trend: from 0s (8V) to about 500s (13V), the resistance increased with the voltage linearly as expected based on the temperature variation of resistivity; after passing 500s (13V) they began to deviate from the linear relation by first decreasing and then increasing at about 800s (16V); and finally burnt out at about 1500s (above 23V). The two curves also had the same characteristics for the individual steps, as shown in Figure 4.1(a). At the beginning, the resistance remained the same value within one step, in which the voltage was kept constant. As the general trend of the curve started to deviate from linearity, the resistance went down though the voltage was still constant during one voltage step. From 500s (13V) to 800s (16V), the decrease within each step was even larger than the increase occurring when the step began, so the general trend of resistance deceased in this section. On the other hand, the resistance within each voltage step went up after the experiment lasted 1200s (20V), until eventually rose to infinity when burnt out.

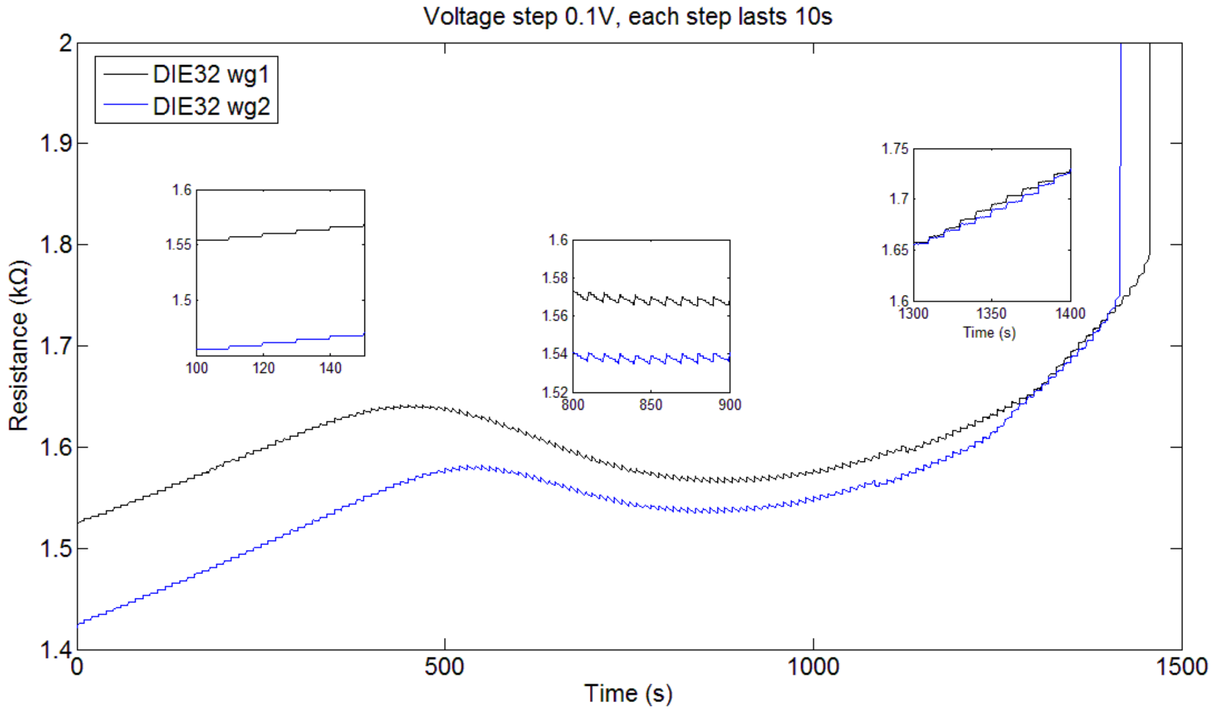

(a) Resistance versus time

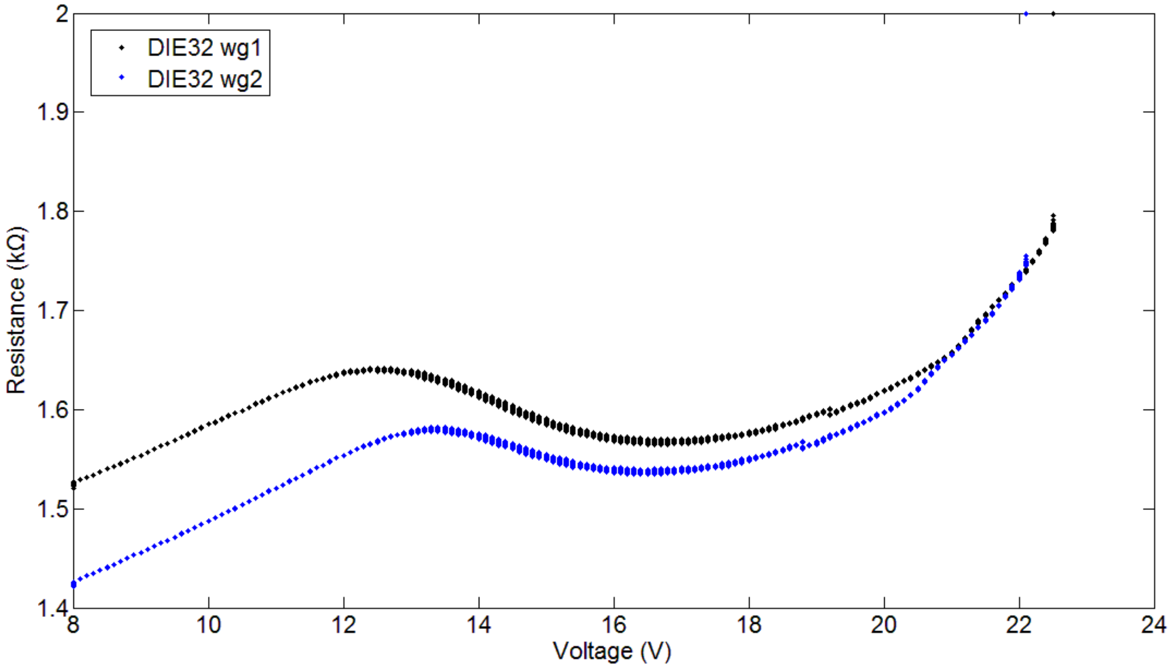

(b) Resistance versus voltage

Figure 4.1: Short term experiments. Each voltage step was 0.1V high, lasted 10s. Voltage ranged from 8V till about 22V (burn-out).

From Figure 4.1 we discover that the waveguides burnt at around 1400s~1500s, corresponding to a voltage value of about 22V, but even before this voltage value was reached, some permanent changes had already occurred and the resistance-voltage relationship deviated from linearity. To exclude most of the electromigration effect, it is necessary to choose a much smaller threshold value than the burn-out limit. A value chosen near the end the linear section might be better. Henceforth we use an operational definition for the term "electromigration threshold" that it is defined as the current density from which the voltage-resistance relation begins to deviate from linearity. We choose the current density associated with t=360s, V=11.5V to be the threshold and it is necessary to test how well the waveguides could work under this voltage value in the next experiment.

4.1.2 Long term experiments, V=11.5V

Figure 4.2 represents a resistance-versus-time curve measured under a constant voltage of 11.5V for a relatively longer period. It was observed that in the first 1200s the resistance fluctuated within 0.01kΩ, whereas in the next 2400s it remained generally stable, at around 0.95kΩ. The waveguide was burnt out after about 1 hour, as its resistance suddenly increased to infinity. From this experiment it was proven that even working at small voltage values the waveguide could still burn out if it worked long enough, as was discussed in Section 1.5. It was also determined that this waveguide can work normally for 1 hour under the voltage of 11.5V. Thus when using the same kind of waveguide for thermo-optic modulation under a constant or a changing voltage of 11.5V or less, we expect its total lifetime to be at least 1 hour.

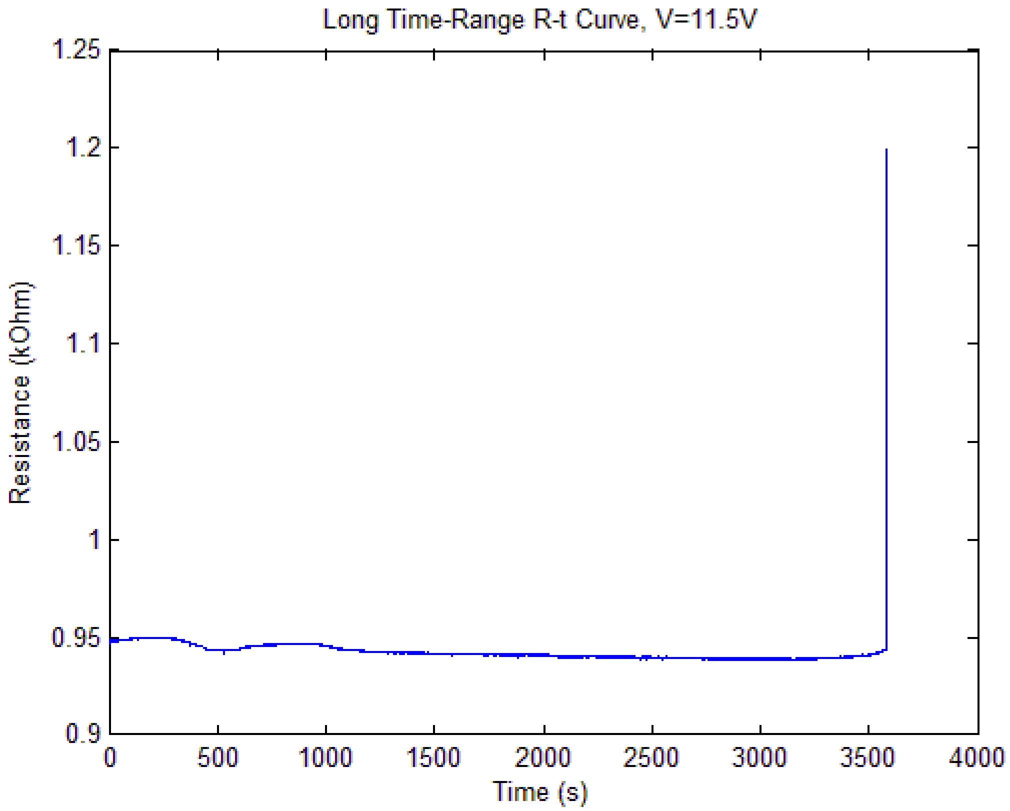

Figure 4.2: Long term experiments, V=11.5V

4.1.3 Long term experiments, V=6V

It could be interesting to see how the waveguide would work under even lower voltage, which was supposed to show smaller changes or fluctuations and longer lifetime. The result of 4 consecutive resistance-versus-time measurements carried out on the same waveguide is illustrated in Figure 4.3. In all these experiments the applied voltage stayed at 6V. The metal probes injecting the electric current were not readjusted between two consecutive experiments but were left untouched. The data points shown in this picture were plotted by smoothing.

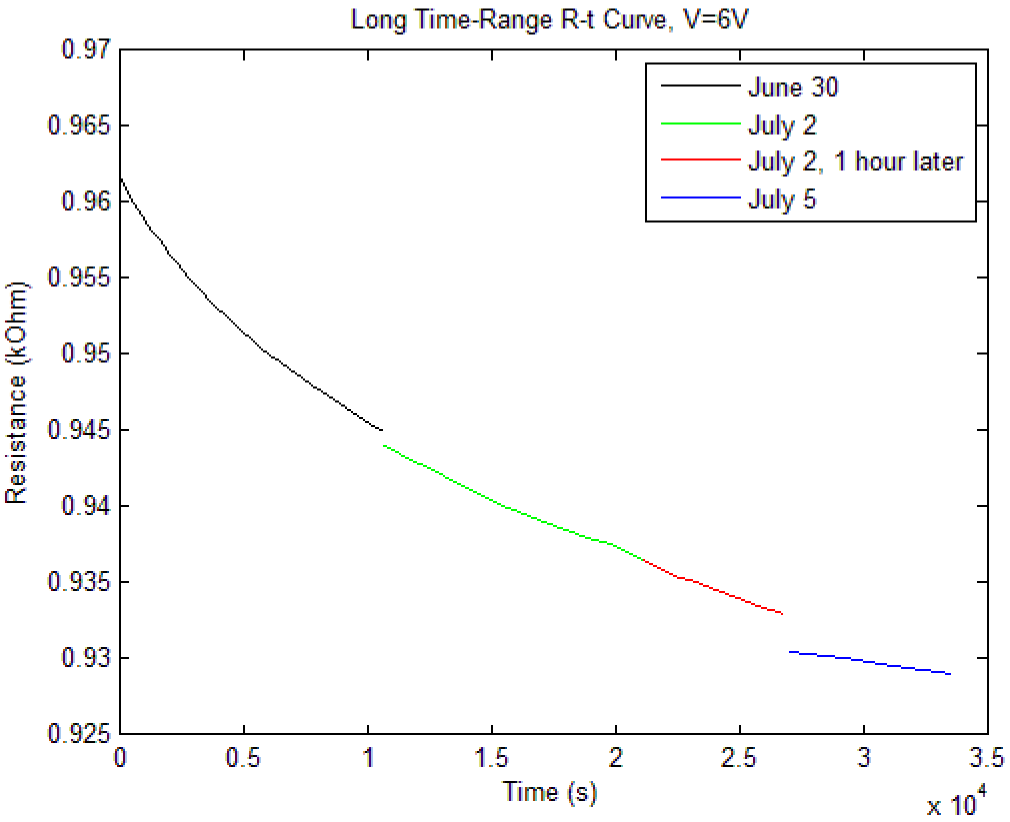

Figure 4.3: Long term experiments, V=6V

We notice that the resistance of the waveguide gradually decreased as time went by. One possible cause of this slight decrease could be the drifting of the attached probes causing changes in the contact resistance. For analyzing it, a comparison amongst the 4 curves in Figure 4.3 was needed. The second curve was drawn 2 days later than the first one, and there was a small gap between them -- the starting point of the second curve was 0.001kΩ lower than the first one. Similarly, the fourth curve was taken 3 days after the third one, in between which there was a relatively larger gap than the former one. Yet the second and the third curves were drawn in the same day with only 1 hour between them, correspondingly, these two curves were almost continuous, with no obvious gap between them. This comparison of gaps showed that it was the drifting of the probes occurred during the time intervals that led to those gaps, and thus could be at least a partial cause to the dropping of resistance during the experiments as well. However, as comparing the duration of the first and the second experiments, which were both 3 hours approximately, with the time interval between them, which was 2 days -- 48 hours, we could realize that the gap formed during this interval should have been much larger than what is shown in the plot, or in other words, the decrease in resistance in these curves should have been much smaller than the gap, supposing that drifting of the probes was the only cause of the decreasing resistance. Since it was actually not that small, the extra decrease must be due to other causes, for instance, the changing internal structure of the waveguide.

Finally, we should notice that whatever the causes might be, the total decrease of approximately 0.03kΩ over about 10 hours, was rather small, showing that the resistance was stable enough for the waveguide to work normally.

To sum up, V=11.5V was chosen as the safety threshold value in order to prevent electromigration. The current and current density associated with this voltage value is about 12.2mA and 70GA/m^2 respectively. This result is reasonable compared to 66.6GA/m^2 for the current density value reported in reference [11], which used the same operational definition for the electromigration threshold. Waveguides on DIE32 could work under this voltage for 1 hour, a lifetime long enough for the thermo-optic experiments; and under smaller voltage its lifetime would be longer. There would be reducing of waveguide resistance brought about by both drifting of the probes and structural changes of the metal of the waveguides, but the decrease was small enough to be neglected.

4.2 Mode extinction threshold for straight waveguides

4.2.1 Curves of optical-power-versus-current, set 1

As mentioned in Section 1.5, when the electric current injected into the metal stripe increases, the heat generated herein forms a temperature gradient in the nearby CYTOP cladding region. Because CYTOP has a negative TOC, the central region nearest the metal stripe would have a lower refractive index, forming an anti-guide exerting an effect on the propagation of the LRSPP mode. When the injected current density reached a certain value, the effect brought about by the anti-guide was so strong that the LRSPP mode would be cut off (and radiate into the background cladding). It was necessary that we determined this threshold value for mode extinction of the straight waveguide case.

To obtain this threshold value, the applied voltage was increased by steps of 0.1V every 0.5s so the injected current increased correspondingly, and the optical power for each current value was measured. In this method an optical-power-versus-current curve could be drawn. When a decrease of optical power was observed on this curve, the current would be the mode extinction threshold. The waveguides tested in this experiment are all 4.8mm-long straight waveguides with metal pads.

Figure 4.4 shows one set of this kind of measurement consisting of 18 optical-power-versus-time curves taken consecutively within one day, on the same waveguide (Waveguide 5 on DIE2_4). After each measurement, the alignment of the fibers and waveguides would always be readjusted whereas the metal probes were left untouched, and I always waited for about 15~20 min until the optical power was restored and remain stable (in order to dissipate the heat generated in the last experiment) before starting the next experiment.

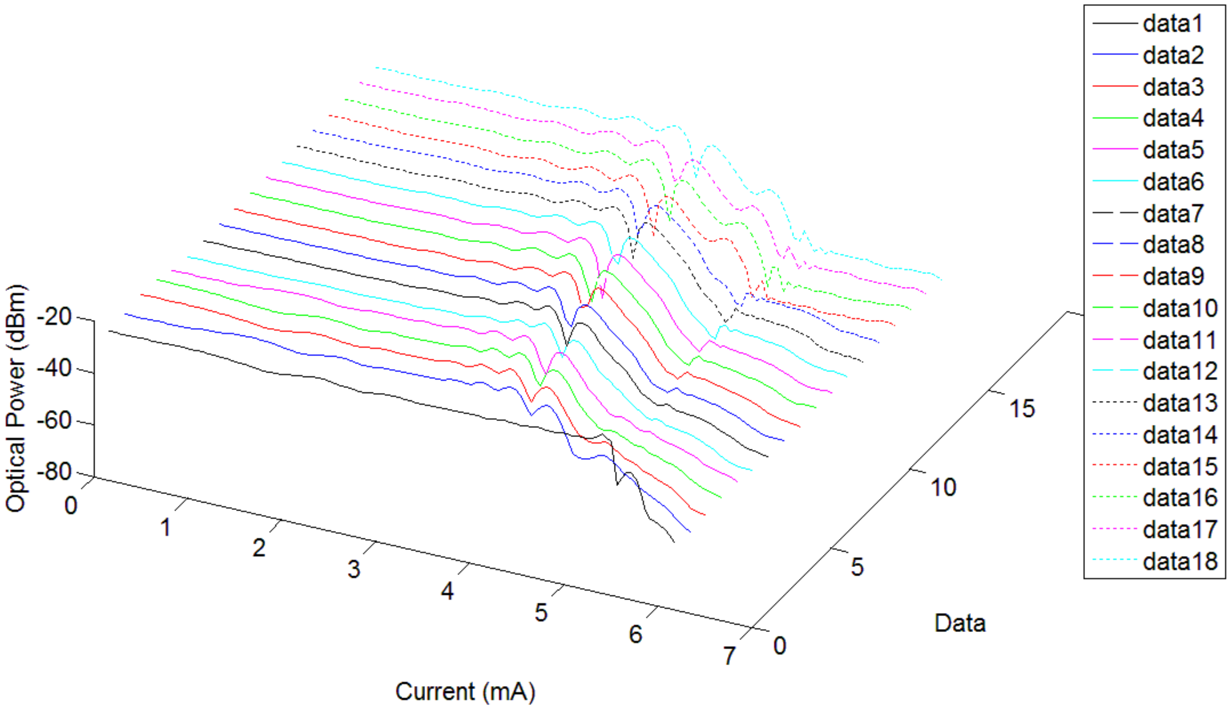

(a) Waterfall plot

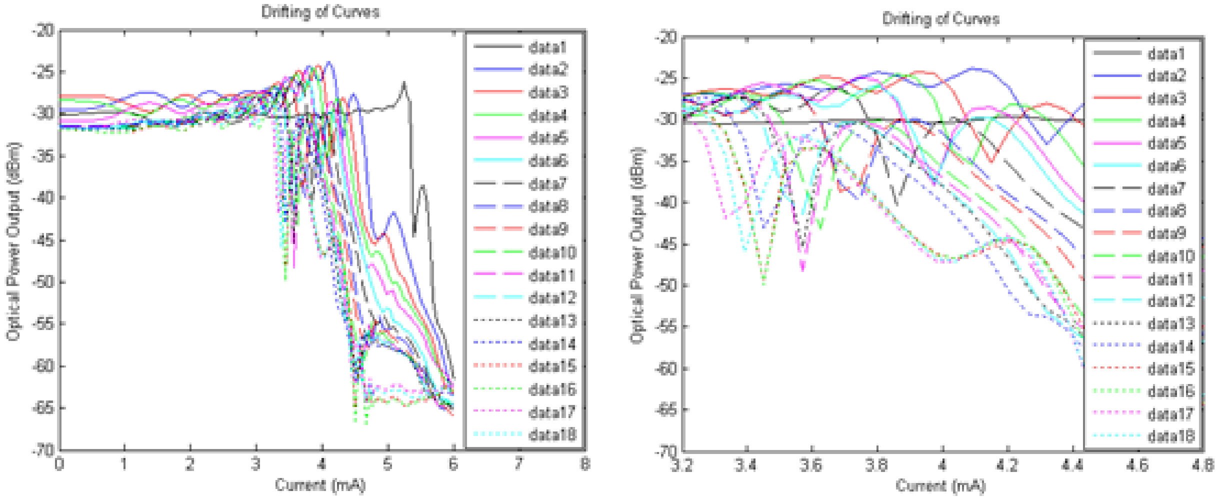

(b) Planar plot **(c) Zoom-in plot**

Figure 4.4: Curves of optical-power-versus-current, set 1

Figure 4.4(a) illustrates the 18 measurements as a waterfall plot, showing that except for the first curve, they had the same trend. At lower current the optical power was generally stable when the current increased, with a few small fluctuations caused by the beating between the LRSPP mode and the cladding mode. As the current increased to a higher value, the fluctuations in optical power grew larger and larger, ending in a peak value before dropping off. This peak was due to the decrease of the refractive index of the claddings surrounding the waveguide as it was heated, making the mode field enlarged and the attenuation decreased. After that it reduced sharply to the first valley, then went up again to a second bump, and finally dropped all the way down to very small values near 0mW. It is also be discovered that there was a general trend of “moving leftward” for these curves as the experiment was run time after time; this is shown more clearly in planar plot in Figure 4.4(b), although there are some exceptions as sometimes the curve stayed put or moved rightward. This trend was more detailed when focusing on observing the current values for the first peak, first valley and second bump, which all generally decreased as given in expanded view in Figure 4.4(c). The first curve, however, was an obvious exception, standing far away from the other curves and having a much higher current value for the first peak.

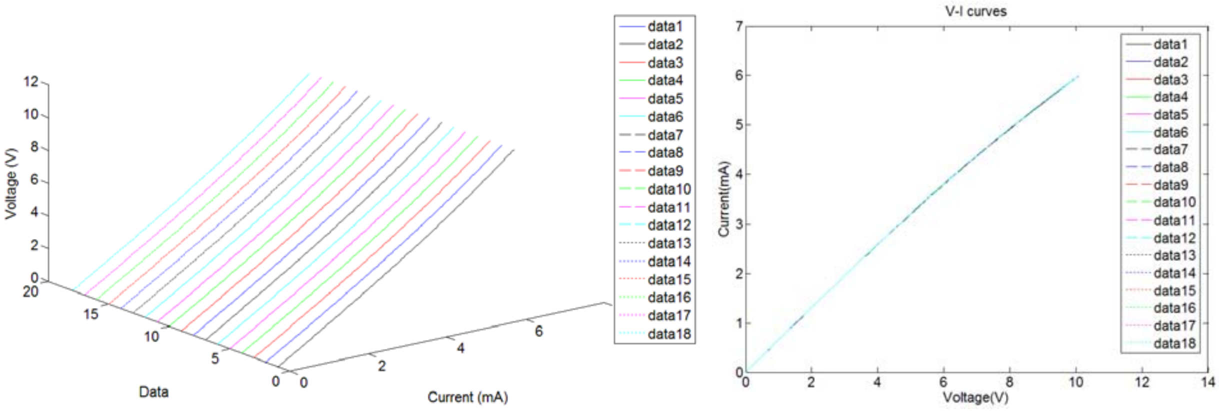

(a) Waterfall plot **(b) Planar plot**

Figure 4.5: Curves of voltage-versus-current

I wondered whether this “drifting to the left” behaviour of these curves was accompanied by any changes in electric properties of the waveguide so I plot a set of voltage-versus-current curves in

Figure 4.5 for observing the resistance. The relationship between each voltages sweep and its currents is linear in all cases, indicating that the resistance value within one experiment was constant, as shown in Figure 4.5(a). The 18 voltage-versus-current curves all overlapped with each other, indicating that the resistance value from time to time remained constant, as shown in Figure 4.5(b). Thus we know that the electric properties of the waveguide did not have obvious changes, only their optical properties changed.

One possible cause for drifting is the time that I waited after each measurement (15~20min) may not be long enough for the generated heat to dissipate thoroughly (CYTOP has a rather small thermal conductivity as mentioned in Section 2.4), thus heat accumulated after a previous experiment would affect the latter ones. Since we already had some heat accumulated there, less heat would be needed to reach the cut-off state, so the measured threshold current value would became smaller and the curve would move leftwards. To investigate this possibility I started another set of experiments on the same waveguide on the next day, which was at least 10 hours later and could be regarded ample for the device to cool down.

4.2.2 Curves of optical-power-versus-current, set 2

Figure 4.6 represents 12 optical-power-versus-current curves taken on the same waveguide in a similar method on the next day, and they had the same trend as the first 18 curves showed us. The first curve was far from the rest ones and looked quite different. The other curves all had a first peak, a first valley, and a second bump, and the general trend of these curves was drifting leftwards, in other words, the current values for the above three characteristic points became smaller as the experiment was run time and time again. One apparent exception was data 4, which moved far rightwards into a location nearly in the middle of the first curve and the rest ones. This might be because that it was taken at least 2 hours more or less rather than 15~20min after data 3, so the heat accumulated during the first 3 experiments could have been dissipated.

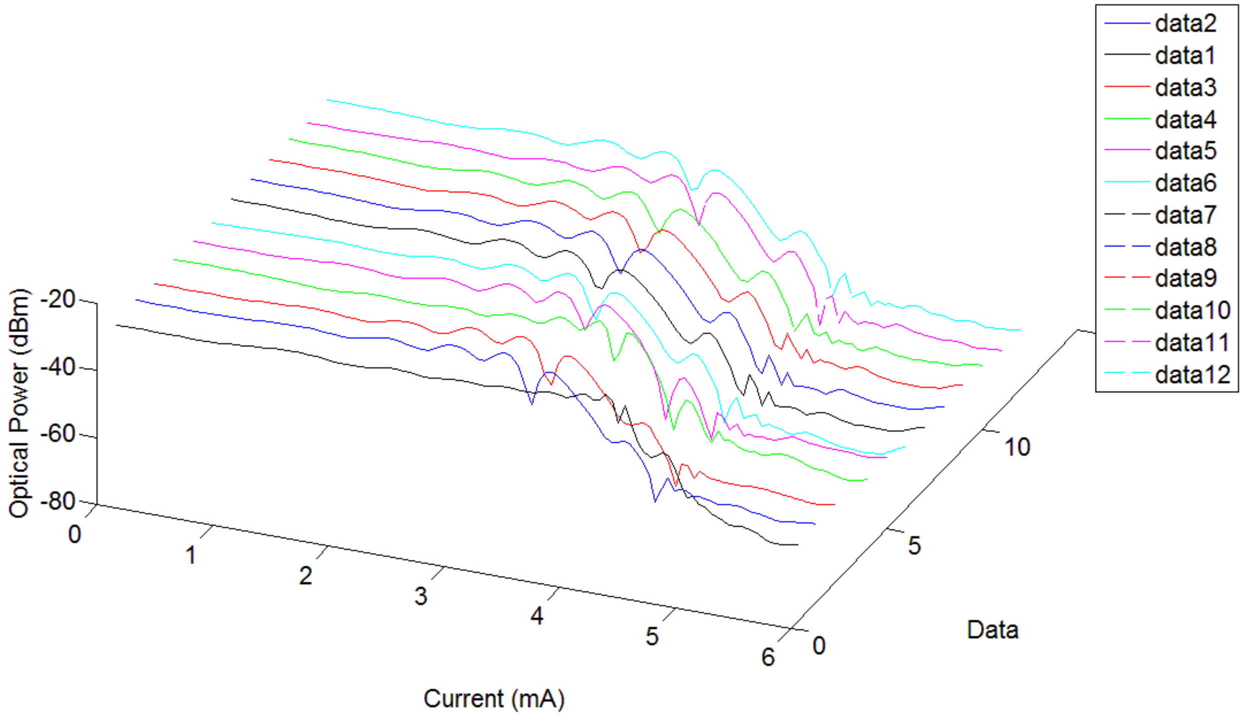

Figure 4.6 Curves of optical-power-versus-current, set 2

The drifting could be observed more clearly if we plot the two sets of measurements together, as is shown in Figure 4.7. The 30 curves were divided into 3 groups differentiated by colors. Each group was taken consecutively with time intervals of around 15~20min. It could be demonstrated that within every single group the first peak, first valley, and second bump became smaller and the curve drifted leftwards time and time again. Once waiting long enough for the device to cool down, the next curve would always turn back but then the following ones would resume the previous leftward trend. Even those curves that turned back would not return to the original location, for instance, comparing the first curves of each group data1, data19, and data 22 we discovered that although data 19 did move backward it did not return as far as data 1, and data 22 returned even less than data 19.

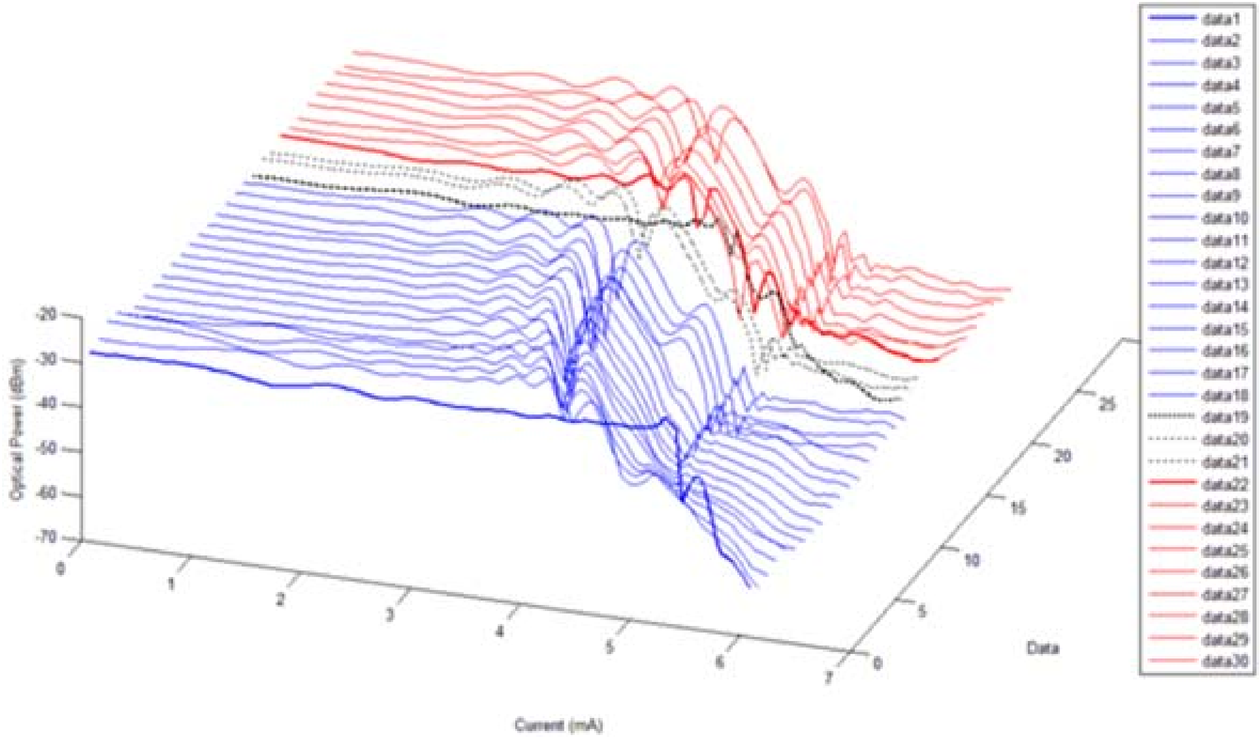

Figure 4.7 Curves of optical-power-versus-current, set 1 and 2 together

Two conclusions can be drawn. First, the accumulation of heat during a previous experiment is one cause for the drifting of the curves. Second, it was not the only cause of the drifting, for even given ample time for heat dissipation the curve would not return to its original place, indicating that some permanent changes must have occurred to the waveguide.

A cause that might explain the permanent change was that the CYTOP cladding around the waveguide could have experienced glass transition due to the high temperature of the waveguide. Some documents mentioned that CYTOP would transit from glassy to rubbery at 108˚C (glass transition temperature) [24]. An estimation of the temperature of the metal waveguide can be made based on the following equation [11],

$$R(T) = R(T_0)[1 + \delta(T - T_0)] \tag{4.1}$$

$R(T)$, $R(T_0)$, δ, and T_0 are the resistance at temperature T recorded as 1.681 kΩ, the resistance at room temperature which is 1.504 kΩ, temperature coefficient of resistivity of gold taken as 1.3876×10^{-3} (˚C^{-1}) [11], and room temperature which was 25˚C, respectively. The estimated waveguide temperature was approximately 109.8˚C, exceeding slightly the glass transition temperature of CYTOP. This meant that the CYTOP near the metal stripe could have transited to rubbery and back again upon cooling, causing a permanent change to the metal stripe and thus the waveguide.

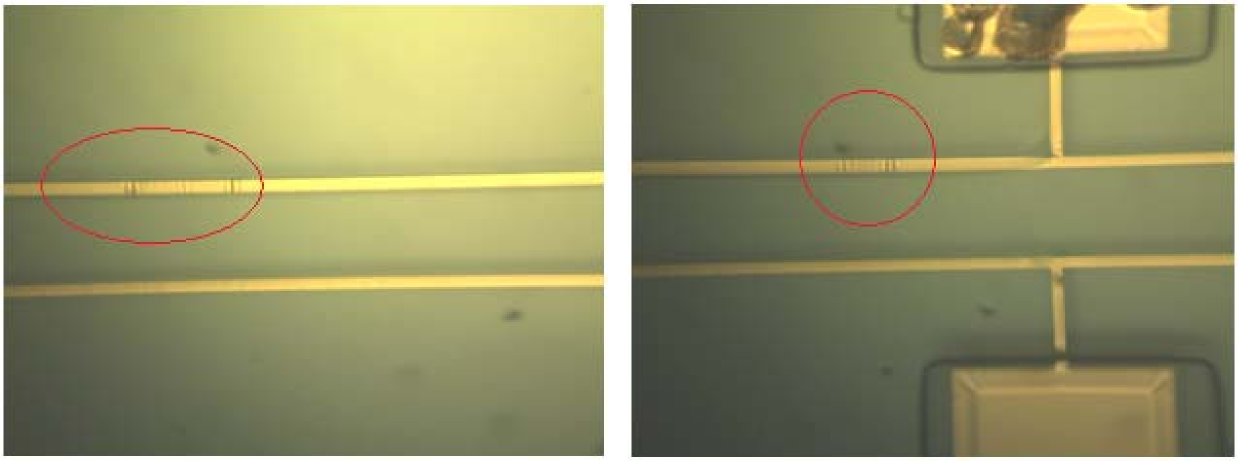

Figure 4.8: Microscope images of permanent changes along waveguides

Figure 4.8 gives microscope images of some of the permanent changes newly observed after the experiments. Comparing the upper waveguide which had been tested many times and the lower one that was not tested, it is discovered that some rugged sections that were not recorded in the inspection appears on the tested waveguide, as marked in red circles. Another change observed but not included in the pictures is that the path for the electric current on the waveguide looked brighter and wider, probably due to changes occurred in its nearby CYTOP claddings.

Besides, the restoration of optical output seemed to occur faster in the last few measurements, in which it usually took about 10min for the optical power output to restore stability after cutting off the current, comparing to 15~20min for the first few measurements. This probably indicated permanent changes on the chips as well.

4.2.3 Adding TEC to the setup

In an attempt to exclude the effect of heat accumulation I added a TEC to the setup so that the temperature of the TEC and the Si substrate could be detected and controlled. Figure 4.9 represents the results of 12 measurements carried out similarly as discussed in 4.2.1 and 4.2.2, on another single straight waveguide (Waveguide 17) on DIE2_4.

The same trend of drifting of curves as Figure 4.4 and 4.6 could be found in Figure 4.9(a). From Figure 4.9(b) it could be discovered that this set of curves was more regular than the previous two sets. Time after time the first peak decreased a little, the first valley grew deeper making the second bump more and more distinct, there also seemed to be a disappearing third bump and an emerging fourth bump, of which the trend looked systematic. The mechanism of this trend is yet to be further explored.

We could see through the prominent drifting of curves in Figure 4.9 that the TEC did not solve the problem. Two possible reasons might explain the lack of success. One was that it was glass transition of the CYTOP rather than the accumulation of heat that was the main cause of the drifting problem. Another possibility was that the heat accumulation problem was not absolutely resolved and so still served as a cause for the drifting.

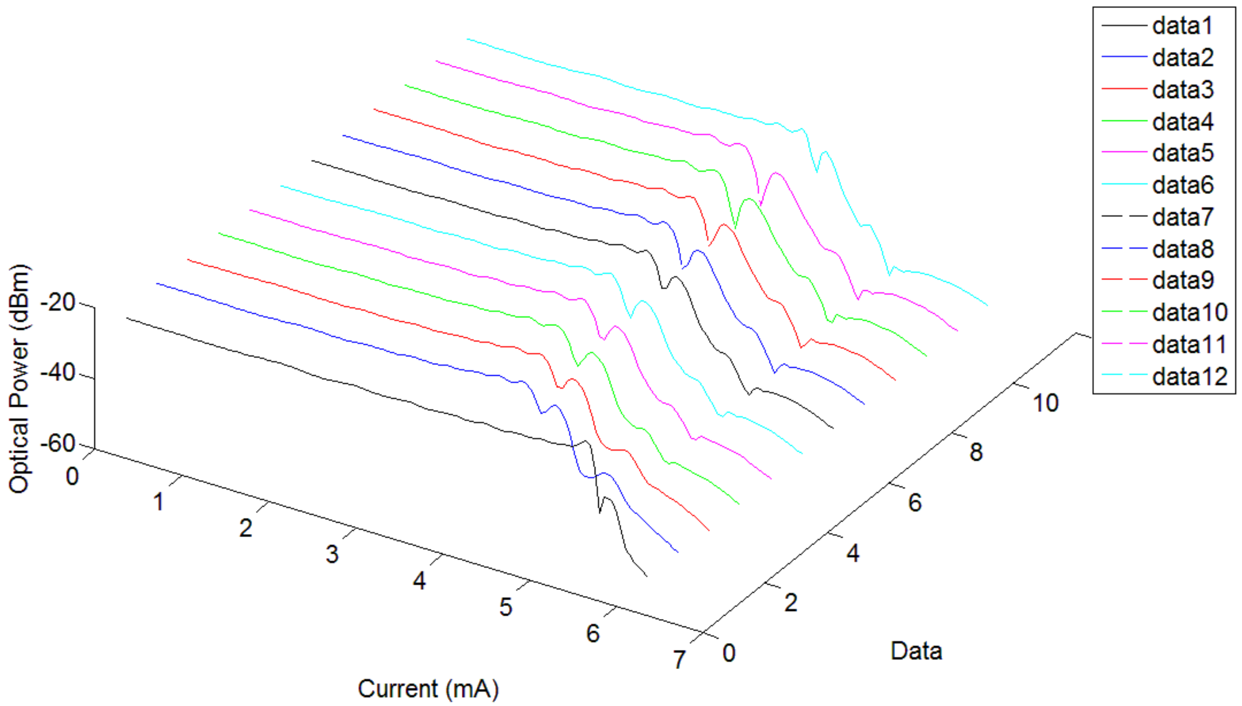

(a) Waterfall plot

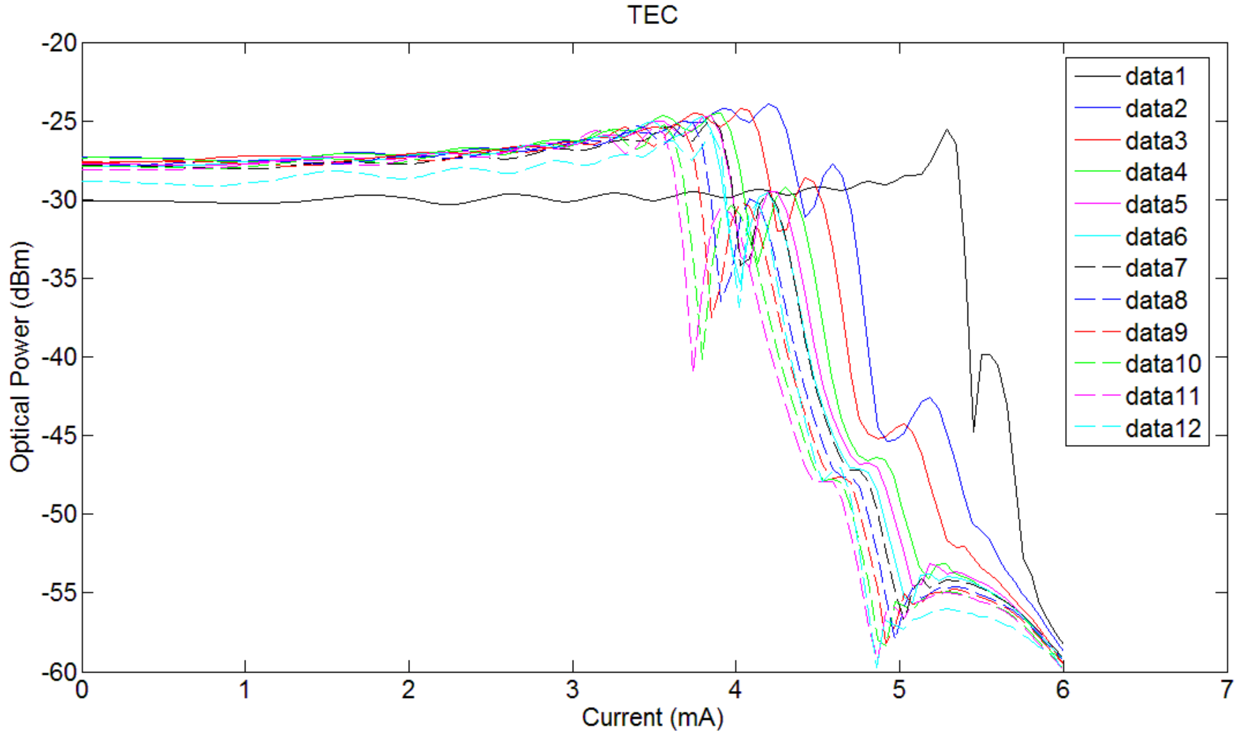

(b) Planar plot

Figure 4.9 Curves of optical-power-versus-current, after adding TEC

Although the current value for the first peak went smaller time after time, a current of about 2.5mA could be considered safe enough for waveguides on DIE2_4 for the first dozen of experiments, based on the results of Figure 4.7 and 4.9. This value is chosen because below this value no cutoff occurred, as well as the optical power output remained generally constant as the current changes. In the future works phase modulation on a MZI will be carried out beneath this current value so that the modulated arm will not be blocked due to the cutoff of the LRSPP mode travelling through it, and the changes of the optical power output of the MZI caused by the phase change on the modulated arm will not be affected by the change of optical power in this arm.

4.2.4 Mode outputs and their relation with the optical-power-versus-current curve

Figure 4.10 shows one set of mode outputs under different voltage and current values, helping to explain the changing optical output power with the injected current.

From 0mA to 2.46mA the mode did not change a lot, corresponding with the generally stable section in an optical-power-versus-current curve. Beginning at 2.46mA the mode grew brighter, and from 2.94mA the background light appeared and increased. The first peak was reached at 3.2mA, after which the mode went dimmer and the background light became even stronger. The mode nearly disappeared but then appeared again at about 3.66mA, corresponding to the second bump shown on the optical-power-versus-current curve. After that, both the mode and the background light gradually got dimmer, and a third bump seemed to be reached at about 4.22mA. The mode eventually disappeared altogether as we further increased the current.

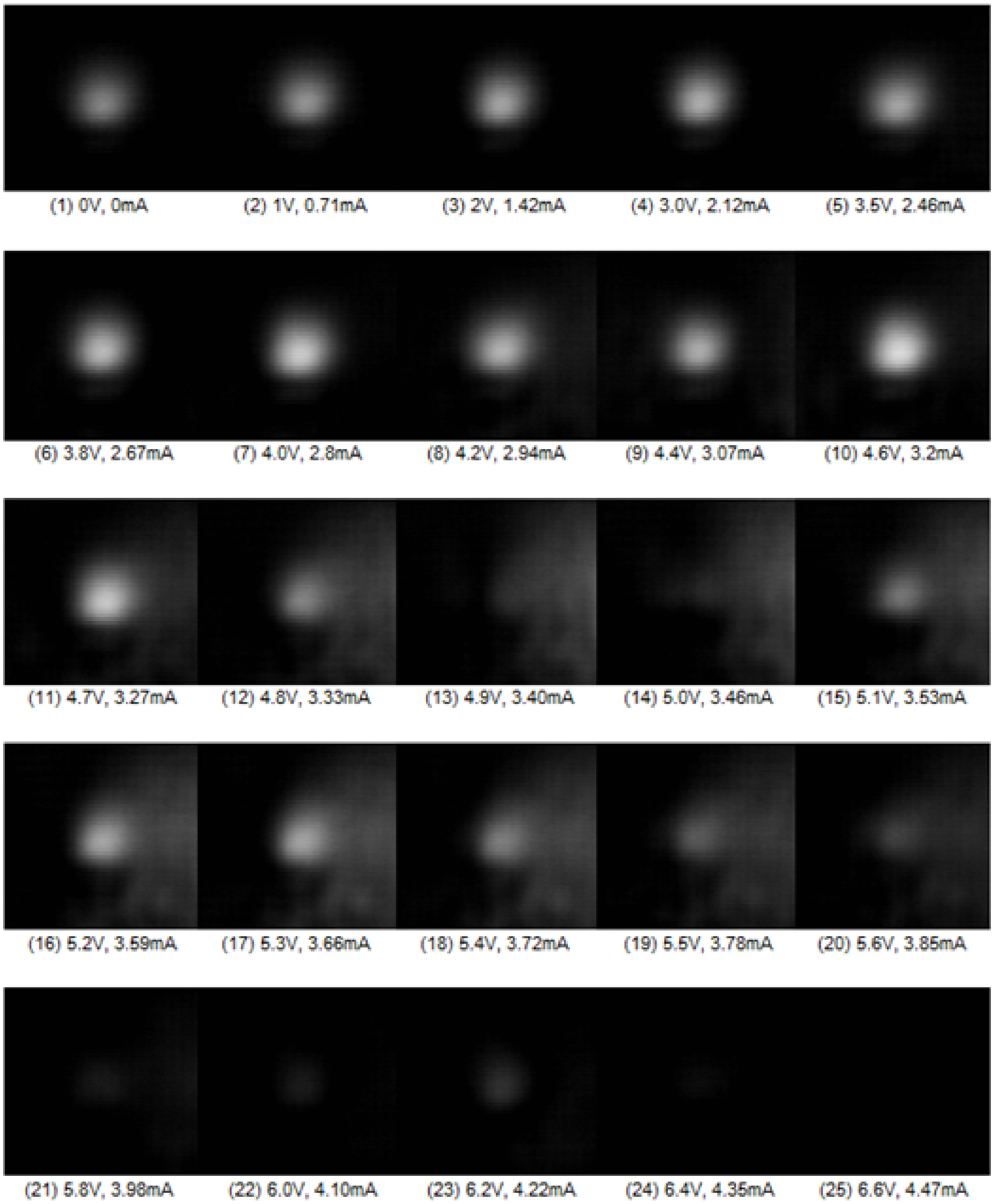

(1) 0V, 0mA (2) 1V, 0.71mA (3) 2V, 1.42mA (4) 3.0V, 2.12mA (5) 3.5V, 2.46mA

(6) 3.8V, 2.67mA (7) 4.0V, 2.8mA (8) 4.2V, 2.94mA (9) 4.4V, 3.07mA (10) 4.6V, 3.2mA

(11) 4.7V, 3.27mA (12) 4.8V, 3.33mA (13) 4.9V, 3.40mA (14) 5.0V, 3.46mA (15) 5.1V, 3.53mA

(16) 5.2V, 3.59mA (17) 5.3V, 3.66mA (18) 5.4V, 3.72mA (19) 5.5V, 3.78mA (20) 5.6V, 3.85mA

(21) 5.8V, 3.98mA (22) 6.0V, 4.10mA (23) 6.2V, 4.22mA (24) 6.4V, 4.35mA (25) 6.6V, 4.47mA

Figure 4.10: Mosaic of mode outputs for different voltages and currents

4.3 Restoration after one experiment

4.3.1 Observation of temperature restoration

Using the TEC, the temperature restoration after one experiment could be recorded by turning off the temperature controller and observing the temperature detected by the sensor. It was recorded that the temperature of the TEC at the end of one experiment was 26.0˚C. Once removing the current it dropped to 25.1˚C within 10s, and further decreased to 24.9˚C in 2~3min, then fluctuated between 24.9˚C and 24.6˚C lasting 10~15min, finally got stabilized at around 24.6˚C. Thus it took about 15~20min for the chip and the setup to return to room temperature. This result corresponded with the one acquired through observing the restoration of the optical power output, which had been mention above and would be further discussed in details in the following section.

4.3.2 Observation of optical power output restoration

After finishing one experiment I tried to measure the optical power versus time as soon as possible after turning off the voltage applied to the device; the results are plotted in Figure 4.11. The first or the first few peaks appeared in 10s right after the experiment might have been missed but the changes of optical power occurred later were all included in this plot.

The t=0s point was about 10s after the thermo-optic experiment was done. In this 10s there might be one or more peaks not recorded. The optical power sharply dropped to a valley when t=15s more or less. Another peak was reached at about 50s and reduced again to a second valley at 100s. Then there came another peak which was much milder than the earlier ones. The bump ranged from 2min to 10min, followed by an approximately constant section over which the optical power had stabilized. The general trend was that the peaks became lower and smoother as time went by, and in the end became constant. One should bear in mind that this waveguide had been tested many times so it needed less time to restore optical power output, only about 10min, referring to the discussion in Section 4.2. Otherwise it would need longer time, about 15~20min.

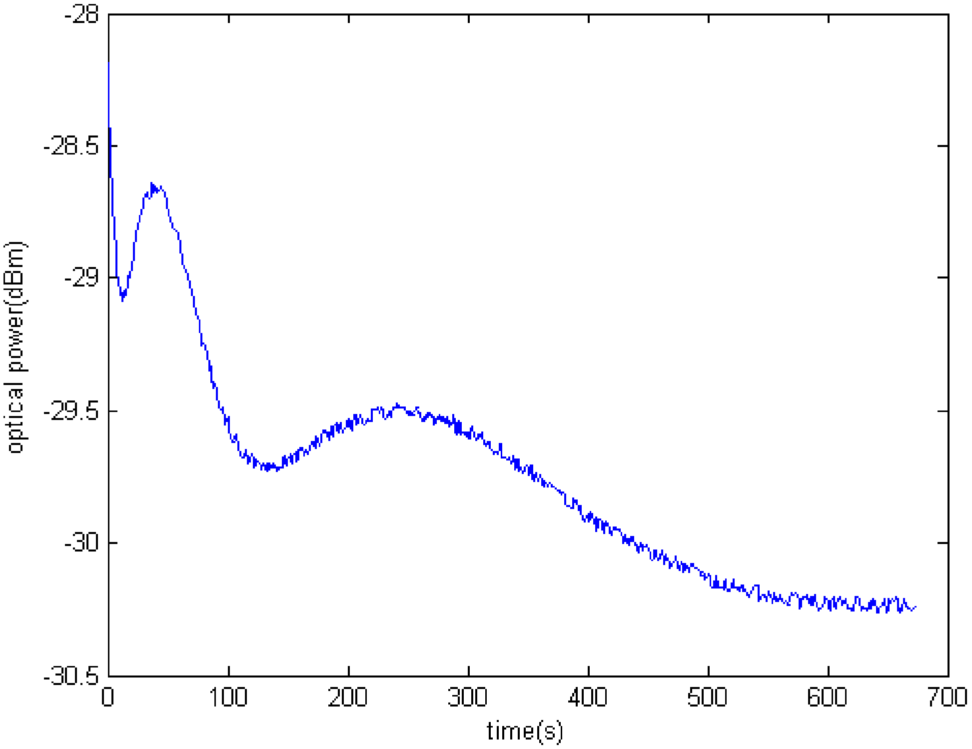

Figure 4.11: Optical power stability restoration

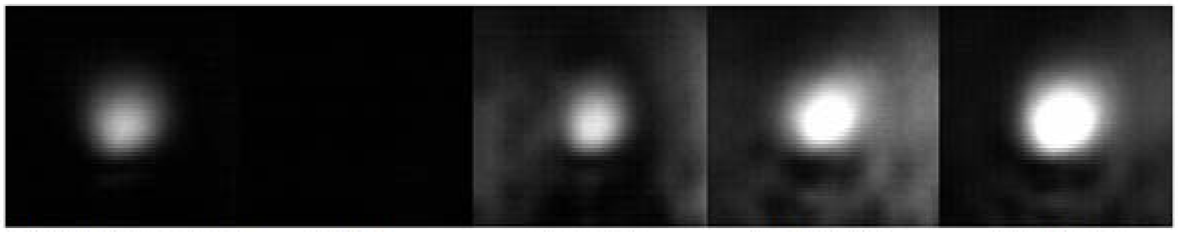

(1) before the experiment (2) cut off (3) within 10s (4) within 10s (5) within 10s

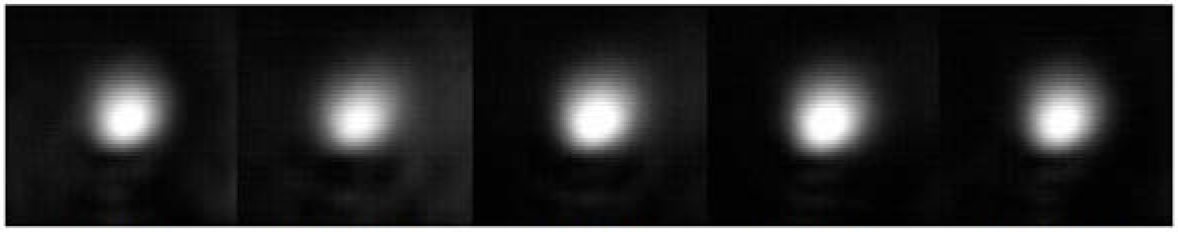

(6) 10s to 60s (7) 10s to 60s (8) 10s to 60s (9) 10s to 60s (10) 10s to 60s

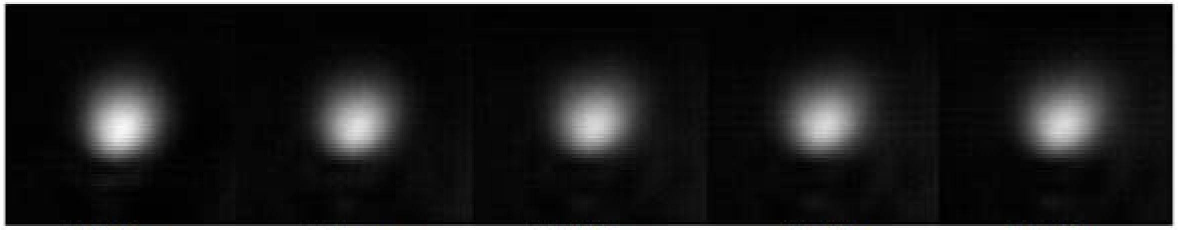

(11) 90s (12) 120s (13) 150s (14) 180s (15) 210s

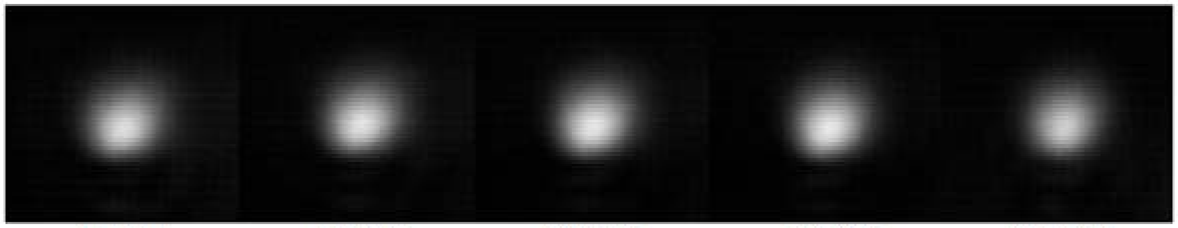

(16) 240s (17) 300s (18) 360s (19) 420s (20) >600s

Figure 4.12: Mode output restoration

Figure 4.12 shows the mode appearances during the process of optical power output restoration. Figure 4.12(1) is the mode before the thermo-optic experiment. (2) shows that the mode was cut off during the experiment. (3)~(5) were taken within 10s after the experiment was completed, in which the mode got brighter quite fast. (6)~(10) were taken from 10s to 1min, with the mode kept at a generally bright level yet fluctuating slightly and repeatedly. (11)~(20) were taken at the respective time point marked below each picture, and the mode gradually dropped to the same level as that before the thermo-optic experiment. This set of pictures could help understand the trend of optical power output versus time of Figure 4.11.

4.4 Optical response time

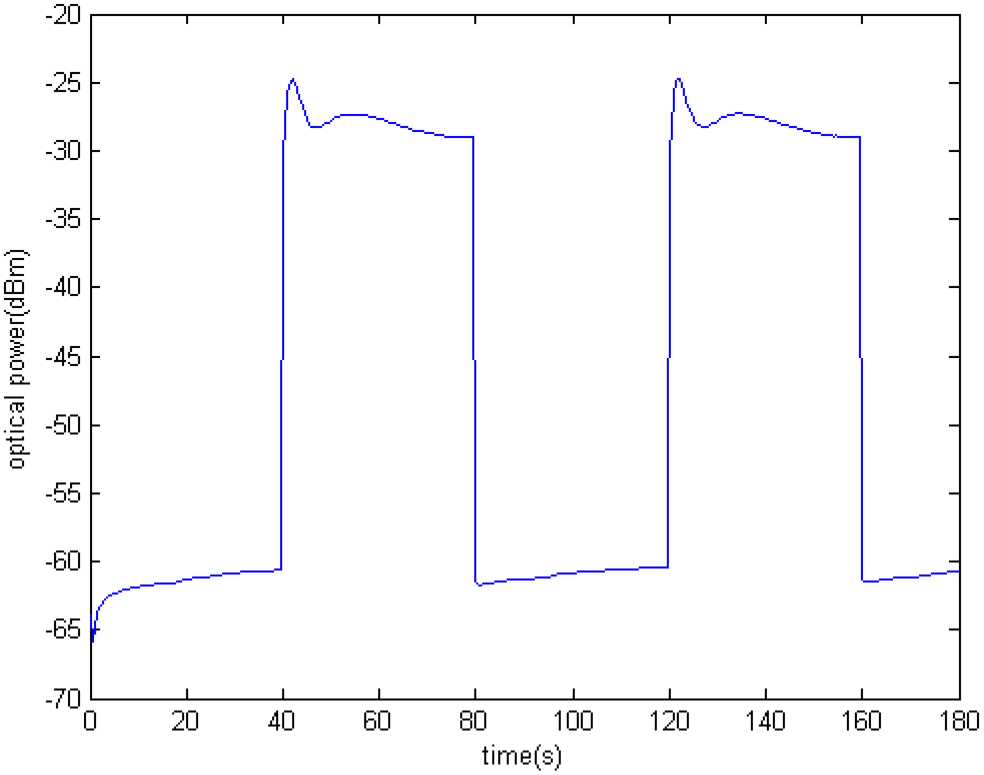

Figure 4.13: Optical response time

Figure 4.13 gives the optical rise and fall responses of the device. The optical rise response looked much the same as Figure 4.11, while the optical fall response looked normal, and reacted faster than the optical rise response. A reasonable explanation for this faster response was that the optical fall time was determined by thermal rise time, and since the optical waveguide was also the heat source, the heat generated at the waveguide did not need to diffuse very far in order to create an anti-guide and stop the propagation of LRSPP mode; whereas the optical rise time depend on thermal fall time, in other words, cool-down time, and the restoration of the mode required the heat to dissipate out of the whole optical region into the Si substrate heat sink [11]. However, both response times were quite long having the order of tens of seconds, for the low thermal conductivity CYTOP layer hindered the heat from dissipation.

5. Conclusion

5.1 Summary

Long-range surface plasmon-polariton (LRSPP) passive structures such as straight waveguides, S-bends, Y-junctions, Mach-Zehnders, and couplers, made of gold and cladded with CYTOP, designed to be 5μm wide and 35nm thick, were optically or thermo-optically tested and the results were compared with theoretical values generated from some past theoretical modeling work done by other researchers.

Suppose both the measurements and the simulations were reliable, the error between the measured data and the theoretical expectation could possibly mean that the fabrication quality of the sample chip needed improvements. The thickness of waveguides located on different regions of the wafer did not seem to be consistent -- the gold layer tended to be thicker in the center of the wafer while thinner on the edge. There were defects on the end-facet which would affected the optical power output but could not be detected during inspection. Irregular deformation prevailed on the wafer making waveguides even in the nearby region or right on the same chip deform differently in type and extent, and therefore become less comparable with each other.

Though the quality of the chips prevented us from obtaining a consistent set of butt-coupling loss, attenuation, radiation loss, and transition loss for them, conclusions could still be drawn that most of the tested waveguides were thinner than they were designed to be. The contrasts of relatively lower attenuation of the straight waveguide of various widths, S-bends (5dB/mm for DIE39_1, 6dB/mm for DIE39_2), and Y-junctions (4.8dB/mm) to the value of the designed thickness 35nm (7.1776dB/mm) all support such a conclusion.

Thermo-optic modulation experiments were also carried out on these chips. The optical measurement method remained the same, meanwhile electric currents were injected into them through metal pads, heating the waveguides, increasing their temperature, and making the refractive indices change correspondingly.

In the first step, a threshold current density for electromigration was found by measuring the resistance of the waveguide versus time and voltage. 70GA/m^2 was chosen as the threshold current density allowing the waveguides to work for a total lifetime of at least 1 hour under this current density.

In the next step, straight waveguide were thermo-optically tested and improvements were made by adding a TEC into the setup system. As the injected current went higher the optical power output firstly remained stable, then fluctuated a little and rose to a first peak, and then dropped to a first valley, passed a second bump and eventually got cut off. As experiments were run on the same waveguide time and time again the obtained optical-power-versus-current curves gradually and consistently drifted leftward, due to the accumulation of heat brought about by the low thermal conductivity of CYTOP, as well as possible changes to the waveguide due to operation through the glass transition temperature of CYTOP. Although the mode cut-off limit would decrease with the whole curve drifting leftward, a threshold current of about 2.5mA could be safe for waveguides on DIE2 to run the first 12 experiments.

During the experiments some improvements could be made in order to enhance the stability of the setup, making the measurements easier and the acquired data more precise. The improvements include: cleaving the fibers shorter, building a plastic tent, removing instruments that have fans away from the working table, and adding refractive index matching oil.

5.2 Contributions

The contributions of this thesis to the advancement of integrated LRSPP technology were as follows. To begin with, gold LRSPP waveguides and passive elements (S-bends, Y-junctions, MZIs, and couplers) with CYTOP claddings were characterized for the first time, as well as the thermo-optic performance of a straight waveguide section. Moreover, improvements were made to the experimental setup and operation. Last but not least, the difficulty of getting well enough fabricated CYTOP cladded chips and the problem the low heat conductivity of CYTOP brought to thermo-optic modulation experiments were noticed.

5.3 Future work

One suggestion for the future work is to use refractive index matching oil in passive measurements. The oil may be inconvenient for operating, but it can make the data more precise since the experimenter no longer need to pick out the maximum power value from the fast-jumping readings of the power meter.

Another suggestion is that we should redesign the wafer so that each kind of chip has several ones in the center region where the quality of the chip is usually better than that on the edge, so that passive measurements, thermo-optic modulations, fluidic sensing experiments and other varieties of experiments can all have some good-quality chips to use.

Thirdly, MZIs can be thermo-optically tested with one arm under thermo-optic modulation and it is expected that below the mode extinction threshold the output power goes up and down periodically as the current increases. MZIs of dual and triple outputs can also be tested. The two or three outputs are predicted to alternately rise and drop, in a complementary manner in the case of the dual output MZIs whereas with a 120-degree phase difference with respect to each other in the triple output case.

Appendix A: Mean time to failure

There is a term for the lifetime of a waveguide called mean time to failure (MTTF), describing the relation between the lifetime the waveguide can work, the injected current density, and the temperature of the waveguide given as follows [25~28].

$$MTTF = \frac{A}{j^n} exp\left(\frac{E}{kT}\right) \tag{A.1}$$

j is the current density, *T* is the waveguide temperature, *k* is the Boltzmann constant, *A* is a cross-section-area-dependent factor, *n* is a scaling factor, and *E* is the effective activation energy of the electromigration failure process. The *A*, *n* and *E* parameters for a waveguide cannot be foreseen. For a certain waveguide type, they can be obtained by measuring three groups of data of *MTTF*, *j* and *T*, and fill them into a transformation of (A.1) as follows.

$$ln(MTTF) = lnA - nlnj + \frac{E}{kT} \tag{A.2}$$

Solving the three linear equations we can get the solution for the three unknown values *lnA*, *n* and *E*. Thus the *A*, *n* and *E* parameters for this kind of waveguide will be known.

Appendix B: Preliminary thermo-optic modulation of MZIs

In this experiment one arm of the MZI was attached by the metal probes though which a voltage was applied. Figure B.1 shows the mode output for different voltages. The applied voltage and notes for each mode is marked below the output.

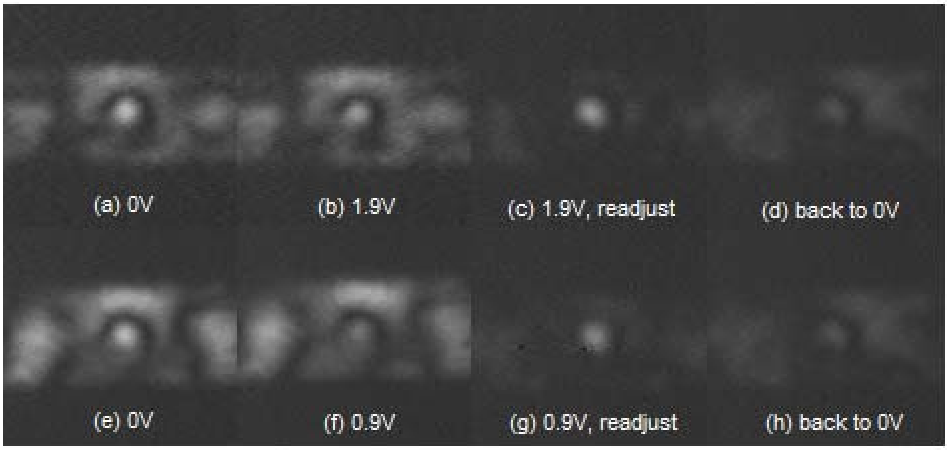

Figure B.1: Preliminary thermo-optic modulation of MZIs

Figure B.1(a) is the mode without voltages applied to the waveguide. It is a typical mode pattern for MZIs -- a mode output added to strong background light -- as was described in Section 3.5. Next step the voltage was increased to 1.9V and the mode output is given in Figure B.1(b), which looks the same pattern as (a). But after the alignment of fiber and waveguide was readjusted, as shown in Figure B.1(c), a clear mode output with obviously less background light appeared which seems to have the same pattern of a straight waveguide. After that the voltage returned to 0V and the mode output shown in Figure B.1(d) looked different from the original output in referring to (a). I readjusted the alignment to restore the typical MZI mode pattern, and started another turn of experiment with the voltage increased to 0.9V. Similar results were generated and are given in Figure B.1(e)~(h).

It is strange that the background light was heavy at 0V compared to that at certain voltages such as 0.9V and 1.9V, when the background light was removed. One reasonable explanation was that the two arms of the MZI have different optical path lengths, which is probably caused by chip fabrication problems. When there was no voltage applied, mode travelling through the two arms interfered, leaking more power into the background. As the voltage increased to 0.9V or 1.9V the optical path length along one arm of the MZI changed, so the two arms fulfilled the condition of constructive interference and the background light was diminished.

Bibliography

[1] A. D. Boardman, Ed., Electromagnetic Surface Modes, Wiley, 1982.

[2] V. M. Agranovich, D. L. Miles, Surface Polaritons: Electromagnetic Waves at Surfaces and Interfaces, Eds., North Holland, 1982.

[3] H. Raether, Surface Plasmons on Smooth and Rough Surfaces and on Gratings, Springer, 1988.

[4] Goodfood: tutorial on biosensors, http://www.goodfood-project.org/.

[5] P. Berini, "Long-range surface plasmon polaritons," Advances in Optics and Photonics 1, 484-588 (2009) doi: 10.1364/AOP.1.000484.

[6] P. Berini, "Figures of merit for surface plasmon waveguides," Opt. Express (2006) 14: 13030-13042.

[7] Guy Gagnon, "Thermo-optic variable optical attenuators using plasmon-polariton waveguides," M.Sc. dissertation, Department of Electrical Engineering, University of Ottawa, Ottawa, NO, Canada, 2003.

[8] P. Berini, "Plasmon-polariton waves guided by thin lossy metal films of finite width: Bound modes of asymmetric structures," Phys. Rev. B (2000) 63: 125417.

[9] P. Berini, "Plasmon-polariton waves guided by thin lossy metal films of finite width: Bound modes of symmetric structures," Phys. Rev. B (2000) 61: 10484-10503.

[10] R. Charbonneau, P. Berini, E. Berolo, E. Lisicka-Shrzek, "Experimental observation of plasmon polariton waves supported by a thin metal film of finite width," Opt. Lett., Vol. 25, pp. 844-846, 2000.

[11] G. Gagnon, N. Lahoud, G. A. Mattiussi, P. Berini, "Thermally activated variable attenuation of long-range surface plasmon-polariton waves," Journal of Lightwave Technology, Vol. 24, No. 11, November 2006.

[12] E. D. Palik, G. Ghosh, Electronic Handbook of Optical Constants of Solids, Academic Press, 1999.

[13] T. Nikolajsen, K. Leosson, S. I. Bozhevolnyi, "In-line Extinction modulator based on long-range surface plasmon-polaritons," Opt. Comm., Vol. 244, pp. 455-459, 2005.

[14] I. Breukelaar, R. Charbonneau, P. Berini, "Long-range surface plasmon-polariton mode cutoff and radiation," Appl. Phys. Lett., Vol. 88, 501119, 2006.

[15] Sang-Shin Lee et al. "Variable optical attenuator based on a cutoff modulator with tapered waveguides in polymers," Journal of Lightwave Technology, Vol. 17, No. 12, December 1999.

[16] P. Berini, G. Gagnon, S. Jetté-Charbonneau, "Thermo-optic plasmon-polariton devices," US Patent 7,043,134 (issued 2006), filed 2004.

[17] A. S. Oates, "Electromigration transport mechanisms in Al thin-film conductors," Journal of Applied Physics, Vol. 79, No. 1, January 1, 1996.

[18] C. Chiu, "Fabrication of surface plasmon waveguides and devices in CYTOP with integrated microfluidic channels," M.Sc. dissertation, School of Information Technology and Engineering, University of Ottawa, Ottawa, NO, Canada, 2009.

[19] C. Chiu, E. Lisicka-Shrzek, "Fabrication of surface plasmon waveguides and devices in CYTOP with integrated microfluidic channels," J. Vac. Sci. Technol. B 28(4), Jul/Aug. 2010.

[20] Ewa Lisicka-Shrzek, "Biosensor mask DIE description," private communication, June 2009.

[21] T. Nikolajsen, K. Leosson, S. I. Bozhevolnyi, "Surface plasmon-polariton based modulators and switches operating at telecom wavelengths," Appl. Phys. Lett., Vol. 85, No.24, December 13, 2004.

[22] Robin Buckley, "Biosensor designs on CYTOP," private communication, May 2009.

[23] R. Charbonneau, E. Lisicka-Shrzek, P. Berini, "Broadside coupling to long-range surface plasmons using an angle-cleaved optical fiber," Appl. Phys. Lett. 92, 101102 (2008).

[24] Amorphous Fluoropolymer CYTOP, Asahi Glass Co., Ltd, http://www.agc-cytop.com/, January 2009.

[25] Daniel Young, Aristos Christou, “Failure mechanism models for electromigration,” IEEE Transactions on Reliability, Vol. 43, No.2, June 1996.

[26] Jens Lienig, Göran Jerke, “Embedded tutorial: Electromigration-aware physical design of integrated circuits,” Proceedings of the 18th International Conference on VLSI Design held jointly with 4th International Conference on Embedded System Design (VLSID’05) 1063-9667/05.

[27] R. L. de Orio, H. Ceric, S. Selberherr, “Physically based models for electromigration: From Black’s equation to modern TCAD models. Microelectronics Reliability (2010),” doi: 10.1016/j.microrel.2010.01.007.

[28] K. N. Tu, “Recent advances on electromigration in VLSI of interconnects,” Journal of Applied Physics, Vol.94, No.9, November 1, 2003.